UNIVERSITY OF CALIFORNIA
SANTA CRUZ

LOCAL STRUCTURE ANALYSIS OF MATERIALS FOR INCREASED ENERGY EFFICIENCY

A dissertation submitted in partial satisfaction of the
requirements for the degree of

DOCTOR OF PHILOSOPHY

in

PHYSICS

by

Scott Medling

June 2012

The Dissertation of Scott Medling
is approved:

Professor Frank Bridges, Chair

Professor Sue A. Carter

Professor David P. Belanger

Dean Tyrus Miller
Vice Provost and Dean of Graduate Studies

Table of Contents

List of Figures

List of Tables

Abstract

Local Structure Analysis of Materials for Increased Energy Efficiency

by

Scott Medling

In this dissertation, a wide range of materials which exhibit interesting properties with potential for energy efficiency applications are investigated. The bulk of the research was conducted using the Extended X-ray Absorption Fine Structure (EXAFS) technique. EXAFS is a powerful tool for elucidating the local structure of novel materials, and its advantages are presented in Chapter 2.

In Chapter 3, I present details on two new techniques which are used in studies later in this dissertation, but are also promising for other, unrelated studies and, therefore, warrant being discussed generally. I explain the presence of and present a method for subtracting the X-ray Raman background in the fluorescence window when collecting fluorescence EXAFS data of a dilute dopant Z in a Z+1 host. I introduce X-ray magnetic circular dichroism (XMCD) and discuss the process to reduce XMCD data, including the self-absorption corrections, for low energy K-edges.

In Chapter 4, I present a series of investigations on ZnS:Cu electroluminescent phosphors. Optical microscopy indicates that the emission centers do not degrade uniformly or monotonically, but rather, most of the emission centers blink on and off during degradation. The effect of this on various proposed degradation mechanisms is discussed. EXAFS data of ZnS:Cu phosphors ground to enable thinner, lower-voltage

devices indicate that grinding preferentially causes damage to the CuS nanoprecipitates, quenching electroluminescence (EL) and concluding that smaller particles must be built up from nanoparticles instead. EXAFS data of nanoparticles show that adding a ZnS shell outside a ZnS:Cu core provides significant additional encapsulation of the Cu, increasing photoluminescence and indicating that this may increase EL if devices can be fabricated. Data from extremely dilute (0.02% Cu) ZnS:Cu nanoparticles is presented in order to specifically study the non-precipitate and suggests that the Cu dopant substitutes for Zn and is adjacent to a S vacancy.

In Chapter 5, I present a study into thermoelectric clathrates to determine how differences in size of one of the cage atoms affects the local structure and, therefore, the thermoelectric properties. I then discuss the effect of additional cage disorder on the scattering of phonons and the scattering of electrons, and thus the thermoelectric figure of merit.

In Chapter 6, I present an XMCD study of $La_{1-x}Sr_xCoO_3$, finding results that are consistent with Sr-induced formation of ferromagnetic clusters within the non-magnetic, insulating matrix. We also show that not only are the O states spin-polarized, but a significant fraction of holes from Sr-doping go onto the O sites. Further, experimental results are compared to density functional calculations and discussed.

To my wife and parents,

for their love, encouragement, and support.

Acknowledgments

I owe many thanks to my advisor, Bud Bridges; this research would not have been possible without his patient teaching, guidance, and support. I also want to thank the rest of my committee, Sue Carter and Dave Belanger, for their time and guidance.

I would like to express my sincere gratitude to Justin Jiang and Chris France for the time they took away from their research to teach me. I want to thank Mike Kozina, Brad Car, Brian Vollbrecht, Trevor Keiber for time and effort spent helping with data collection and reduction. I would also like to specifically thank Corwin Booth for maintaining RSXAP and making adjustments to solve unique problems I encountered.

I want express my appreciation to all of those who synthesized samples for my research: Carley Corrado and the other students in Jin Zhang's lab, Ben Balaban and Chris France in Sue Carter's lab, Andrew Short and Ian Carbone in Glenn Alers' lab, and Toshiro Takabatake's group.

The text of this dissertation includes reprints of or substantial excerpts from the following previously published material:

[Medling *et al.*, 2011] – I performed the optical microscopy and collected & analyzed substantial portions of the local structure (XANES and EXAFS) data.

[Medling and Bridges, 2011] – I conducted the research under the supervision of F. Bridges.

[Car *et al.*, 2011] – I performed the background subtraction, collected & analyzed a substantial amount of the data and authored much of the paper.

[Corrado *et al.*, 2010] – I performed the local structure (EXAFS) portions of the research.

ZnS:Cu phosphor work was supported by the US Department of Energy Basic Energy Sciences grant DE-FG02-07ER46388-A002. Thermoelectric clathrate work was supported by the US National Science Foundation grant DMR-1005568 XMCD and cobaltate work was supported by the US Department of Energy Basic Energy Sciences grant DE-AC02-07CH11358.

Chapter 1

Introduction

In order to understand the fundamental physics of complex phenomena, it is first necessary to understand the local structure (or the structure of materials at the atomic scale). Only once the physical basis for phenomena are better understood is it possible to come up with new ideas or models and for industry to develop the applications of the future.

Primarily, I use the extended X-ray absorption fine structure (EXAFS) technique due to several of the unique advantages over other techniques. EXAFS is fast; probing the local structure in $< 10^{-15}$ seconds. EXAFS is tuned to individual elements within the material, allowing the separate analysis of the neighborhood around dilute dopants from the rest of the host material and making it possible to isolate individual elemental bond-lengths between elements mixed on a variety of lattice sites. X-ray data collected at synchrotron light sources produces polarized light, which can be used to probe the spin and orbital magnetic moments of individual elements in magnetic mate-

rials. The reason for and origin of these advantages are presented in Chapter 2, along with the details on how we collect and analyze data.

In the process of studying the properties of novel materials, new problems are stumbled upon which often require creative solutions. In Chapter 3, I describe the methods I devised and implemented for new techniques to better understand certain classes of materials.

The specific materials investigated here are all related to sustainable energy. The electroluminescent phosphors discussed in Chapter 4 are a cheap, abundant, non-toxic method of creating solid-state lighting, and have the potential to do so very efficiently. The thermoelectrics presented in Chapter 5 are used in easily scalable heat engines or solid state coolers, and can be used for waste heat recovery or targeted cooling (respectively). The research presented in Chapter 6 will expand mankind's understanding of magnetism in general, important for precisely controlling a variety of magnetic systems.

More specific motivation is provided at the beginning of each chapter for each of those materials and due to the fact the results from each section are not applicable to the other materials, conclusions are listed within each section.

Chapter 2

EXAFS Background

2.1 Synchrotron Radiation

2.1.1 Radiation Emission

The basic principal behind most methods of generating X-rays is that whenever charged particles (*i.e.* electrons) are accelerated, radiation is emitted. In the case of small X-ray units, electrons are gradually accelerated and then suddenly brought to a halt when colliding with a target, resulting in the emission of X-rays. In a synchrotron, relativistic electrons travel in a closed loop, and the bending magnets which keep the beam in a circle do so by accelerating the electrons inward, producing a stream of X-rays, as seen in Figure 2.1.

In order to increase intensity, most beamlines now utilize a related method called a wiggler, which involves a series of oppositely aligned magnets to rapidly deflect the electron path back and forth, forcing the electron bunches to travel in waves

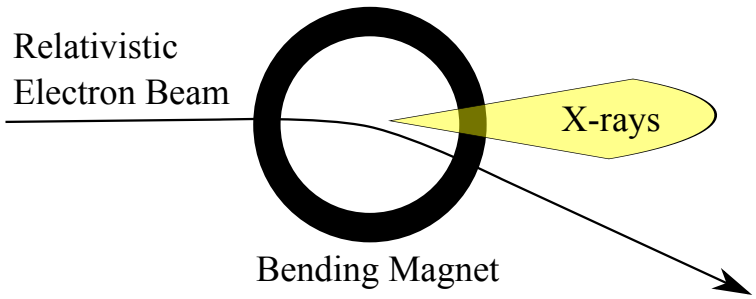

Figure 2.1: Diagram of electrons emitting synchrotron radiation while proceeding through a bending magnet.

(spatially), emitting X-rays with an increase in intensity depending on the number of pairs of magnets (typically 10-20). It is also possible to construct a wiggler such that the X-ray output is circularly polarized rather than linearly polarized.

In either case, the radiation produced by a synchrotron is a broad spectrum with high flux, brilliance (collimation), and stability. Further, the radiation is inherently (horizontally) polarized and it is possible to produce individual, timed packets of X-rays for pump-probe measurements. For these reasons, synchrotrons have become the lightsource of choice for researchers using X-rays.

2.1.2 Energy Resolution

While the X-rays from the synchrotron are a broad spectrum, in order to perform spectroscopy, it is necessary to isolate a single X-ray energy at a time. Thus, a double monochromator is used to select a given photon energy.

Uncertainty in the actual X-ray energy incident on the sample is caused by two major factors: the intrinsic uncertainty of the monochromator (dE_i/E) and the

uncertainty due to spread of the beam (dE_s/E), which depends on a number of physical parameters including the slit height (h), the distance to from the bending magnet or (L), and the lattice parameter of the monochromator (d). The monochromator parameters for various monochromators we have used are listed in Table 2.1.

Monochromator	dE_i/E ($\times 10^{-5}$)	$2d$ (Å)
Si(111)	14.1	6.271
Si(220)	6.04	3.840
Si(400)	2.53	2.715

Table 2.1: Energy resolution parameters for the monochromators used at SSRL.

To calculate the uncertainty in the energy resolution due to the spread of the beam, one uses the following formula:

$$dE_s/E = \tan(h/L)\cot\left(\sin^{-1}\left(\frac{12.4 \text{ Å keV}}{(2d)E}\right)\right) \tag{2.1}$$

This is then added, in quadrature, to the intrinsic uncertainty for the monochromator to determine the overall uncertainty in the incident X-ray energy. When selecting a monochromator it is also important to consider the total flux, minimum and maximum energy, and the location of any glitches within the scan region.

2.2 X-ray Absorption Spectroscopy

2.2.1 X-ray Absorption and Fluorescence

Generally, X-ray absorption decreases with increasing energy, until the X-ray energy of the incident photon is large enough to eject a lower energy electron from the atom into an unoccupied energy level (typically the conduction band). At that point, the absorption cross-section jumps, as shown in Figure 2.2. Quantum mechanically, this is due to the fact that the probability of the photon being absorbed by the electron depends on the initial and the final state of the electron, which includes the superposition of the outgoing and all incoming, backscattered waves and the potential energy difference between the atomic state and the Fermi energy.

After the X-ray has been absorbed and the photoelectron has been ejected, its original atom is left lacking an inner electron, and is said to have a core hole. At this point, one of the other electrons in the atom will quickly fall down into the hole, emitting a fluorescence X-ray.

The location of these edges (and fluorescence energies) are element-specific and exist for each of the electron energy levels within each element (K = 1s, L1 = 2s, etc. as shown in Figure 2.2). For this reason, for X-ray spectroscopy performed over a relatively narrow range at a given edge allows the probing of the local structure around individual elements, a feature which sets XAS, and techniques derived from it, apart from most other techniques.

It is important to mention that the lifetime of the core hole, left behind by

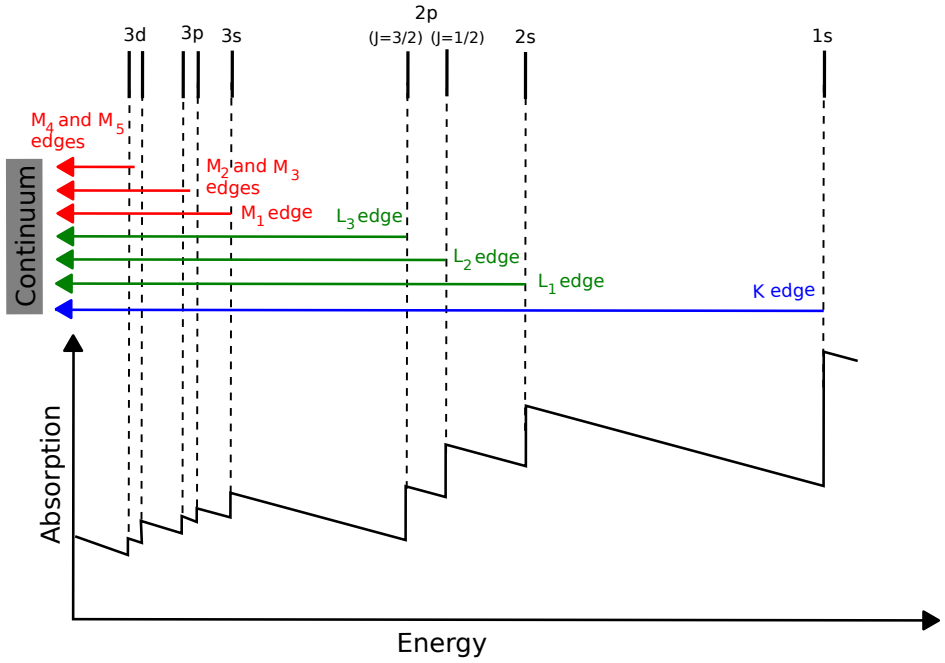

Figure 2.2: Absorption as a function of energy for K, L, and M edges, as well as how edges are related to individual electron orbitals. (Diagram is for a general element ^{30}Zn $\leq$ Z $\leq$ ^{36}Br. Lighter elements lack edges starting at the left; heavier elements add edges to the left.)

the ejected photoelectron, is on the order of 10^{-15} seconds. This a very short time compared to most atomic phenomena, but is long enough that the photoelectron has time to backscatter off of nearby atoms and return to produce an interference pattern at the absorbing atom.

Simple X-ray absorption spectroscopy (XAS) is a useful technique. It is possible to determine the relative concentrations of a sample by comparing the ratio of the absorption edge heights at the same location on a sample to those published in the McMaster Tables.

2.2.2 XANES and EXAFS

In reality, the absorption edges are not as sharp and straight as indicated in Figure 2.2, but instead possess variations in a short region both just below the edge energy (in what is called the pre-edge region—and is due to excitations of core electrons into higher energy bound states instead of the continuum) and in a longer region extending several hundred eV above the edge energy. X-ray absorption near-edge spectroscopy (XANES) is the study of the immediate post-edge region (up to $\sim$ 30 eV above the edge) and extended X-ray absorption fine structure (EXAFS) is the study of the post-edge region starting $\sim$ 30-50 eV above the edge through the end of the visible oscillations, as can be seen in Figure 2.3.

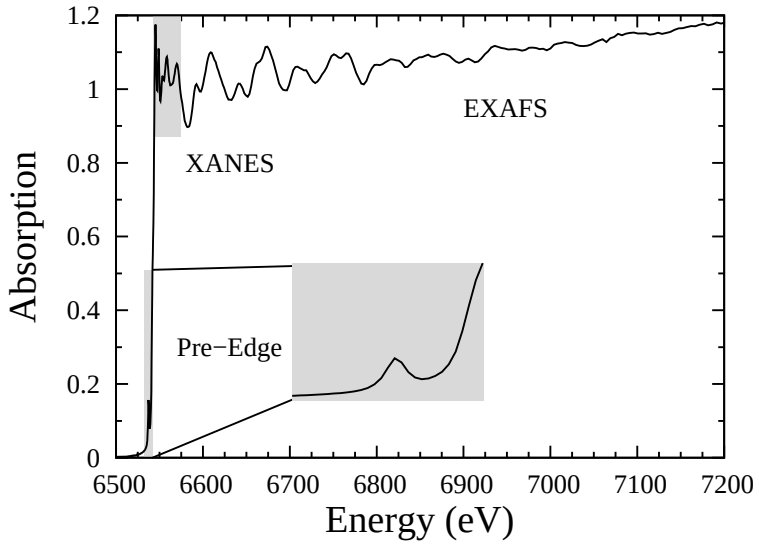

Figure 2.3: A sample spectrum (ZnS:Cu,Mn, Mn K-edge). Pre-edge is shown shaded and enlarged in inset; XANES is showed shaded; EXAFS region extends from approximately the high end of the XANES region to the end of the scan.

After the incident X-ray ejects an electron from the host atom, it becomes a

photoelectron and must travel somewhere. Due to the wave-particle duality, this photoelectron will have a wavelength $\lambda = h/p$, where the momentum (p) of the photoelectron is determined by the energy of the incident X-ray (E) in excess of the binding energy of the electron (E_0), so that:

$$p = \sqrt{2m(E - E_0)} \tag{2.2}$$

Thus, the wavelength of the outgoing photoelectron is directly determined by the incident X-ray energy. This wavelength is important because the photoelectron can backscatter off of nearby atoms in the sample back to the original absorbing atom, creating an interference pattern, and modulating the absorption coefficient (depending on the incident X-ray energy), to produce the oscillations that are observed above the absorption edge. When, these oscillations are viewed in momentum-space instead of in energy space, they become less distorted, and can be Fourier Transformed into position space to find the actual bond lengths. Therefore, the energy of the incident photon, via the momentum of the photoelectron, enables a measurement of the interatomic distances between individual elements.

The oscillations in the long EXAFS region are associated with photoelectrons creating an interference pattern after backscattering off of individual atoms several wavelengths away from the absorbing atom. The EXAFS results can also be calculated from theoretical standards, allowing the comparison with various proposed local structures. This enables EXAFS to determine the types and number of neighbors and bond lengths to 0.01 Å (and, therefore, distortion or disorder in the system, including the Debye-

Waller factor, σ). Despite this, it is important to keep in mind that EXAFS cannot resolve peaks less than 0.1 Å apart.

The XANES region close to the edge is associated with several interactions. Here, the outgoing photoelectron can interact with another electron bound to the atom and cause it to jump into another energy state (*i.e.* "shake-up" or "shape-down"); this requires that the additional energy of the photon just exceeds the energy difference of the initial and final state of the other electron. XANES is also sensitive to scattering off of several successive neighbors (out to 7-9 Å). However, XANES modeling and accurate theoretical calculations are computationally difficult. Nonetheless, XANES is particularly sensitive to bond lengths and, therefore, the valences of atoms, and is still quite useful for comparing experimental data to experimental standards, and may be useful for comparing to theoretical standards for certain materials.

2.2.3 EXAFS Analysis

The absorption of a sample of thickness t is expressed as μ in the equation:

$$\mu t = log(I_0/I_1) \tag{2.3}$$

where I_0 is the intensity of the X-ray beam incident on the sample and I_1 is the intensity of the X-ray beam after having passed through the sample.

The background from other elements and absorption of other electrons is extrapolated from the pre-edge region and subtracted from the data, as shown in Figure 2.4(a). We then normalize the step height to 1, to obtain the interference function:

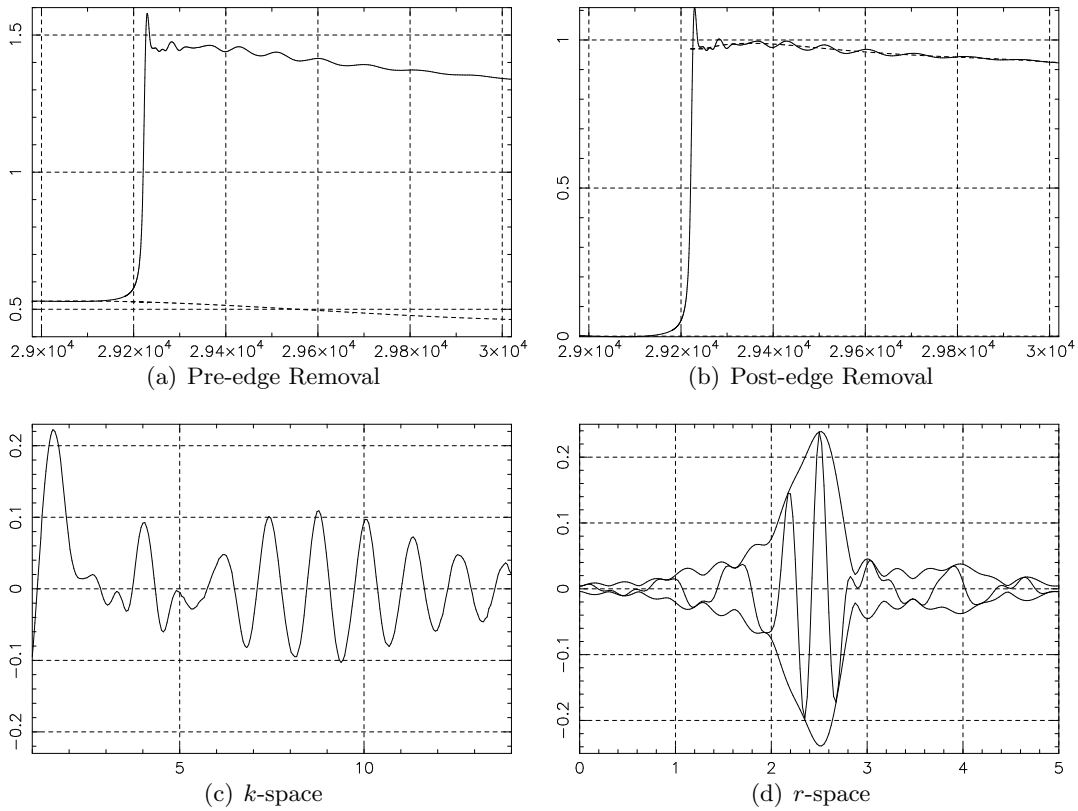

(a) Pre-edge Removal (b) Post-edge Removal

(c) k-space (d) r-space

Figure 2.4: (a) Pre-edge Removal shows the raw data (solid line) and the background fit (dashed line). (b) Post-edge Removal showing the resulting data after the pre-edge background subtraction (solid line) and the spline through the post-edge region (dashed line). (c) k-space shows oscillations spaced regularly in k-space, with attenuation visible above 9 $\mathring{A}^{-1}$. (d) r-space showing the the real part of the Fourier Transform rapidly oscillating inside the amplitude envelope.

$$\chi(E) = \frac{\mu(E) - \mu_0(E)}{\mu_0(E)} \tag{2.4}$$

To truly isolate the oscillations, a spline is fitted through the data above the edge, as shown in Figures 2.4(b), resulting in oscillations about zero. The number of knots (generally, spaced evenly in k-space rather than energy-space) can be controlled in order to balance the degree to which the spline will eliminate the lower frequency background components, but not affect the higher frequency EXAFS oscillations. (Note, it is also possible to use a theoretical $\mu_0(E)$ curve, which then does not require two separate background subtractions.)

The next step in the process is to convert from energy space into k-space:

$$k = \frac{\sqrt{2m(E - E_0)}}{\hbar} \tag{2.5}$$

For electrons, this results in a fairly easy-to-remember formula with k in Å and E in eV:

$$k \approx 0.512\sqrt{E - E_0} \tag{2.6}$$

To compensate for the attenuation of the EXAFS signal at large k (as seen in Figure 2.4(c)), the EXAFS amplitude ($\chi(k)$) at large k it is often multiplied by some power of k, resulting in $k^n\chi(k)$, before proceeding with the reduction.

The last step, is to Fourier Transform the k-space data into real space, resulting in the data shown in Figure 2.4(d). Typically, the window is rounded using a Gaussian in order to decrease ringing artifacts. It is important to note that this step gives peaks

that are shifted from the known values by 0.2-0.5 Å. This is due to a well-known effect of the phase shift, and can be accounted for in calculations.

2.2.4 EXAFS Equation

EXAFS began to be understood in the mid-1970s,[Stern, 1974; Lee and Pendry, 1975] and by this time the theory has been well established. Only a summary explanation is reproduced here.

The starting point for modulation of the final state wavefunction is given by Fermi's Golden Rule:

$$\mu \sim < f|H'|i > \tag{2.7}$$

where the relevant Hamiltonian, H', takes into account a number of factors, which are laid out in Table 2.2.

For polycrystalline samples, every angle is averaged over, so the dipole approximation goes to a constant. The Gaussian harmonic approximation, which approximates the disorder in the system, simplifies to $\approx e^{-2\sigma^2/k^2}$ for $k\sigma \ll 1$. These, and simple algebraic combination of terms, gives the following result for the amplitude modulation of the absorption in the EXAFS region:

$$\chi(k) = \sum_i \frac{N_i S_0^2}{kr_i^2} F_B(k, r_i) e^{-2r_i/\lambda(k)} e^{-2\sigma^2 k^2} \sin\left(2kr_i + 2\phi_c + \phi_i\right) \tag{2.8}$$

It is important to note that the EXAFS signal is naturally attenuated by the $1/k$ factor present in the EXAFS Equation (Equation 2.8). It is also interesting

Term	Reason
$\sum_i N_i$	Sum Over Each Neighbor
S_0^2	Inelastic Loss Factor
$\int \frac{1}{\sqrt{2\pi}\sigma} e^{-(R-r_i)^2/2\sigma^2} dR$	Gaussian Harmonic Approximation
$(\hat{\epsilon} \cdot \hat{r})^2$	Dipole Approximation
$\frac{e^{-ikr_i}}{kr_i}$	Outgoing Spherical Wave
$e^{i\phi_c(k)}$	Central Atom Phase Shift (going out)
$e^{-r_i/\lambda(k)}$	Electron Mean Free Path (going out)
$k\lvert f(\pi,k)\rvert \frac{e^{-ikr_i+i\phi_i(k)}}{kr_i}$	Complex Backscatter Probability (amplitude & phase)
$e^{-r_i/\lambda(k)}$	Electron Mean Free Path (coming back)
$e^{i\phi_c(k)}$	Central Atom Phase Shift (coming back)

Table 2.2: Derivation of the EXAFS Equation. The inelastic loss factor, S_0^2, is generally 0.9-1.0.

that the backscattering amplitude F_B which determines the amplitude depends only on the backscattering atoms, whereas the phase factor is actually twice as sensitive to the absorbing atom as backscattering atoms due to the fact that the photoelectron wavefunction experiences the phase shift from the absorbing atom both going out and coming back, compared to only once from backscattered atoms.

That EXAFS can be used to determine the Debye-Waller factor (from the Gaussian harmonic approximation) is another benefit to using the technique, as otherwise it is usually difficult to obtain. To do so, it is necessary to collect data at several temperatures 4–320 K, at which point it is possible to determine the values of the thermal and static portion of σ^2. For a system without additional disorder (such as

Jahn-Teller splitting):

$$\sigma^2 = \sigma^2_{\text{static}} + \sigma^2_{\text{thermal}} \tag{2.9}$$

2.3 Experimental Setup

There are two basic methods to conduct X-ray spectroscopy: transmission and fluorescence. The setup is shown in Figure 2.5. In transmission, the absorption of the entire sample is directly calculated from the intensity of the beam before and after passing through the sample. In fluorescence, the absorption of the specific element is calculated by looking at the emission of X-rays at the characteristic fluorescence energy for the desired element. This fluorescence signal is proportional to transmission (from ∼5% for oxygen K to ∼90% for barium K), and enables the collection of data in cases where it is not possible to obtain a high-quality transmission data, whether because the sample is too thick to allow sufficient X-rays to pass through or if the element of interest is too dilute in the sample. It is also important to note that fluorescence data tends to have a much lower signal-to-noise (S/N) ratio than data collected in transmission.

Reduction of fluorescence data is much the same as transmission data with a few exceptions. When the data is initially collected, it is important to take a separate deadtime scan, in order to measure the response of the fluorescence detector. When reducing the fluorescence data, it is necessary to apply a self-absorption correction, in order to account for the fact that some of the fluorescence X-rays are reabsorbed by

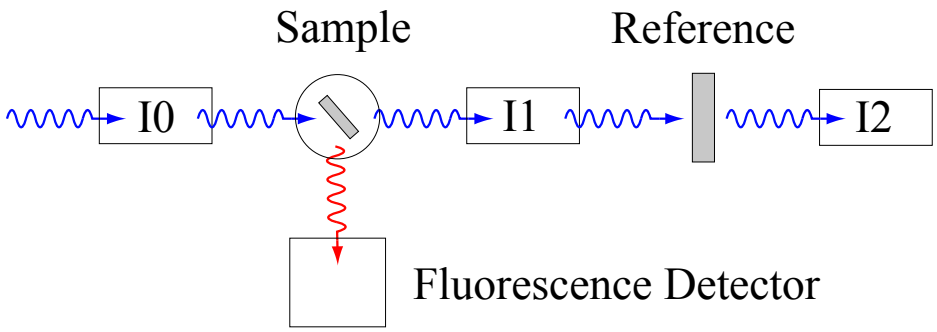

Figure 2.5: Diagram of experimental setup for collecting data in transmission and/or fluorescence. For taking data in only transmission, sample would be normal to the X-ray beam instead of at 45°. The reference sample is used to measure any monochromator drift, which can then be corrected during data reduction.

the sample, with the ratio depending on the thickness of the sample and fluorescence energy.[Booth and Bridges, 2005] This correction is described in more detail in Section 3.2. Another, though relatively minor difference, is that the fluorescence background also does not follow the same formula as the transmission background, resulting in a slightly different subtraction process.[Booth, 2012]

Because the monochromators work by utilizing Bragg scattering, they not only reflect the photons of the desired energy, but also, to a lesser extent, the photons with an energy of some integer multiple of the fundamental energy. Due to the fact that these harmonics are less absorbed by the sample, the background they create cannot be properly subtracted. They also result in additional monochromator glitches being present in the data as well as possibly running into absorption edges of any of the other materials present in the sample, if any edges are present in multiples of the scan energies. In addition, since all that is required to produce fluorescence is a source of X-rays with

higher energy than the absorption edge, it is possible for harmonics to excite a small signal at a large number of fluorescence energies, resulting in further difficulties when collecting data in fluorescence mode.

Fortunately, an easy way to decrease the intensity of the harmonics is to detune the monochromator. Since the width of the Bragg peak for the harmonics is typically narrower than for the desired energy, detuning so that the fundamental is decreased to about half intensity generally results in the harmonics being nearly eliminated.

The X-ray data presented here came primarily from the Stanford Synchrotron Radiation Lightsource (SSRL) at SLAC National Accelerator Laboratory, but a small portion came from the Advanced Photon Source (APS) at Argonne National Lab. The transmission detectors are high voltage ion chambers filled with either N_2 or Ar gas, depending on the X-ray energy; Ar absorbs too many of the X-rays to be used at low energy while N_2 doesn't absorb enough X-rays at high energy to provide a good signal-to-noise ratio (S/N). Fluorescence data was typically collected using a 13-element Ge detector. Our samples are mounted in a liquid helium flow cryostat, with a temperature sensor and resistive heaters connected to a power supply to maintain any desired temperature 4–320 K.

Chapter 3

New X-ray Techniques

3.1 Raman Background Subtraction

3.1.1 Motivation

A common technique for investigating the local structure about dilute atomic species, is to use fluorescence Extended X-ray Absorption Fine Structure (EXAFS). Typically, the fluorescence mode becomes better than transmission for concentrations below a few percent (depending on the host material) and in some cases, data for concentrations below 0.01% are possible. However, when studying impurity atoms with atomic number Z in a host of atoms with atomic number Z+1, a large background in the fluorescence signal may be observed if the impurity concentration is very low.

For such systems, the normally weak X-ray Raman emission line from the Z+1 host atoms, which occurs at a fixed energy below the incident X-ray energy, can add a significant background signal near the fluorescence energy of the Z dopant. The Raman

emission peak shifts to higher energy and becomes larger in intensity as the X-ray energy is scanned. Consequently, for solid state fluorescent detectors with a resolution of 200–400 eV, the Z+1 Raman peak will partially overlap the window set up for collecting the fluorescence for the dilute Z atom; the resulting background in the fluorescence signal is not oscillatory, but produces a large upward slope of the data as the energy is scanned.

As an example, we consider a recent study of 0.02% Cu (Z = 29) in a ZnS host (Z = 30 for Zn). For this very low Cu concentration, the fluorescence detector system as set up for Cu K-edge EXAFS produces a large background that increases rapidly with energy as the scanned energy approaches the Zn K-edge, as can be seen in Figure 3.1 (dashed line). This background is not obvious in the EXAFS data for samples of higher concentration Cu in ZnS (0.5%), for which the average amplitude above the edge is roughly constant (solid line in Figure 3.1). In looking at the output of the fluorescence detector at various energies using a multi-channel analyzer, it became apparent that there were two factors contributing to this steep background: a small peak passing through the Cu K-edge fluorescence window as the incident X-ray energy increased (identified as the Zn Raman line[Sánchez *et al.*, 2006]) and a small part of the tail from the Zn fluorescence peak, just below the Zn K-edge, that is within the Cu K-edge fluorescence window. A similar background would be present in fluorescence EXAFS spectra for any system with a dilute atomic number Z in a host with Z+1.

This background produces difficulties for EXAFS analysis since the EXAFS oscillations, χ, are most rigorously extracted using $\chi(E) = \mu(E)/\mu_o(E) - 1$, where $\mu(E)$ is the total absorption at energy E and $\mu_o(E)$ is the average function through

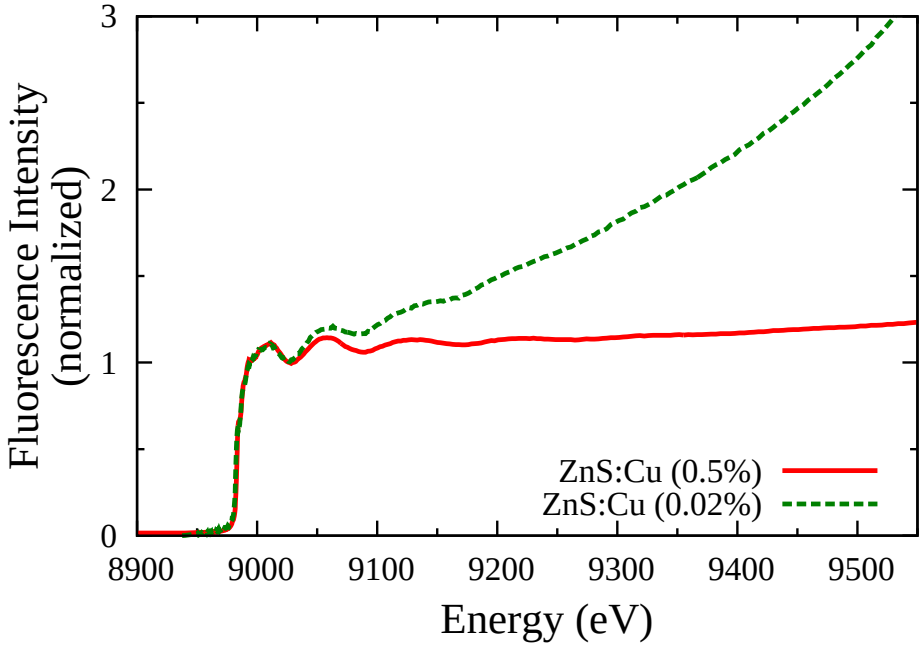

Figure 3.1: A comparison of the fluorescence E-space data at the Cu K-edge for two ZnS:Cu samples: an extremely dilute 0.02% Cu sample (dashed line) and a higher concentration 0.5% Cu sample (solid line). For comparison, the data were normalized at 9000 eV.

the oscillations—obtained from a fit of the data to a series of splines.[Teo, 1986; Koningsberger and Prins, 1988] This is quite straightforward for transmission data; for fluorescence data, however, the experimental $\chi_{exp}(E)$ is obtained from $\chi_{exp}(E) = I_f(E) - \bar{I}_f(E)/\bar{I}_f(E)$ where $I_f(E)$ is the measured fluorescence signal and $\bar{I}_f(E)$ is the average spline through the data. The corrected χ must be extracted from $\chi_{exp}(E)$ using some self absorption code (see Ref. [Booth and Bridges, 2005] for example). If $\bar{I}_f(E)$ increases with E, the amplitude of χ (corrected) decreases at high E and distorts the EXAFS signal.

Because fluorescence EXAFS typically uses a fairly narrow detector window

($\sim$ 200–300 eV wide for Cu) around the dopant fluorescence peak to eliminate other fluorescences and the scatter peak, the effect of the Zn Raman line here is more complex; the extra background arises from a convolution of the Raman line with the window used for data collection. As the energy is scanned for the Cu edge, the Zn Raman line grows in magnitude and its peak energy increases. The line passes through the window set up for Cu fluorescence and eventually would merge with the Zn fluorescence peak if the scan energy reached the Zn K-edge. To measure this effect, it is necessary to collect the background data the same way (with the same window) as the Cu fluorescence data are collected.

3.1.2 Subtraction Process

To quantify the effect, we replaced our ZnS:Cu sample with a Zn foil and scanned over the same Cu K-edge energy range (8740–9550 eV) with all other experimental parameters unaltered. This scan produced an increasing fluorescence signal as the energy increased towards the Zn K-edge, as shown in Figure 3.2. We then parametrized these data using a 6^{th} order polynomial and subtracted a constant background such that the resulting background function $\mathbf{B(E)}$ starts at zero at the beginning of the scan.

To correct the 0.02% Cu fluorescence data, (after a preliminary pre-edge subtraction), we multiply $\mathbf{B(E)}$ by a constant $\mathbf{a}$ such that this scaled background function has the same post-edge slope as the 0.02% Cu EXAFS data (to account for different sample thicknesses) and then subtract it from the fluorescence EXAFS data, obtaining

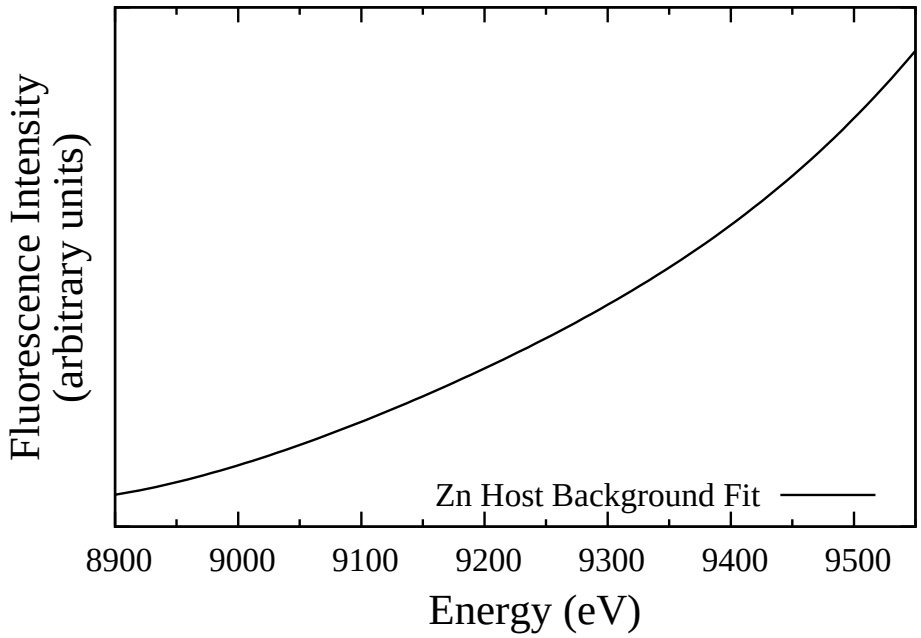

Figure 3.2: Fluorescence detector output for a Cu K-edge scan for a Zn foil sample, using the same parameters as for collecting Cu K-Edge EXAFS data in ZnS:Cu.

corrected data with a post-edge slope that is roughly zero. The background-subtracted data for 0.02% Cu are shown in Figure 3.3 as the dotted line. The corrected data can then be reduced using standard procedures such as RSXAP[Booth, 2012] to obtain k-space data and r-space data.

Although, for low concentrations, the Raman peak can be comparable to the fluorescence peak of the host atoms, resulting in artificially low k-space data at high k and, therefore, an erroneously large value for sigma, it can easily be removed to minimize these distortions in the EXAFS data and obtain the proper magnitude at high k and a correct value for sigma.

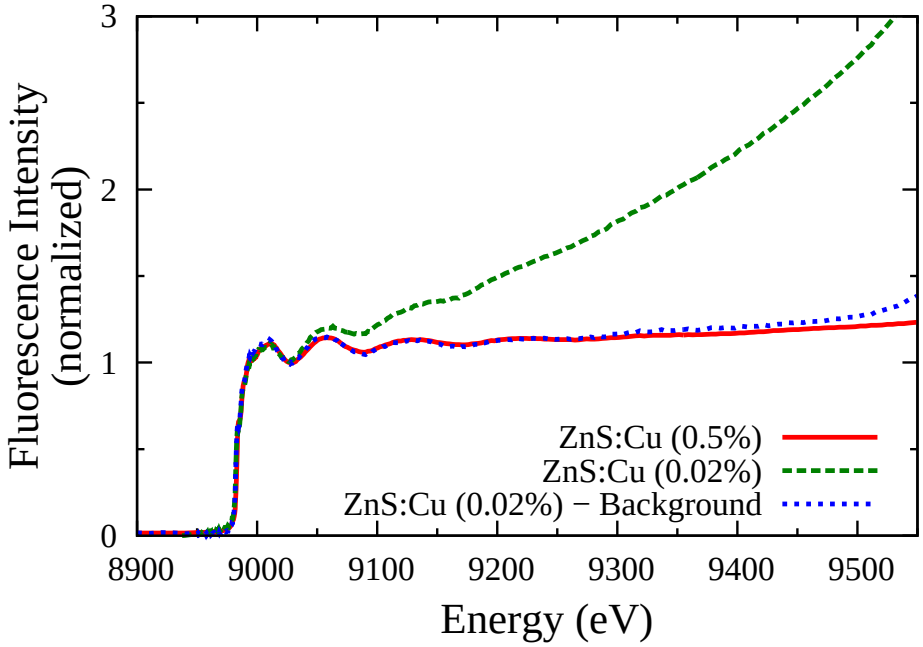

Figure 3.3: The normalized, background-subtracted dilute 0.02% Cu sample, compared to the original dilute data and to the higher concentration 0.5% Cu sample.

3.1.3 Alternate Subtraction Process

In certain situations, it can be difficult or impractical to fit the Raman background and, therefore, an alternative subtraction process is necessary. There are a number of alternate methods to remove this background. For example, it is possible to obtain a spline from the reference data or it is possible to simply use the smoothed, interpolated reference data. We tested interpolating the reference data (using a simple gaussian weighting over a number of nearby points) and have found that this results in equivalent values for the reference data (results are not shown due to the lack of a significant difference compared to the process in Figure 3.3).

3.2 X-ray Magnetic Circular Dichroism

3.2.1 Motivation

XMCD is typically performed at the L2 and L3 edges of 3d transition metals, though it also occurs in the K edges of many elements and the M4 and M5 edges of 4f rare earth metals. When a circularly polarized photon is absorbed by an electron, the photon transfers its angular momentum to the photoelectron. Depending on the original state of the electron, this angular momentum can be transferred to the electron's spin, angular momentum, or both.[Schütz *et al.*, 1987; J. Stöhr, 1999]

Since spin flips are forbidden in electric dipole transitions, photoelectrons from a p core shell (L2 or L3 edges) can only be excited into d hole states with the same spin and photoelectrons from an s core shell (K edge) can only be excited into p hole states. Thus, in either case, the X-ray absorption is modulated by the availability of empty hole states with the appropriate angular momentum, and the difference between the XAS with circularly polarized X-rays parallel to and antiparallel to the applied magnetic field makes it possible to probe them independently.

Thus, XMCD performed at the K edge reveals information about the orbital moment μ_L and XMCD at the L2 or L3 edge, provides information about both the orbital moment and the spin of the empty states. XMCD's sensitivity to angular momentum, combined with the elemental specificity intrinsic to XAS techniques, makes is invaluable in the understanding of magnetic properties of materials.

3.2.2 Analysis Technique

To collect data to be used in XMCD, it is necessary to take four sets of data: one for each combination of positive or negative magnetic field and left or right circularly polarized X-rays. At the APS, the file from each scan was for a given magnetic field and contained a column for both left and right circularly polarized X-rays (having taken the data one after another for each X-ray polarization before proceeding to the next energy).

To reduce the data for each individual scan, we first divide the XAS columns by I0, subtract a background and normalize the XAS columns to 1 at some energy E_0^+ well above the edge. (This gives us $N = \frac{I_f}{I_0}(E)/\frac{I_f}{I_0}(E_0^+)$.)

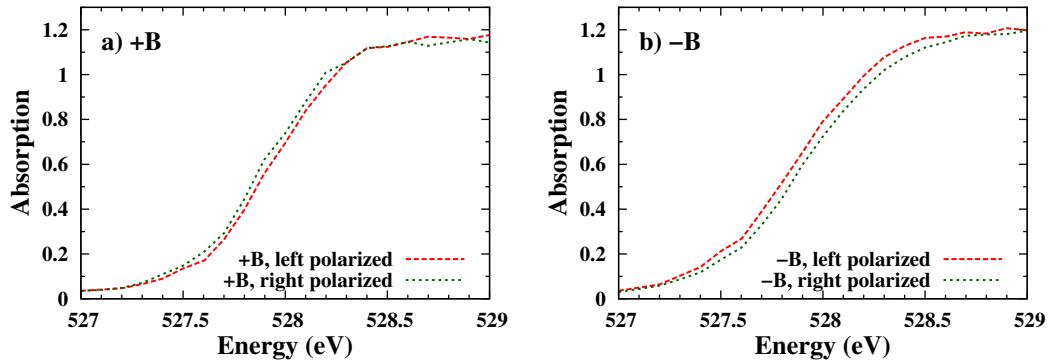

Figure 3.4: XMCD data at the O K edge, during data analysis. Example is for $La_{0.85}Sr_{0.15}CoO_3$.

Figure 3.4 shows an example of what the data looks like zoomed in at the edge region at this point in the data analysis. The next step is to correct for the florescence self-absorption, using the formula from Haskel [1999]:

$$\frac{\mu_e(E)}{\mu_e(E_0^+)} = \frac{\frac{\frac{I_f}{I_0}(E)}{\frac{I_f}{I_0}(E_0^+)}\left(\frac{\mu_t(E_f)}{\mu_e(E_0^+)}\frac{\sin\theta_i}{\sin\theta_f}+\frac{\mu_b(E)}{\mu_e(E_0^+)}\right)}{\left(\frac{\mu_t(E_f)}{\mu_e(E_0^+)}\frac{\sin\theta_i}{\sin\theta_f}+\frac{\mu_b(E_0^+)}{\mu_e(E_0^+)}+1\right)-\frac{\frac{I_f}{I_0}(E)}{\frac{I_f}{I_0}(E_0^+)}} \quad (3.1)$$

$$= \frac{N\left(\beta\frac{\sin\theta_i}{\sin\theta_f}+\gamma(E)\right)}{\left(\beta\frac{\sin\theta_i}{\sin\theta_f}+\gamma(E_0^+)+1\right)-N} \quad (3.2)$$

Where μ_e is the absorption of the specific edge, μ_b is the background absorption (including from other edges in the same element), $\mu_t = \mu_e + \mu_b$ is the total absorption, and E_f is the fluorescence energy. Thus for convenience, β is defined as the ratio of the total absorption at the fluorescence energy over the edge absorption at the normalization energy and $\gamma(E)$ as the background absorption at the incident X-ray energy E over the edge absorption at the normalization energy. The net effect of this correction is shown in Figure 3.5.

The next step in calculating the XMCD is converting the left and right circularly polarized XAS data columns into an average XAS data columns and a difference XAS data column.

After doing that to all of the data files, we average together the sweeps with both identical samples and identical B fields. For the pairs of sweeps with opposite applied magnetic fields, we further average the average columns and subtract the difference columns. This results in a final average XAS and the XMCD. (Note that we do a two-step average in case some of the samples do not have the same number of +B sweeps as –B sweeps.) This final step is performed in order to cancel out any artifacts.

Figure 3.6 shows an example of what the data looks like zoomed in at the edge

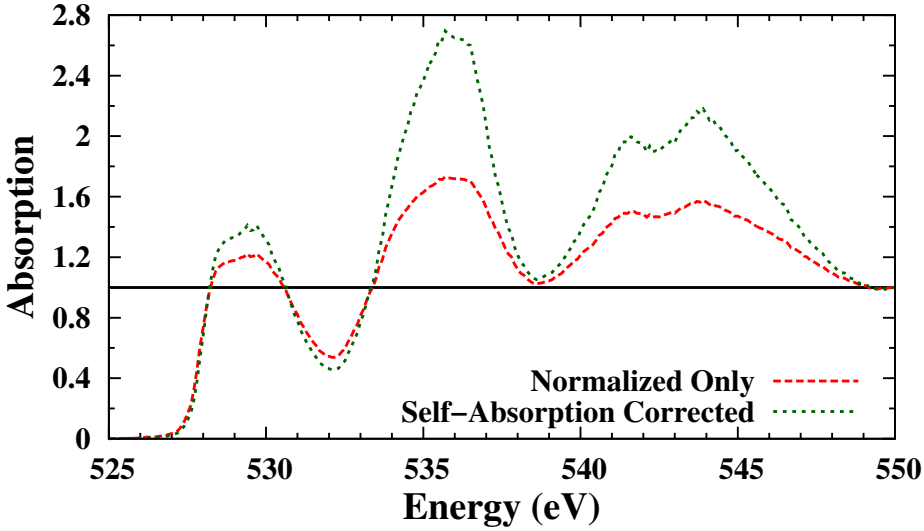

Figure 3.5: Example showing the effect of the fluorescence self-absorption correction for $La_{0.85}Sr_{0.15}CoO_3$ at the O K edge. The horizontal black line is at 1, and makes it clear that, for normalized data > 1, the value of the corrected data increases while, for normalized data < 1, the value decreases further.

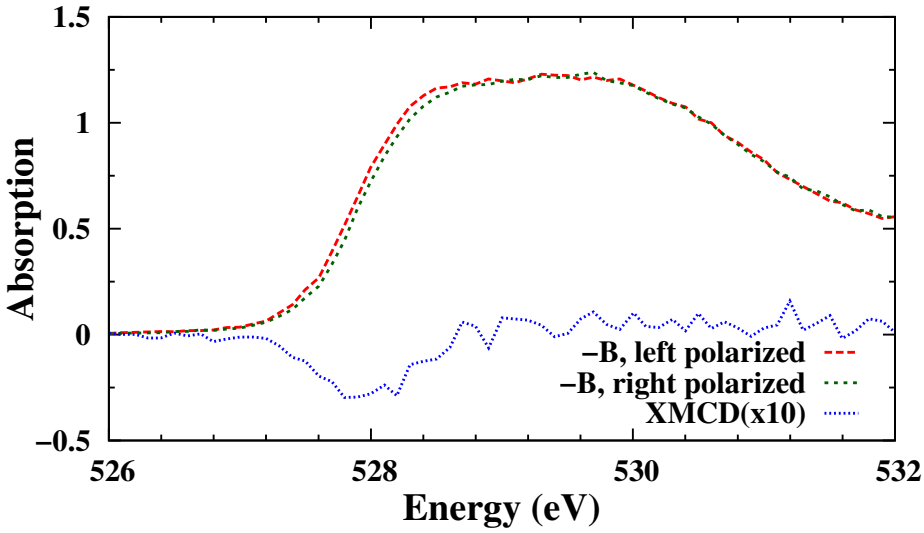

Figure 3.6: The final, reduced XMCD data at the O K edge of $La_{0.85}Sr_{0.15}CoO_3$ and two of the original traces.

region at this point in the data analysis. Since the XMCD signal is small, it is often multiplied by 5 or 10 (as is the case here) to make it easier to compare it's location to the original XAS.

At this point, we can subtract the average XAS for a given sample from a reference sample and/or can integrate the areas under various sections of the XMCD curves.

Chapter 4

ZnS:Cu Phosphors

4.1 General Introduction

Doped ZnS phosphors such as ZnS:Cu,Cl have been studied for low-cost, non-toxic solid-state lighting applications since the 1930s when Destriau discovered their electroluminescence (EL) under AC excitation.[Destriau, 1936] These materials exhibit AC EL at much lower applied voltages than is required for DC EL. For a relatively thick 50 μm layer, voltages of only 100 VAC are required, two orders of magnitude lower than for DC EL.

Extensive research in the 1950s and 1960s culminated in the best experimental observations and mechanistic theory by Fischer in 1963.[Fischer, 1962, 1963] Fischer observed that light emission was in the form of alternating emission from either end of a linear structure within the individual ZnS:Cu,X phosphor particles, shown in Figure 4.1. At Cu concentrations above $\sim 0.04\%$, Fischer proposed that most of the Cu precipitates

out along [111] crystal imperfections or grain boundaries during the cooling phase in fabrication. These conducting CuS inclusions have a needle or disc like shape that causes a local electric field enhancement of up to a factor of 100 near the tips. The remaining Cu dopants that do not precipitate out form hole-traps, at least some of which have been shown to be in Cu complexes with C_{3v} symmetry, from Raman spectroscopy measurements.[Urabe *et al.*, 1968] Meanwhile, isolated Cl (or Br or Al) co-dopants form shallow electron-traps.

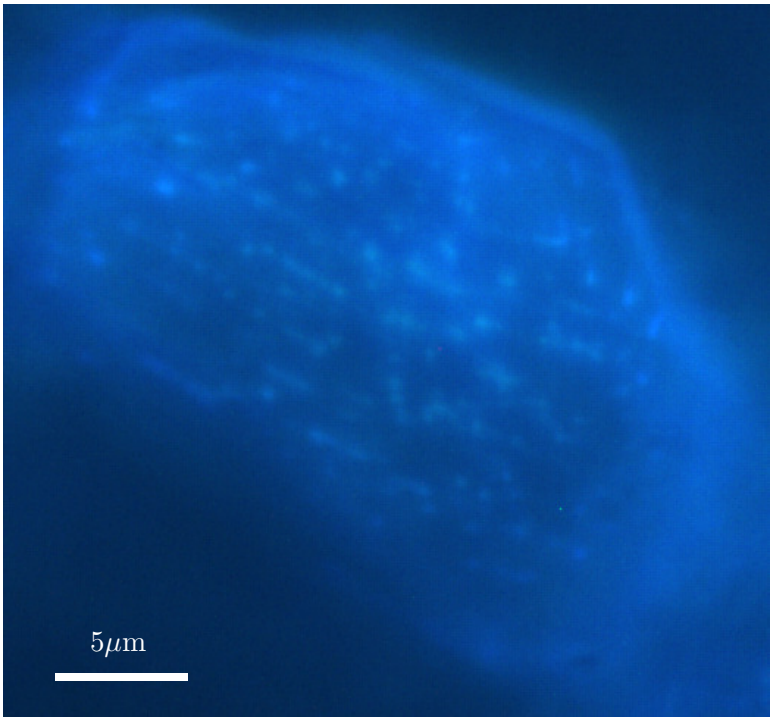

Figure 4.1: A 20 μm particle with the individual emission centers visible.

It is believed that the optical emission is due to electron-hole recombination from the electron and hole trap sites (diagram shown in Figure 4.2) which are in the

high field region in the vicinity of the tips of the CuS precipitates. With AC excitation, electrons and holes are injected into the ZnS in equal numbers via field emission from opposite ends of the CuS nano-precipitates and are trapped in their respective trap sites. Each time the field is reversed, some of these injected electrons recombine with holes trapped during the previous half cycle, emitting light.[Fischer, 1963] Analysis of the EL spectrum reveals the presence of four separate emission lines: three blue lines and one weaker green line. It is believed that the existence of more than one type of trap state helps to explain the presence of these four different emission lines.[Tanaka *et al.*, 1999; Shionoya, 1999]

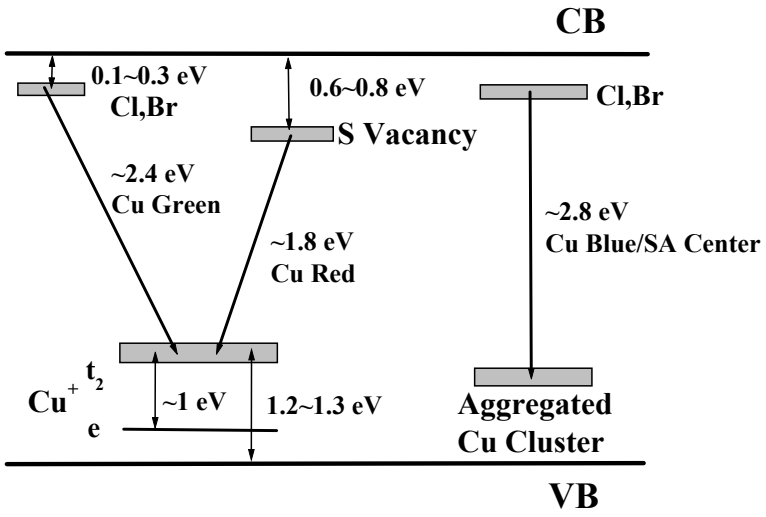

Figure 4.2: A band diagram of various trap states in ZnS:Cu,Cl/Br, showing several proposed emission mechanisms.[Stanley *et al.*, 2010]

In order to better understand ZnS:Cu phosphors for AC EL applications, it is also useful to study their photoluminescence (PL) properties. In a simple picture, the PL of the phosphor is fundamentally similar to the EL, except that the electrons

and holes are excited optically instead of electrically, and therefore do not require being encapsulated into a device. In PL, the blue line generally dominates but a green line is also observed[Suzuki and Shionoya, 1971] while in EL three major, closely-spaced, blue/green lines are observed plus a weak (2–3%) narrow line.[Stanley *et al.*, 2010] Some have also reported a red line in bulk ZnS:Cu when there are significant S vacancies present.[Shionoya *et al.*, 1966] Also, a number of metal ions, such as Mn^{2+}, Cu^{+}, Pb^{2+}, Ag^{+}, and Eu^{2+}, can be doped into ZnS to produce PL or EL emission in different regions of the visible spectrum.[Morozova *et al.*, 1985; Soo *et al.*, 1994; Kishimoto *et al.*, 2000; Chen *et al.*, 2000; Yang *et al.*, 2001; Khosravi *et al.*, 1995; Jiang *et al.*, 2009a]

4.2 Time-Lapse Microscopy

4.2.1 Degradation Background

Unfortunately, the usefulness of doped ZnS phosphors for high brightness applications is limited by the fact that the devices degrade to 10% of initial brightness over a short 20 hours when run at 100 kHz.[Thornton, 1960; Lehmann, 1966] Previous studies have shown that degradation proceeds faster at higher applied frequencies and when the device is run at higher temperatures.[Lehmann, 1960; Thornton, 1956; Bol *et al.*, 2002; Stanley *et al.*, 2010] After degradation, the devices can be rejuvenated back to 70–80% of initial brightness by annealing for about an hour at 185°C, with higher temperatures or longer times both resulting in a gradual decrease of EL. Further, devices can be degraded and annealed multiple times, each time permanently losing 20–30% of

the initial brightness, until it is no longer worthwhile.[Stanley *et al.*, 2010] However, the degradation mechanism or mechanisms remains an unsolved problem even after more than 50 years.

The degradation and ability to subsequently rejuvenate, along with the fact that degradation of the material does not occur over long times under comparable applied DC fields ($\sim$ 100 V DC) suggests that some type of electric-field enhanced diffusion during field switching in AC operation is primarily causing the degradation. These microscope images show the AC EL emissions of 4–6 particles. Some popular degradation mechanisms include: sharp CuS tips becoming blunted, decreasing numbers of hole and/or electron trap sites (Cl, Br, or Al co-dopant) in the high field region about the CuS nano-precipitates, Cu complexes (hole trap sites) becoming damaged, and local damage to the ZnS host.

Previous studies of electroluminescent degradation focused on the device as a whole, using the entire light output from thousands of particles, each containing dozens of individual emission centers.[Stanley *et al.*, 2010; Warkentin *et al.*, 2007] However, observing images taken during degradation, it was found that the number of visible emission centers decreased as the device degrades.[Stanley *et al.*, 2010] It is not known whether each emission center's light output decayed in the same way or if some sites decayed faster than others, leading to the above observation. Due to the fact that the CuS nano-precipitates vary in size and orientation, the local electric fields must vary significantly throughout the device. Thus, it would not be surprising if individual emission centers simply degraded at different rates.

In this work, we investigate the degradation of many individual emission centers in a a number of bulk particles ($\sim$ 20–30 μm) for several devices. Using an oil immersion optical microscope with a magnification of 60$\times$ and a depth of focus of about 10 μm, we took 4 second exposures at intervals ranging from every 5 seconds (at the beginning of the degradation) to every minute (towards the end of the degradation) for 24–100 hours, giving us about 2000 images per degradation. Some preliminary results from one run were presented in a conference proceedings.[Bridges *et al.*, 2010b] There we noted a few bright points that turned off and on. Here we show that this is a much more general behavior and occurs over most of each particle. We took two separate approaches in analyzing these extensive data sets.

4.2.2 Device Preparation

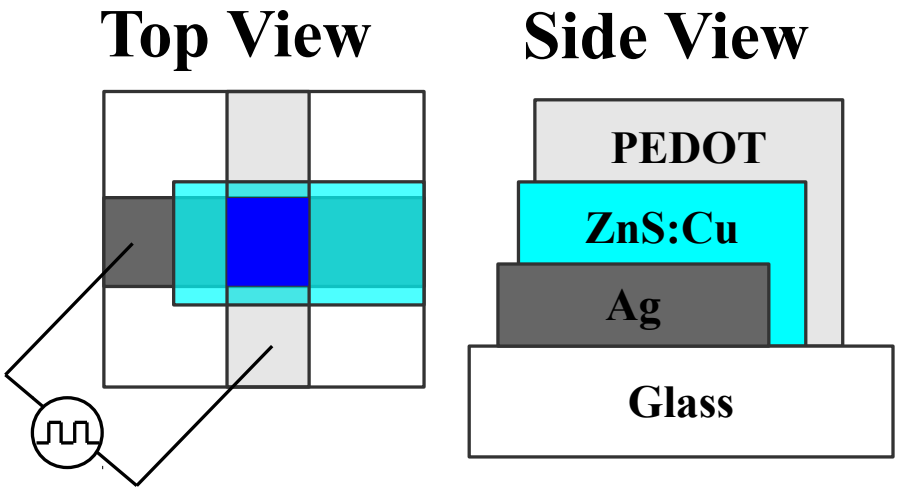

Figure 4.3: Two views of fabricated devices. Active area is the dark blue region in center of top view.

AC EL devices were fabricated using commercially available blue-green emitting ZnS:Cu,Cl phosphor from Osram-Sylvania and Osram-Sylvania EL binder with a superstrate device structure on glass, as seen in Figure 4.3. Phosphor material was mixed with binder by mass at a ratio of m_{ph}/m_{bi}=0.55±0.02, and each layer was doctor bladed onto glass slides using a razor blade. Two pieces of Scotch tape were used to control the wet film thickness. Slides were annealed in a vacuum oven at 110°C and ∼ 1 Torr for 30 minutes. Silver paste and PEDOT contact layers were applied (perpendicular to each other) using the same technique. Completed active device area was 3 mm by 3 mm.

4.2.3 Intensity Measurements

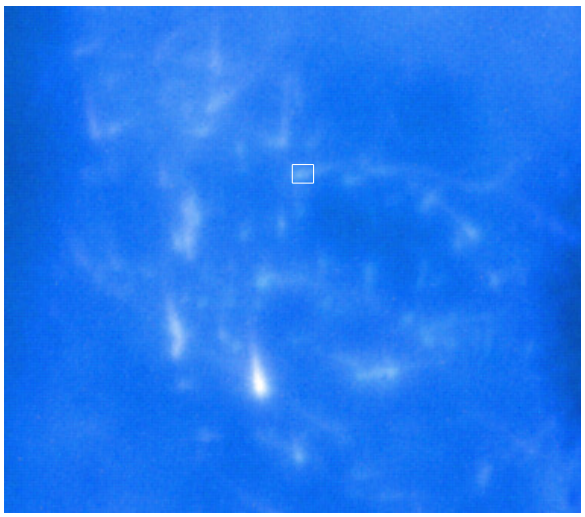

Figure 4.4: A small phosphor particle (∼ 15 μm) from within a larger image. Note that the resolution of the emission centers is limited by diffraction; the actual emission centers are likely much smaller than they appear. The white box indicates an example integration region, of which this particle would contain about 20.

In Figure 4.4, we show an image cropped to a single, small particle, showing it's AC EL emission. In each series of exposures, we identified a large number of emission centers (40–80 total per image) by looking at several images—not just the initial image. Then, we integrated the number of counts within a 0.5–1.0 μm^2 ($\sim$ 150 pixel) rectangle around each point, as shown in Figure 4.4. We next plot the intensity as a function of time for each identified emission center. While the light output from some emission centers decayed in rough agreement with the exponential decay for the device as a whole,[Stanley *et al.*, 2010] these accounted for fewer than 50% of the emission centers. Instead, most individual emission centers exhibit sharp changes in their light output.

In Figure 4.5A and 4.5B we plot the intensities for several emission centers with monotonically decreasing luminosity, including sharp drops. In many cases (including the drop shown in Figure 4.5B), all of the drop occurs in less than the time between exposures (5–60 sec); even in cases (such as Figure 4.5A) where the drop takes place over the course of several exposures, it is still quite short compared to the hours-long device degradation. However, these sharp drops were not the only unexpected behavior visible. Some of the emission centers also showed sudden increases in luminosity, often turning off and back on several times during the device degradation, as can be seen in Figure 4.5C and 4.5D. In Figure 4.5C, note that there are two small, rapid blinks, slightly later in the degradation (between 12 and 15 hours) and two shorter blinks within the inset. In 4.5D, the increase in intensity near 30 hours seems to be equal to several of the previous drops. Often, this blinking happens at the end of the life of that emission center, but in some cases (as in 4.5C) the emission center continues to emit light for a

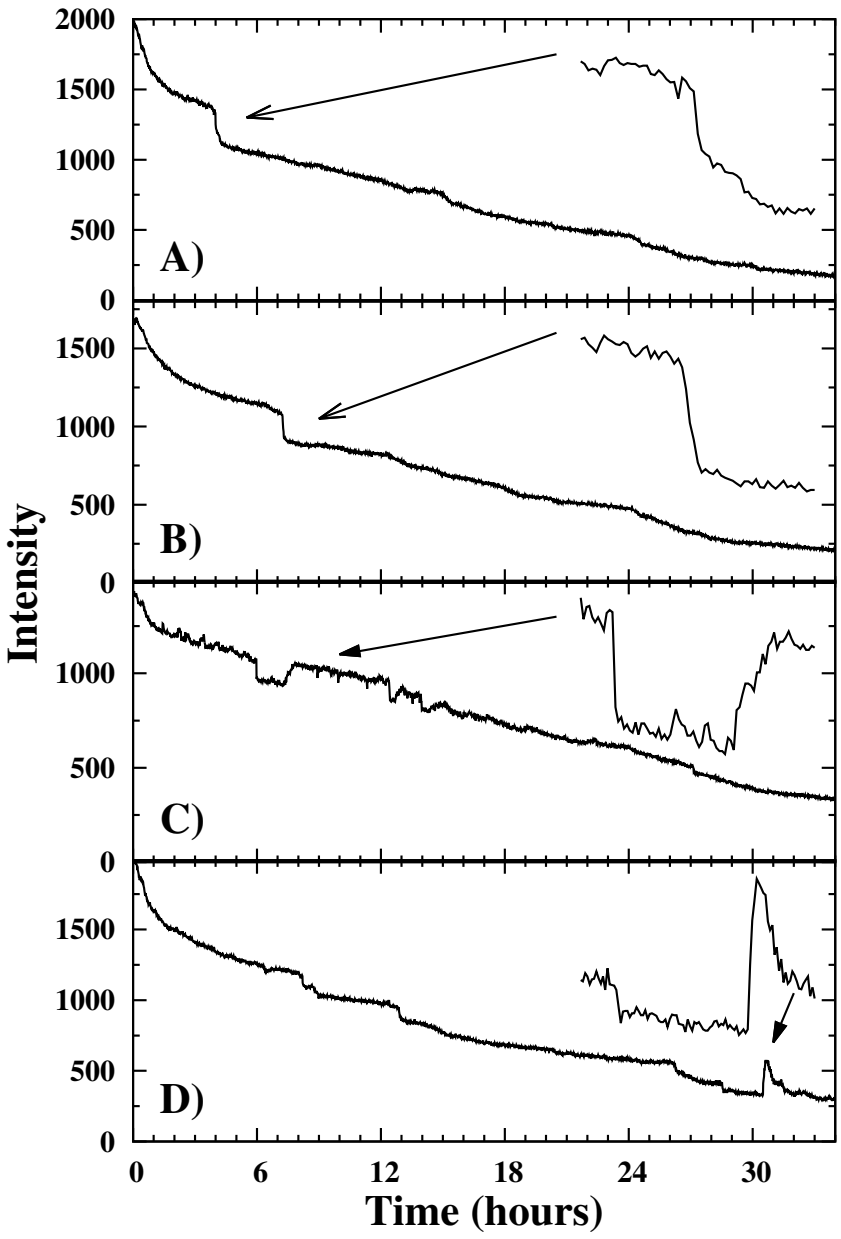

Figure 4.5: Intensity for several emission centers, with enlarged inserts showing the occasionally abrupt behavior in detail. In A and B we see only gradual decay and sharp drops in luminosity, while in C and D we also see large increases in luminosity, or blinking.

long time after blinking.

Unfortunately, the large variations in the scattered light within each particle result in a background which varies greatly with both time and locations, prevented us from being able to accurately subtract off the background to truly isolate the individual emission centers. Thus, it is unclear how much of the smooth decaying behavior is due to the individual particle gradually dimming, versus scattered light from elsewhere in the device creating a slowly decaying background.

This method clearly worked well when the device did not move throughout the data collection. However, due to the fact that many individual emission centers blinked off and on repeatedly, it was not feasible to implement drift-tracking and to produce graphs for those devices that, for one reason or another, had drifting of the optical system during the course of the data collection.

4.2.4 Video Analysis

Our second approach was to take crops of 5–8 individual particles within each image and combine them into a video at 30 fps, speeding up the degradation by a factor of 150. This made it easy for the naked eye to pick out emission centers—even dim or slightly unfocused ones—that are turning off, turning on, or blinking on and off. Excerpted individual (original) frames showing this blinking are presented in Figure 4.6. Full videos can be found online at http://exafs.ucsc.edu/acel/.

These videos show that over the entire area of each particle there are significant intensity fluctuations—*i.e.* at some point in the decay, nearly every emission center

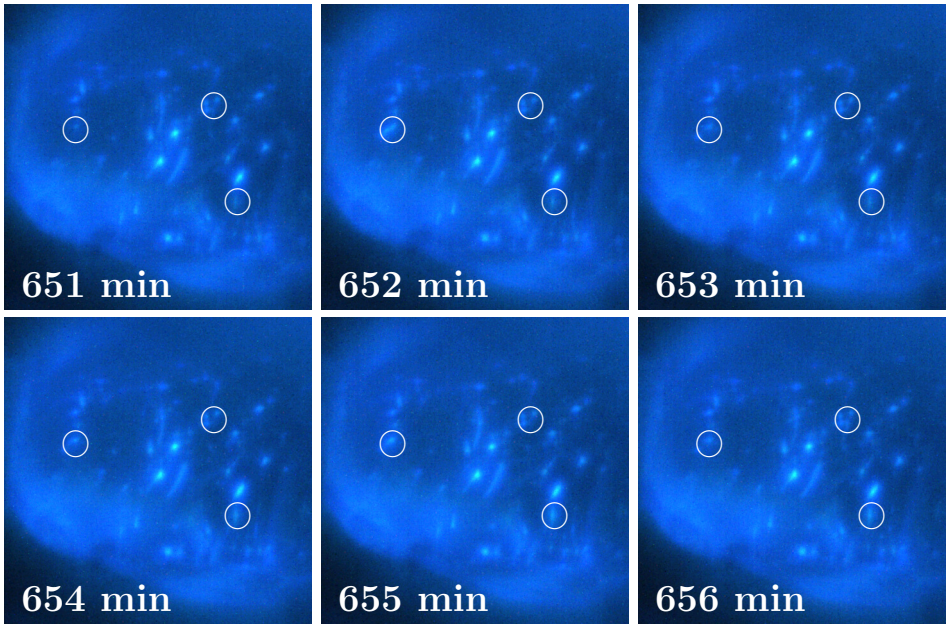

Figure 4.6: Several images of the same particle over a short period. The circles are around emission centers with significantly fluctuating intensities. The circle at the left, in particular, is an example of an emission center that turns on and off twice within 5 minutes (on in 652 and 655). The top right circle contains 3 emission centers until 656 when another turns on and it contains four. The bottom right circle increases in brightness gradually from 651 to 655. This 5 min example is typical of many particles over their entire degradation.

shows significant intensity fluctuations. Thus the videos, and to a lesser extent the short sequence of still images in Figure 4.6, makes it clear that the phenomenon graphed in Figure 4.5 is not limited to one or two of the strongest emission centers in a few particles or devices, but occurs for most emission centers in every phosphor particle—it is a universal behavior.

4.2.5 Discussion

The extensive plots of intensity vs time for hundreds of emission points provides a new assessment of the degradation and provides a means of evaluating several distinct proposed degradation mechanisms, listed in Table 4.1. The fact that there are two primary degradation methods (sudden changes, down and up, and gradual decay) suggests that at least two different degradation mechanisms play major roles, and at least one of them is rapid and can be partially reversible. The rapid changes suggest a threshold effect and the ability to spontaneously start emitting again suggests that randomness is a significant factor.

The proposed blunting of the tips of the CuS nano-precipitates, which would cause a decrease in the electric field amplification, would be gradual and irreversible. Local damage to the ZnS host would also be gradual and, while it is expected to be reversible by annealing, it would be extremely unlikely to occur spontaneously during degradation. Diffusion of the trap sites out of the high field region would be reversible, but not rapid enough (due to the fact that it would take many hops, each with a random component, to exit the high field region).

Proposed Mechanism	Rapid?	Reversible?
Tip Blunting	No	No
Trap Migration	No	Yes
Damage to Complexes	Yes	Partially
Host Damage	No	Only Under Anneal

Table 4.1: Summary of the features of proposed degradation mechanisms. Only damage to complexes can be both rapid and reversible, due to individual atoms hopping short distances.

To a lesser extent, the long-scale fluctuation in the degradation, as in Figure 2B at ∼12 hours and Figure 2C at ∼ 24 hours, suggest a process that is gradual and has a random component, such as the migration of single-atom trap states. Thus, the smooth decay that can be seen in every emission center is probably due to single-atom trap states slowly diffusing out of the local high field region, and suggest that the migration of trap states plays a larger role in the gradual degradation of the phosphor than tip blunting or damage to the ZnS host.

If some of the trap states are complexes, formed of several atoms or vacancies, the movement of a single atom or vacancy only a short distance away from the complex center might damage a complex site and thereby quench emission. Thus, the large rapid changes are most likely caused by damage to complex sites. Further, if a complex can be turned off by one of the atoms moving away from the cluster, then rapid blinking could easily occur if that atom hops back and forth. However, if one of the complex atoms/vacancies diffuses several lattice sites away from the complex, the site may become permanently damaged and not easily rejuvenated even by annealing. In addition, it has been proposed that if another defect diffuses to an active emission center, it might quench the strong emission. One suggestion,[Roberts, 1957] for example, is that if Cl^- diffuses close to a Cu, that site might become inactive. Such a quenching would also be rapid if it takes a single hop for the extra defect to join the active site; one cannot differentiate between an atom leaving or joining a Cu complex—thereby causing a rapid quenching—or blinking if that atom hops back and forth between two sites.

Of the various degradation mechanisms proposed to date, only damage to the

Cu complex is rapid and can be reversible, and thus we conclude that it must play the primary role in the apparent blinking off and on of individual emission centers and likely plays a significant role in the degradation of the device as a whole.

4.3 Ground Phosphors

4.3.1 Background

Despite the fact that AC EL occurs at average applied field strengths two orders of magnitude below DC EL, typical commercial phosphors (made with particles 20–30 μm in diameter) still require several hundred volts peak-to-peak for full efficiency.

A simple means to decrease the required applied voltage would be to decrease the film thickness, but requires smaller powder particles. Though AC thin-film EL has been studied extensively[Shionoya, 1999] and nanoparticle AC EL devices have recently been reported,[Wood *et al.*, 2009] neither of these technologies utilizes the local electric field enhancements found in ZnS:Cu,Cl powder AC EL devices.

Devices made using commercially available ZnS:Cu phosphors without further processing have a minimum device thickness of $\sim$ 50 μm before the thickness becomes too nonuniform and the devices short out.[Medling *et al.*, 2011] However, commercially available AC EL ZnS:Cu phosphor particles can be milled to produce smaller phosphor particles, which can then be used to fabricate thinner AC EL devices that still contain field enhancements from the CuS nano-precipitates.[Faria, 1988]

Here we show that good EL at somewhat lower voltages is possible for lightly

ground ZnS:Cu particles, but thin films made using heavily ground particles have a very weak output. Moreover, when the particles were size sorted, no significant EL output ($<$ 1%) was observed for the particles ≤ 2 μm in diameter. To understand these changes in the EL output with decreasing particle size we have carried out EXAFS measurements to probe any significant disorder in the ZnS:Cu,Cl particles as a result of grinding. We show that for the size selected particles there is a large increase in the disorder about the Cu sites but no observable change in the disorder about the Zn atoms in the ZnS lattice.

4.3.2 Electroluminescence Studies

Commercially available EL ZnS:Cu,Cl phosphor powders were milled using a FRITSCH Pulverisette 7 planetary micro mill with 5 mm hardened steel beads. To ensure minimal thermal degradation, all milling was carried out in multiple cycles, with each cycle shorter than 2 minutes and an equal rest cycle between cycles. AC EL devices were fabricated using as-made and milled commercially available blue-green emitting ZnS:Cu,Cl phosphor from Osram-Sylvania (GGL21 and GGS22). Phosphor material was mixed with Osram-Sylvania EL binder by mass at a ratio of m_{ph}/m_{bi}=0.55$\pm$0.02 and doctor bladed onto Indium Tin Oxide (ITO) patterned glass slides using Scotch® tape or thin Mylar® to control the wet film thickness. Slides were annealed in a vacuum oven at 110°C and $\sim$1 Torr for 30 minutes. A silver top electrode was applied perpendicular to the lower ITO electrode using similar methods. Completed active device area was 3.0 mm by 6.4 mm.

Room temperature photoluminescence (PL) measurements were made on films deposited on glass slides using a Perkin-Elmer LS45 spectrophotometer. The set-up for PL collected a small solid angle of the fluorescence emission and provided a reproducible shape for the spectra; however, the amplitude was quite sensitive to scattering from the sample surface and varied considerably as the sample was changed or moved. For AC EL, the devices were driven by a HP 3245A power supply with sinusoidal waveforms, while light output was measured either by an Ocean Optics SD2000 optical spectrometer for spectral information or by a Si photodiode connected to a Keithly 425 Picoammeter for automated frequency or voltage sweeps. In this case, an optical fiber was placed close to the device under measurement and collected the emission from a large fraction of the subtended solid angle; for this set-up, the output was relatively insensitive to small motions of the sample and relative intensity measurements were reproducible to a few percent. Also note that under AC operation, the devices are nearly perfect capacitors and we were not able to reliably measure the in-phase current even using lock-in techniques; hence we cannot provide an estimate of the power efficiency.

Dry film thicknesses of phosphor layers were measured to an accuracy of ± 5 μm (before the silver contact was applied) with a vernier micrometer and averaging over several locations on the device. Scanning electron microscope images of phosphor powders were obtained using an ISI WB-6 SEM.

The effects of milling on emission intensities are summarized in Table 4.2. Both the GGL21 and GGS22 phosphors showed similar behavior after milling, with the EL and PL emission spectra unchanged.[Medling *et al.*, 2011] Milling speeds of 100

Phosphor	Speed	Time	EL Intensity
GGL21	200RPM	2 min.	86%
GGL21	400RPM	2 min.	16%
GGL21	400RPM	4 min.	2%
GGL21	400RPM	8 min.	3%
GGS22	100RPM	10 min.	100%
GGS22	200RPM	2 min.	86%

Table 4.2: Summary of EL results for various micro milled ZnS:Cu,Cl phosphors. The relative EL intensity was obtained by comparing photodiode current at 160 V_{pp} excitation for the as ground material.

RPM produced minimal effects on phosphor powder. The powder's visual appearance, EL emission, and PL emission were virtually unchanged. Milling speeds of 400 RPM produced a very fine, sticky powder. These powders showed a significant decrease in PL and EL emission. Milling either phosphor at 200 RPM for 2 minutes produced a powder with a finer consistency than as-made, yet still retained significant PL and EL emission.

Lightly milled samples contain mostly large particles which have smooth crystal surfaces while strongly milled samples mostly contain many small particle fragments with rough damaged surfaces. Figure 4.7 shows an SEM image of a medium ground sample, with a mixture of particle sizes and surface roughness.

Figure 4.8 shows AC EL intensities for three thicknesses of devices produced with milled phosphor and optimal as-made phosphor. Gains of nearly a factor of 5 were obtained for a 25 μm thick device from milled particles compared to a 58 μm device of as-made particles for 40 V_{pp}, 20 kHz excitation. This emission gain at low voltages was robust across frequencies of 200 Hz – 80 kHz excitations, as shown in Figure 4.9,

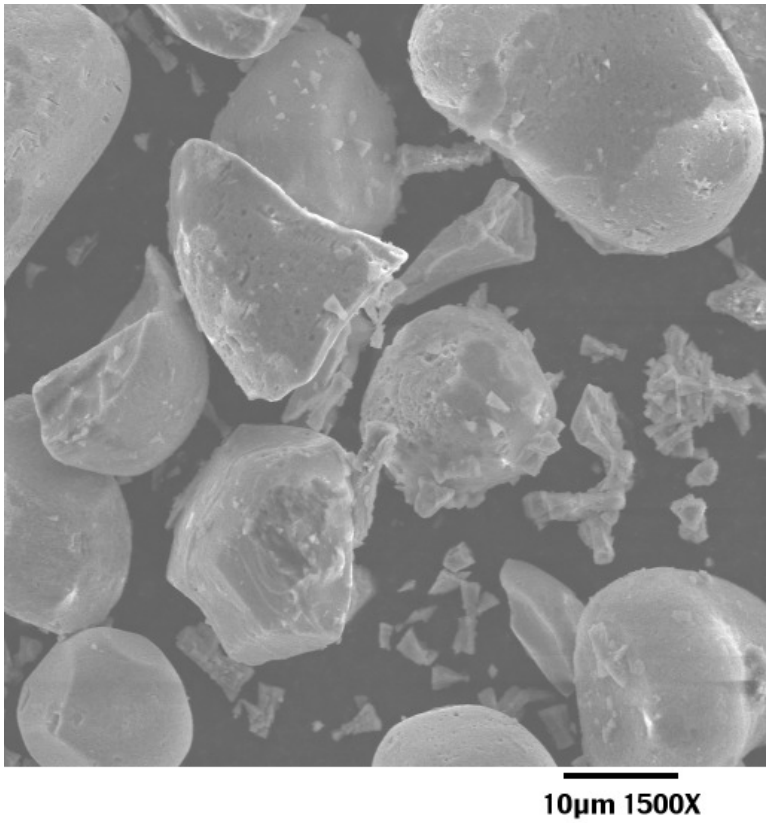

Figure 4.7: Ground particles viewed using a scanning electron microscope showing a large number of large 10–15 μm particles, a few nearly unground particles, and a few below 3 μm. The ground particles are then size-separated prior to EXAFS analysis.

but output of the as-made device approached that of the thinnest milled device as the driving voltage exceeded 100 V_{pp}, shown in Figure 4.8 inset.

It is not clear from the emission why there is such a significant decrease in AC EL for the smallest particles, particularly when AC EL has been observed for nanoparticles of ZnS,[Wood *et al.*, 2009] though the emission mechanism might be different. To reduce the AC EL intensity either 1) the emission centers—electron traps on Cl^{-1} and hole traps on complex Cu centers—are damaged during grinding, 2) the CuS needle-like

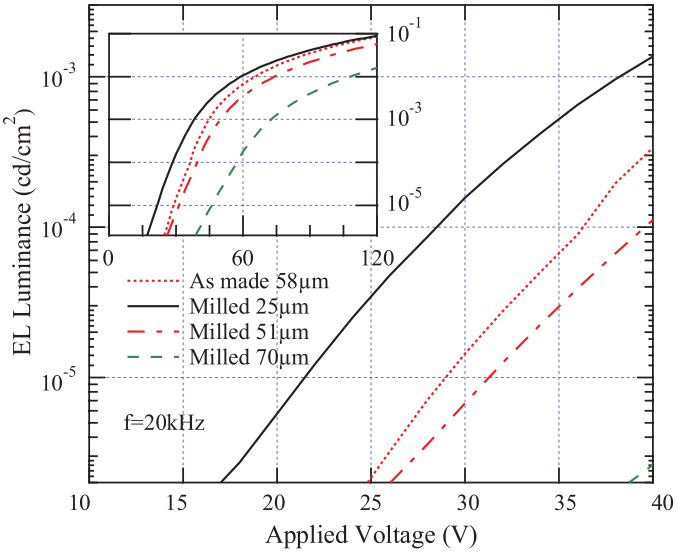

Figure 4.8: AC EL luminance as a function of applied voltage at 20 kHz for a 58 μm thick as-made device and devices of various thickness made from phosphor milled at 200 RPM for 2 minutes (GGL21). Main figure shows range of maximal enhancement while the inset shows a broader voltage range.

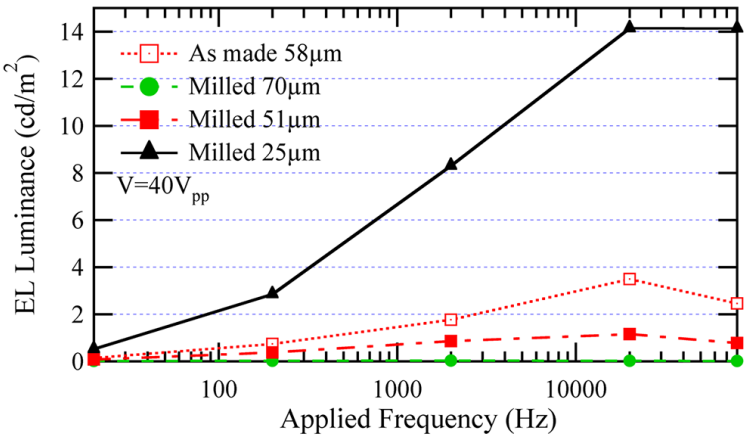

Figure 4.9: AC EL luminance as a function of applied frequency at 40 V_{pp} excitation for a 58 μm thick as-made device and devices of various thickness made from phosphor milled at 200 RPM for 2 minutes (GGL21).

precipitates are damaged, diminishing the local E-field enhancement, 3) both 1 and 2 occur, or 4) the size of the host ZnS particle plays an unknown but significant role.

4.3.3 Local Structure Measurements Using EXAFS

We used the EXAFS technique to investigate the extent of any grinding-induced local structure changes about Cu, Zn, and Mn in ground materials of ZnS:Cu,Cl (GGL21) and ZnS:Cu,Mn,Cl (GGL11). EXAFS is particularly appropriate for these systems because it can detect small changes in local distortions about very dilute dopants such as 0.15% Cu in these samples. The atom of interest (Cu, Mn, or Zn) is selected by using the corresponding X-ray absorption edge for that element.

The first EXAFS experiments were on the as-ground materials discussed above, and indicated that there was increased distortion about the Cu sites. Unfortunately, these first EXAFS results were not conclusive as the amount of distortion varied considerably from sample to sample. However, the SEM images show that even the heavily ground phosphors contained a mixture of various size particles including a few large particles (as in Figure 4.7). Because of the large volume, such particles can dominate over fine particles in EXAFS spectra. In order to have more uniform-sized samples to investigate, the ground particles were size sorted into three groups: large (15–30 μm), medium (3–15 μm), and small ($\sim$ 1–3 μm).

The size separation process began with four 2 minute, 200 RPM grinding cycles each consisting of 1 minute of grinding in the planetary micromill and 1 minute of cooldown. The particles were then suspended in distilled water and placed in a 1000

mL beaker with a 3" magnetic stir bar. The smallest particles were extracted from the top 50% of then solution after letting it sit for 15 minutes with no stirring; the medium-size particles were extracted while stirring with a vortex of depth 25% of the solution; the large particles were extracted from the remaining, unsuspended powder. Two intermediate extractions were also performed, one between small and medium with stirring but no vortex and one between medium and large with a vortex depth of 50%, in order to provide increased differentiation between the sorted sizes. For the final size-sorted samples for EXAFS analysis, we then used a 25 μm sieve to remove any remaining large particles as they could dominate the EXAFS. In practice, we've found that this sieve passes small particles very well but only a few particles in the 10–25 μm range get though. Most of the size-sorted material was used for the EXAFS samples but a few devices were also made with the smallest particles; they have a very low light output ($\ll 1\%$), suggesting that there is a size limit below which the individual particles do not luminesce well. We therefore conclude that in the devices made with heavily ground but not size-sorted samples, the light emission was likely dominated by the few remaining large particles.

X-ray absorption data were collected at a temperature of 6K using a liquid helium cryostat, on beamline 10-2 at the Stanford Synchrotron Radiation Lightsource (SSRL). The data were collected in transmission mode for the host Zn K-edge and in fluorescence mode using a 13-element Ge detector for the dopant (Cu and Mn) K-edges. For the Cu K-edge in these low concentration samples ($\sim 0.15\%$ Cu), it is very important to eliminate harmonics that would excite the Zn K-edge, as the host Zn fluorescence can

interfere with the very weak Cu fluorescence. This was achieved using a double Si 111 monochromator (which has no second harmonic) and detuning the monochromator 50% to reduce the higher harmonics. A slit height of 0.7 mm resulted in an energy resolution of $\sim$ 1.6 eV. The data were reduced and the k-space files Fourier Transformed (FT) to r-space using the RSXAP package.[Booth, 2012]

The Cu K-edge EXAFS data presented in Figure 4.10 show a large peak amplitude reduction as the host particle size decreases. We focus on the first peak which corresponds to Cu-S bonds. Since for a Gaussian pair distribution function (PDF) the amplitude is proportional to $1/\sigma$ where σ is the width of the PDF, the decreased amplitude immediately shows an increase of σ for the Cu-S bonds. In contrast, for Zn and Mn K-edge data (shown in the two insets of Figure 4.10), there is no significant change in the amplitudes of any peak, and thus no significant change in σ for the Zn-S or Mn-S bonds. Further, the shoulder on the first peak at $\sim$ 2.4 Å for the Cu EXAFS, decreases dramatically as the particle size decreases. This shoulder is a signature for the CuS structure[Warkentin *et al.*, 2007] and corresponds to a short Cu1-Cu2 peak; its disappearance indicates that most of the CuS structure is damaged for the smallest ZnS:Cu,Cl particles. This is a very unusual situation because the CuS nano-precipitates (which dominate the EXAFS here because they contains $\sim$ 75% of the Cu) are tiny *internal* structures along [111] planes in the ZnS host. It should also be recognized that in ground particles of most materials, the distortions from grinding are confined to a thin surface layer that is usually a negligible fraction of the sample at micron sizes and not observable in EXAFS; surface distortions only become important at the nanoparticle

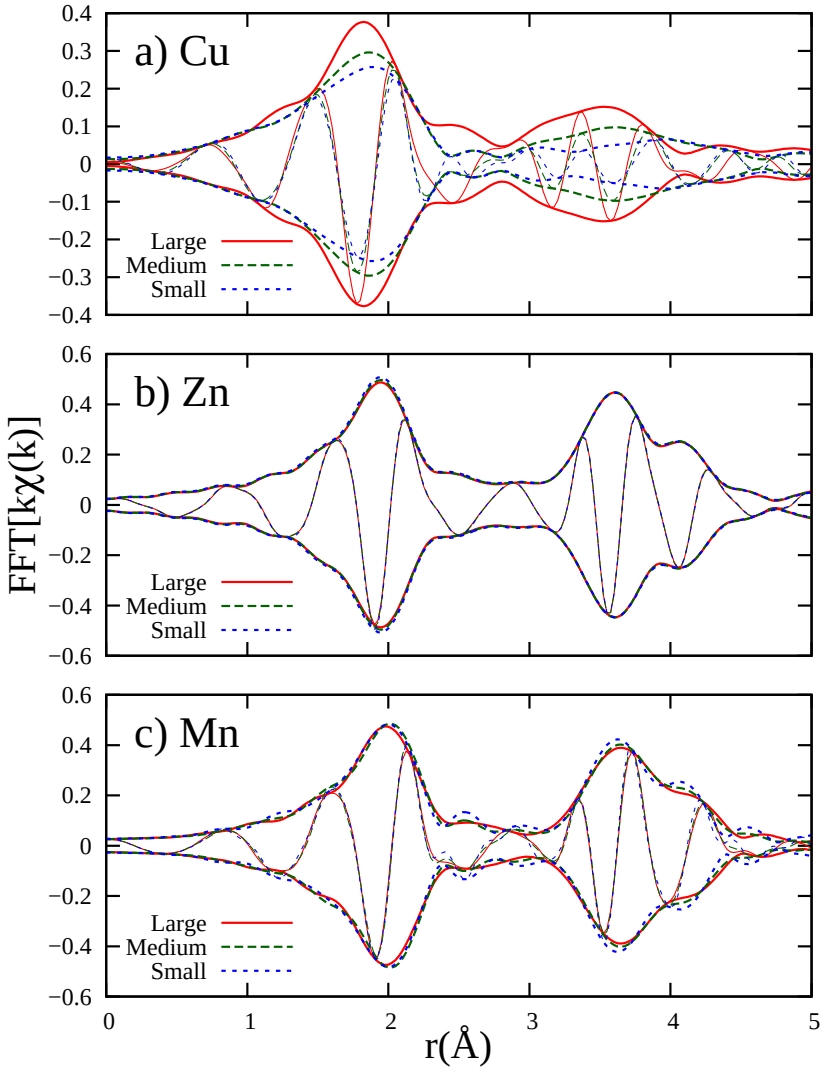

Figure 4.10: a) The r-space Cu K-edge EXAFS plots for the three sizes, showing a large peak amplitude decrease for the smaller particles. b) and c) show the corresponding results for the Zn host and substitutional Mn (5%) show no change with particle size. Cu and Zn plots for ZnS:Cu,Cl; Mn plot for ZnS:Cu,Mn,Cl. In these (and following) r-space graphs, the rapidly oscillating function is the real part, R, of the FT while the envelope function is $\pm\sqrt{R^2+I^2}$ where I is the imaginary part of the FT. Fourier Transform ranges: Cu 3.5–11.3 Å; Zn 4.0–13.5 Å; Mn 3.5–13.2 Å.

level.[Gilbert *et al.*, 2004]

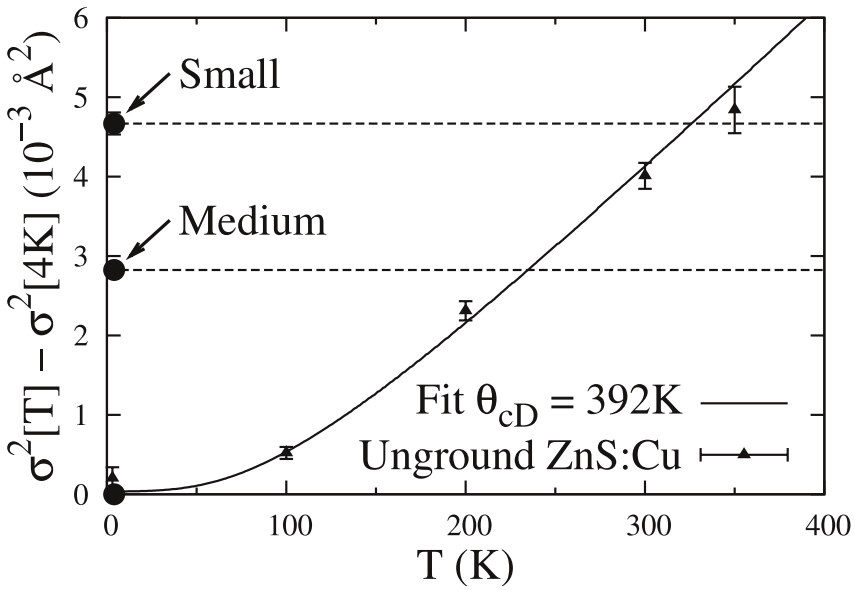

Figure 4.11: A comparison of σ^2 for Cu-S in different size ground particles at 10 K with previous Cu EXAFS results[Stanley *et al.*, 2010] for unground ZnS:Cu,Cl over a range of T.

To quantify the extent of the distortions for the Cu-S PDF, we fit the first peak of the data two ways: using a theoretical Cu-S standard (FEFF[Ankudinov *et al.*, 1998b]) and using the 4 K data for unground ZnS:Cu,Cl as an experimental standard. The fit range was 1.2–2.1 Å. For each fit only r and σ were allowed to vary and the parameters E_o and S_o^2 were fixed; for the experimental standard, $E_o = 0$ and $S_o^2 = 1$, while for the theoretical standard we fixed these parameters to those used in previous fits:[Stanley *et al.*, 2010] E_o = –8.5 eV, $S_o^2 = 0.75$. The results from both fits are comparable; the relative increases of σ^2 for the ground samples at 10 K are compared in Figure 4.11 to our previous results for σ^2(T) for Cu in unground ZnS:Cu,Cl. For the $\sim$

2 μm particles, the grinding-induced static distortion is comparable to phonon disorder above 300 K.

A further indication of the very large disorder about the Cu atoms is that the shape of the Cu-S peak (in Figure 4.10) becomes quite asymmetric for the smallest particles and the quality of fit parameter C^2 ($\propto$ to χ^2) worsens rapidly as size decreases—for large particles, $C^2 = 13.0$; for medium, $C^2 = 64.9$; and for small, $C^2 = 108.7$; a factor of 8.4 increase compared to the large particles. In contrast, for thermally induced disorder in unground material, the shape of the Cu-S peak changes little and the increase of C^2 from 4 K to 300 K is only a factor 2. This large increase of C^2 for the smallest ground samples indicates that describing the grinding-induced disorder by an increased width of either a simple Gaussian or Gaussian broadening the low T data of unground material, is a poor approximation—the grinding-induced disorder is more complex, perhaps a split peak. The fact that the Cu K-edge shows such large effects while the Mn K-edge shows no significant change, means the cleavage of the ZnS particles during grinding is not a random process.

4.3.4 Near Edge Structure

The XANES for the Cu K-edge provides yet another probe of the local structure around Cu atoms. In general, for very tiny clusters—one or two shells of neighbors—the absorption edge is quite smooth with little structure. Structure in the edge (when it exists) arises from multiple-scattering of the ejected photoelectron within a large cluster of order 6–9 Å in radius around the excited atom.

In Figure 4.12, we show the XANES at each absorption edge for three particle sizes. For the host Zn (b) or the dopant Mn (c) XANES there is no significant change in the edge shape which is consistent with the results from the EXAFS analysis, that there is little damage about Zn atoms in the host lattice or about substitutional Mn atoms. In contrast, the Cu K-edge XANES (Figure 4.12(a)) show a large decrease in the edge structure as the particle size decreases, providing further support for preferential damage about the Cu atoms located mainly in the CuS precipitates. These nano-precipitates were initially embedded inside the ZnS host crystallites, and therefore most of them should have remained intact if the grinding process were random. Unfortunately this must remain a qualitative argument as the potentials for sulphides, needed to simulate the Cu K-edge XANES, are not yet good enough[Rehr, 2009] for a quantitative comparison.

4.3.5 Discussion

Both the EXAFS and the XANES indicate a significant structural change about the Cu atom within the CuS precipitates when the ZnS:Cu,Cl or ZnS:Cu,Mn,Cl phosphor particles are ground to make fine particles, yet no corresponding change is observed for the Zn host material or the Mn dopant in ZnS:Cu,Mn,Cl. Note that the changes in the Cu K-edge data are nearly the same in both ZnS:Cu,Cl and ZnS:Cu,Mn,Cl (not shown). This means that the CuS precipitates, initially embedded inside the ZnS:Cu,Cl particles, are preferentially damaged while the ZnS material surrounding them is not—a very unusual situation. The only way that the CuS nano-precipitates

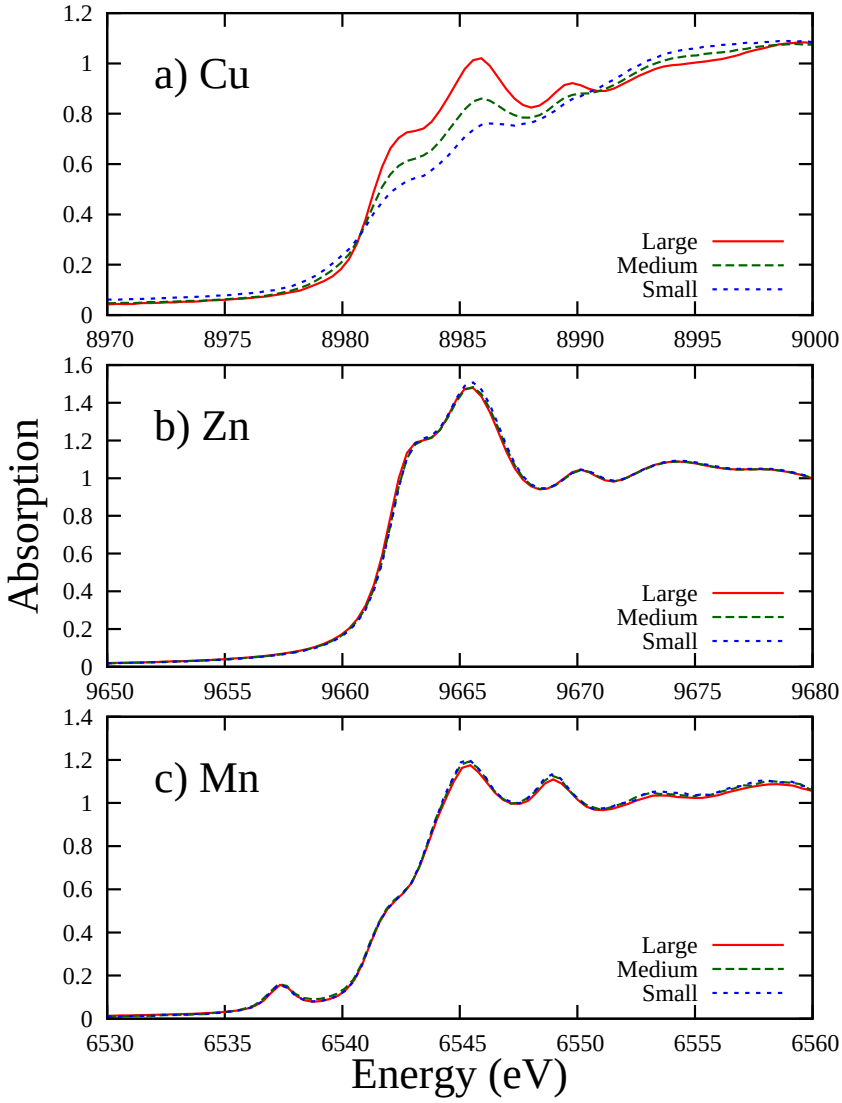

Figure 4.12: XANES data at the Cu, Zn, and Mn edges as a function of particle size. The Cu XANES data (a) show a significant loss of structure with decreasing particle size; in striking contrast, no change occurs for either the (b) Zn or (c) Mn XANES.

can be significantly damaged without noticeable damage to the ZnS host in the grinding process are: 1) the ZnS particles cleave along [111] planes containing the CuS precipitates, thereby fracturing the tiny CuS nano-precipitates or 2) the ZnS particles crack or are badly strained along these planes. Note that an 18.4 Å thick layer of CuS (one unit cell c axis parameter plus one S-S double bond) can replace a region of ZnS in a [111] plane that is 18.7 Å thick (twice the cube diagonal of the cubic unit cell) as shown in Figure 4.13, producing a small strain of 1.6% between the two materials. More importantly, along the interface-layer the strain is even smaller; the S-S distance in the ab plane for CuS is 3.80 Å while the S-S distance in the [111] plane for ZnS is 3.825 Å, a strain of only 0.66%. This small strain will allow epitaxial growth between the two crystal structures. From our earlier EXAFS studies[Warkentin *et al.*, 2007] we had suggested that the CuS precipitates are likely epitaxially bonded to the ZnS host; Figure 4.13 thus provides a reasonable explanation for this observation. In addition, recent results show that etching occurs preferentially through the [111] planes in ZnS:Cu,[Withnall *et al.*, 2009] suggesting that the ZnS [111] planes are indeed weakened by the presence of the CuS nano-precipitates.

We suggest that fracturing through the CuS nano-precipitates is more likely because the CuS would then be left in the surface layer on the outside of the ZnS particles where it would rapidly become more disordered by further grinding. Note that CuS is a layered structure with S-S double bonds that may break easily under strain. In addition, the fact that the AC EL nearly disappears when we damage primarily the CuS nano-precipitates strongly reconfirms the idea that the CuS nano-precipitates are

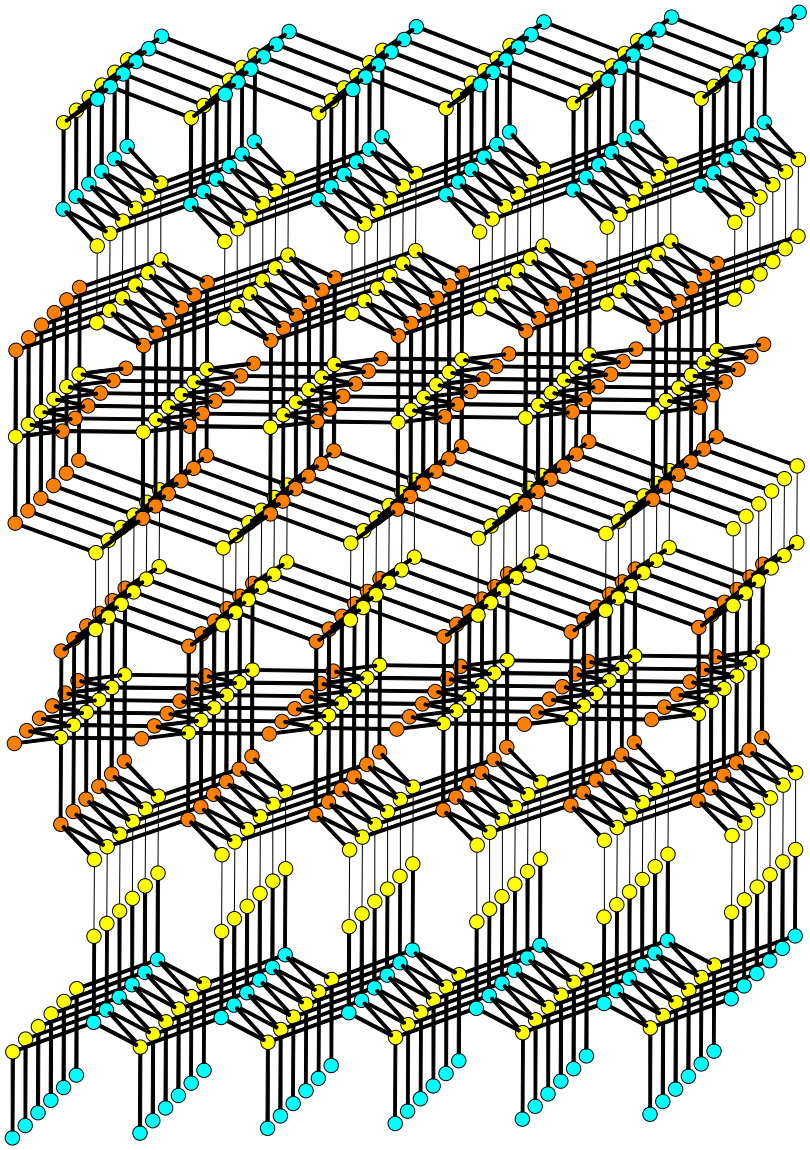

Figure 4.13: The CuS nano-precipitate fits into the [111] planes of the ZnS host with 1.6% tensile strain; the vertical height of the CuS slice is 18.4 Å instead of 18.7 Å for the ZnS structure. The vertical axis is the cubic [111] direction for ZnS.

crucial for relatively low voltage AC EL. However, we must note one caveat: because the PL also decreases qualitatively for ground samples the Cu emission centers might also be damaged. One possible explanation is as follows. The samples are prepared by quenching the phosphors from high temperatures. As the cubic phase develops, the Cu precipitates develop along [111] planes—but there then might be a cloud of Cu centers close to the precipitates that become frozen in place as the sample rapidly cools, *i.e.* the distribution of Cu defects may not be uniform but are more concentrated close to some [111] planes. In that case, cleaving along such [111] planes that contain the CuS precipitates may also damage the Cu emission centers or place them at the surface where non-radiative processes may quench the light emission. Further work is necessary to determine whether or not the Cu defect distribution is uniform at the nanoscale.

Despite the size limitation of micro milling, the enhancement of light output at lower voltages for the 25 μm thick devices compared to the standard 50 μm thick device is interesting due to the significant number of applications that utilize AC EL phosphors for illumination in the mcd/cm^2 range, including back lighting for passive LCDs. To produce 1 mcd/cm^2 with the thinner devices in this study utilizing lightly mill-ground phosphors require 15% less voltage, increasing the attractiveness in low intensity applications where the requirements for higher applied voltages if often a significant hindrance. To produce ZnS:Cu,Cl AC EL devices that utilize the field enhancement from CuS precipitates thinner than 10 μm, a fabrication approach from colloidal nanoparticles[Manam *et al.*, 2010] will probably be more successful due to the damage caused by grinding.

4.4 Core-Shell Nanocrystals

4.4.1 Background

Colloidal semiconductor nanocrystals (NCs)—also referred to as nanoparticles (NPs) or quantum dots (QDs)—are of great interest and have been widely investigated due to their unique size and composition dependent properties.[Nirmal *et al.*, 1996; Chan and Nie, 1998; Zhang, 2000; Peng, 2003; Klimov *et al.*, 2007] Doped NCs are an especially promising and important subgroup of nanomaterials because just a small percentage of an impurity or dopant is introduced to semiconductor NCs to alter their electronic, magnetic, or optical properties.[Erwin *et al.*, 2005; Smith *et al.*, 2000; Yang *et al.*, 2003; Bhargava *et al.*, 1994; Chamarro *et al.*, 1996; Pradhan and Battaglia, 2007; Chen *et al.*, 2004]

In a previous study, photoluminescent ZnS:Cu NCs were synthesized via facile aqueous chemical precipitation method.[Corrado *et al.*, 2009] Through subsequent EXAFS studies, it appeared that the Cu dopants were either on or near the surface of the NCs. In a related study, ZnSe:Mn NCs have been found to be luminescent in core sites while non-luminescent in surface sites, suggesting that it is important to encapsulate the dopant ions into the core site.[Norman *et al.*, 2003]

Thus, one possible strategy is to grow NCs with an undoped ZnS shell around doped ZnS:Cu cores, as shown in Figure 4.14. This strategy has been demonstrated to increase PL intensity with ZnS:Mn.[Cao *et al.*, 2002; Quan *et al.*, 2007; Zheng *et al.*, 2009] Since MnS has the same cubic crystal structure and similar a-spacing as ZnS, 5.22

Å compared to 5.41 Å, respectively, the synthesis of ZnS:Mn/ZnS core-shell structure is relatively easy. On the other hand, CuS, the main precipitate in Cu-doped bulk ZnS, has a significantly different crystal structure than ZnS, and therefore Cu does not fit easily into the ZnS lattice.[Warkentin *et al.*, 2007] For Cu concentrations above ∼ 400–500 ppm, CuS-like precipitates form.[Nickerson *et al.*, 1963; Aven and Parodi, 1960; Nien and Chen, 2006] Consequently, studies of Cu-doping are more challenging and for this reason, ZnS:Cu has not been investigated as widely as ZnS:Mn. The location of the Cu^{-} dopant, particularly whether it is at or near the surface versus in the core of the NCs, is not understood.

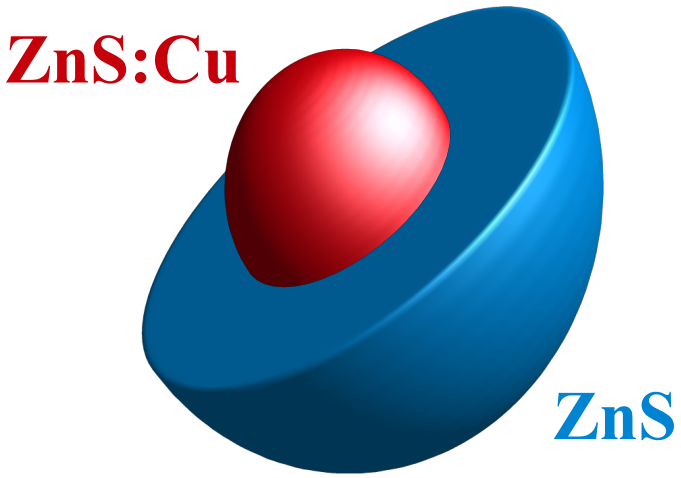

Figure 4.14: Diagram of ZnS:Cu/ZnS core/shell nanocrystals.

In this study, the effect of growing a thin ZnS shell around core ZnS:Cu NCs was investigated with the objective of enhancing the PL of the Cu dopant. The shell growth was monitored using UV-Vis and PL spectrophotometry, and EXAFS. For the

first time, it is shown that the Cu-dopant emission is substantially enhanced by ZnS shell growth around the core Cu-doped ZnS NCs. Detailed analysis of the ZnS trap state PL emission versus Cu PL emission through deconvolution of the observed PL spectra indicates that the thin ZnS capping layer affects the relative PL intensities of the two bands but not their peak positions. The overall enhanced PL of the ZnS:Cu NCs with growth of a ZnS capping layer clearly indicates that, similar to the Mn-dopant in ZnS:Mn NCs, the Cu-dopant is non-fluorescent at surface sites of the ZnS NCs but become fluorescent when confined to the core of the NCs with appropriate capping by a thin layer of ZnS. This study demonstrates a simple strategy for improving the optical properties of doped semiconductor NCs by manipulating the surface.

4.4.2 Experimental Details

In a typical synthesis, ZnS:Cu (0.2%) NCs were synthesized according to our previous work.[Corrado *et al.*, 2009, 2010] The synthesis was slightly modified in that the reaction mixture was brought to reflux, excess Zn was added, and then it was refluxed for 5 minutes rather than 2 hours. The crude reaction mixture was used without purification; however it was allowed to cool to allow for ease of handling, and then 25 mL were extracted and brought back to reflux. 0.15 M $Zn(NO_3)_2$ and 0.1 M Na_2S/0.04 M MPA/0.08 M NaOH were added to the solution in 200 μL injections with a 30 seconds interval in between each injection. Five injections of Zn and S were considered to be a one monolayer addition. The assumption that this constitutes one monolayer is based on a calculation using the size of NCs and their concentration in solution to find the

total surface area of the NCs and then using that to find the amount of Zn and S that would constitute a single monolayer. The shape of the NCs is generally not a perfect sphere, and thus the ZnS shell cannot be assumed to coat the NCs evenly to make up a perfect monolayer. This term, monolayer, is used only to quantify the amount of Zn and S that are added in comparison to the NCs in solution. Each experiment lasted 50 min, which allowed up to 10 monolayers to be grown onto the NCs. Aliquots were taken from the reaction mixture every two monolayers for spectroscopic analysis.

Low-resolution TEM measurements were performed on a JEOL model JEM-1200EX microscope. The crystal structure of the samples was characterized by X-ray diffraction (XRD, Rigaku Americas Miniflex Plus powder diffractometer), using Cu-Ka (λ = 1.54056 Å) irradiation. Diffraction patterns were recorded from 20° to 80° 2θ, with a step size of 0.04° at a rate of 2° per minute. The UV-Vis absorption spectra were taken on a Hewlett Packard 8452A Diode Array Spectrophotometer at room temperature. The photoluminescence (PL) spectra were measured on a Perkin Elmer Luminescence Spectrometer LS50B at room temperature. The samples that were analyzed with spectrophotometry were prepared by dispersing the nanoparticles in Milli-Q water, basified to pH $\sim$ 11 with NaOH, to yield a clear solution. Centrifugation was performed on a Sorvall Legend RT at 3000 rpm for 10 minutes at room temperature.

Temperature dependent EXAFS data at the Cu (fluorescence) and Zn (transmission) K-edge for the powdered ZnS:Cu NC samples were collected at the Stanford Synchrotron Radiation Laboratory (SSRL), beamline 10-2. The NCs were collected using filter paper and then encapsulated and sealed in tape. 1–3 layers were used to

achieve a reasonable absorption step at the Zn K-edge in transmission mode, yielding step heights of about 0.1–0.5. Data were collected using a silicon [111] double monochromator, detuned 50% to reduce harmonics. Small slits ($\sim$ 0.5 mm) provided an energy resolution of 1.3 eV. Cu EXAFS data were collected in fluorescence mode using a 13-element Ge fluorescence detector. Both data sets were reduced using standard procedures (RSXAP)[Booth, 2012] with a Fourier transform (FT) window of 3.0–10.5 Å^{-1} for Cu and 3.0–14.0 Å^{-1} for Zn; the ends of the windows have a Gaussian rounding of 0.3 Å^{-1}. The FT data show peaks in r-space that correspond to shells of neighbors at different distances from the excited atom (Zn or Cu). Note that the peak positions in all EXAFS data are slightly shifted to lower r (by known amounts) compared to the actual bond length.

4.4.3 Characterization

A representative TEM image of the ZnS:Cu NCs before ZnS shell growth is shown in Figure 4.15. The average particle size is 3.6 nm with a size distribution of 9%. The cubic zinc blende structure was confirmed with the X-ray diffraction pattern shown in Figure 4.16, which revealed the (111), (220), and (311) indices, respectively.

The UV-Vis absorption spectra of the ZnS:Cu (0.2%) NCs before shell growth and with ZnS monolayers are shown in Figure 4.17. The 0 monolayer sample has absorption starting around 330 nm and features a small peak around 300 nm and an apparent strong peak around 240 nm. The peak near 240 nm is an artifact due to the decrease in instrumental response since the real absorption is usually expected to

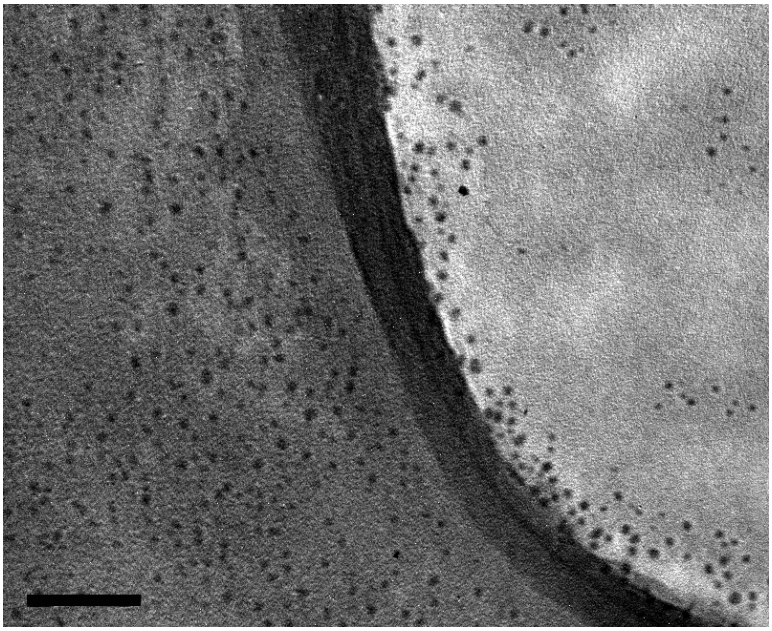

Figure 4.15: Transmission electron microscopy (TEM) image of ZnS:Cu (0.2%) NCs. The scale bar is 50 nm.

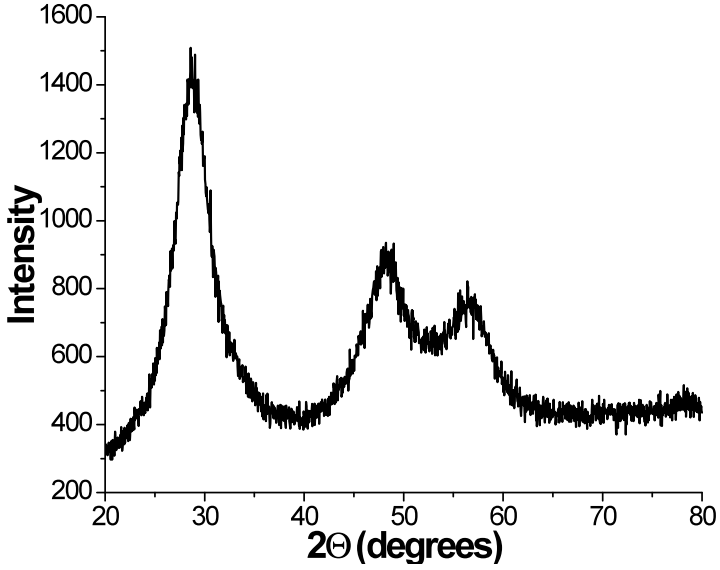

Figure 4.16: X-ray diffraction (XRD) pattern of ZnS:Cu (0.2%) NCs.

continue to increase towards shorter wavelength. As monolayers are added to the surface of the Cu-doped ZnS NCs, roughly from 2–10 monolayers, the absorption onset and peak at 300 nm are red-shifted, as shown in the inset of Figure 4.17. The doping level of Cu did not affect the UV-Vis spectra in any noticeable manner. Overall, there is a small but clear red-shift in the absorption onset due to the increased size of the NCs.

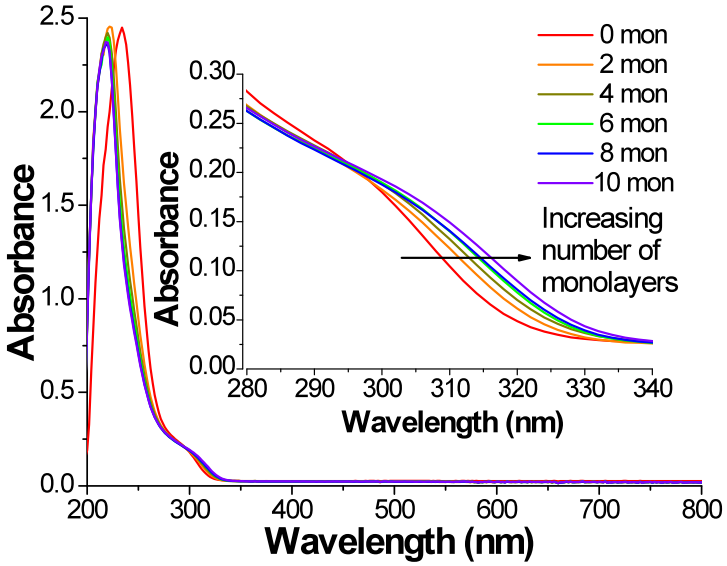

Figure 4.17: UV-visible absorption spectra of ZnS:Cu (0.2%) with 0–10 monolayers of a ZnS shell, grown at 100 °C. The inset shows a closer look of the absorption edge of the same spectra.

For PL measurements, the NC concentration of each sample was adjusted to be 0.26 in optical density (OD) at 280 nm to make it easier for quantitative comparison. The normalized PL emission spectra of ZnS NCs with 0 monolayer coverage doped with 0%, 0.2%, 0.5%, and 1% Cu are shown in Figure 4.18. The undoped ZnS NCs exhibit a peak at 2.79 eV (445 nm) with a FWHM of $\sim$ 0.5 eV. The PL emission peak of the

0.2% Cu is slightly red-shifted and exhibits a peak at 2.76 eV (449 nm). The 0.5% Cu NCs peaked at 2.72 (456 nm) and 1% Cu-doped NCs peaked at 2.62 eV (473 nm). There is an apparent emergence of a peak in each spectra starting $\sim$ 2.3 eV, which is an artifact resulting from the Rayleigh scattering of the excitation light (λ_{ex} = 280 nm) with the grating at second order. There is clearly a red-shift in the observed PL emission peak with increased concentration of copper, similar to what we have observed previously.[Corrado *et al.*, 2009]

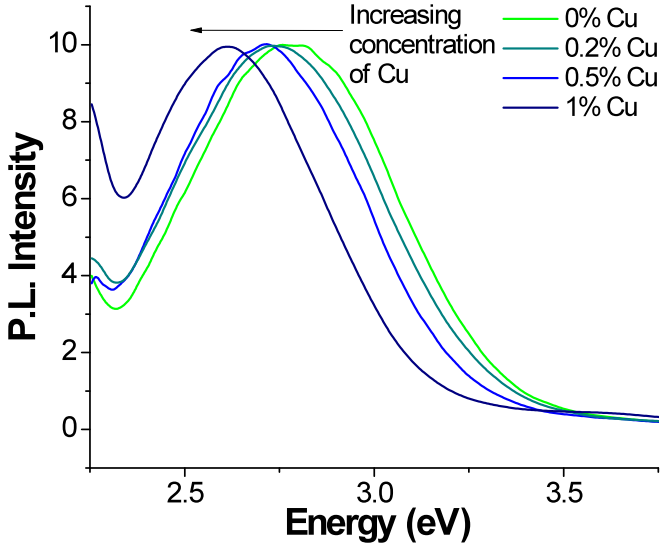

Figure 4.18: PL emission spectra of core ZnS NCs doped with 0%, 0.2%, 0.5%, and 1% copper with λ_{ex} = 280 nm; the NC concentration in solution was adjusted so that the optical OD was 0.26 for each sample.

Based on our previous study,[Corrado *et al.*, 2009] we know that the PL for the Cu-doped ZnS NCs is composed of emission from trap states of ZnS and emission from the Cu-dopant, with their relative contribution dependent on the Cu doping level.

Higher percentages of Cu doping generally led to stronger Cu emission and weaker ZnS emission. In order to better understand the characteristics of these two emissions, the PL of ZnS NCs without Cu doping was also studied. The PL emission spectrum of the undoped ZnS NCs with 0 monolayers is shown in Figure 4.19. The PL spectrum is dominated by one major peak positioned at 2.79 eV with a FWHM of $\sim$ 0.5 eV, which is due to trap state emission based on the large Stokes shift from the bandgap energy. As monolayers of ZnS were added onto the surface of the ZnS NCs at 100 °C, aliquots were taken every two monolayers and their PL spectra show a small but noticeable red-shift towards lower energy. A representative PL spectrum for the 8 monolayer sample is also shown in Figure 4.19, which is red-shifted by about 0.06 eV compared to that with no coverage (0 monolayers). Both PL spectra were fit using single Gaussian functions, as shown in Figure 4.19. Details of the fitting are discussed later. Note that the PL intensity generally increases with an increasing number of monolayers. For example, the increase is about 10% for the 8 monolayer coverage compared to 0 monolayers for the undoped sample.

In order to better understand the relative contributions of ZnS trap state emission and Cu dopant emission as well as their respective characteristics with different monolayer coverages, several samples were compared. As shown in Figure 4.20a, the PL spectrum for the 0.2% Cu sample with 0 monolayers (no coverage) shows a band peaked at 2.76 eV with a FWHM of $\sim$ 0.5 eV. As monolayers were added, the PL emission peak red-shifted and the intensity increased. For 10 monolayer coverage, the PL band peaked at 2.67 eV and displayed an increase in emission intensity of 37% compared to no

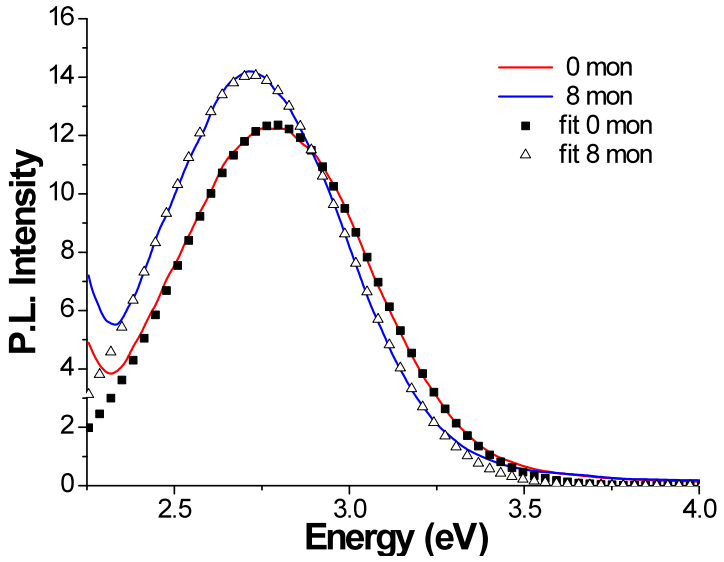

Figure 4.19: The PL emission spectra of undoped ZnS with 0 and 8 monolayers of ZnS and the corresponding single Gaussian fits.

coverage. Each spectrum with zero through 10 monolayers was fit using two Gaussian functions: one to represent the PL from trap states of ZnS and the second to represent the PL from the Cu-dopant. Parameters for the Gaussian representing the ZnS emission peak position and FWHM are kept the same as those used in Figure 4.19. The peak position was allowed to vary between 2.79 eV to 2.72 eV, which were the peak positions for the ZnS emission peak for the undoped sample with zero and ten monolayers. The intensity was then allowed to vary to optimize fitting to the experimental results. The parameters for the Gaussian representing the Cu emission were found by fitting the ZnS:Cu (1%) since its emission is dominated by the Cu emission line. The details of all the fittings will be described in greater detail below. As representative examples for the 0.2% Cu sample, the 0, 2, and 10 monolayer fits are shown in Figure 4.20b with

points (squares, triangles, and stars); the two constituent peaks correlating with ZnS trap-state emission and Cu-dopant emission are shown as solid green and blue lines.

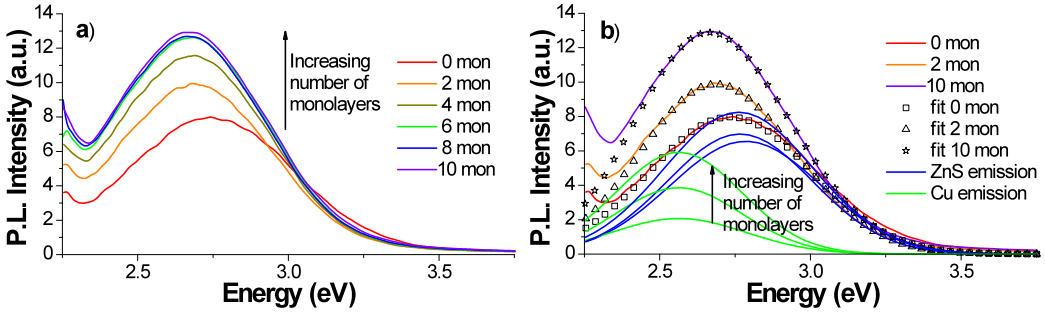

Figure 4.20: (a) PL emission spectra of ZnS:Cu (0.2%) with 0 (red), 2 (orange), 4 (gold), 6 (green), 8 (blue), and 10 (violet) ZnS monolayers with $\lambda_{ex} = 280$ nm; (b) PL emission of ZnS:Cu (0.2%) with 0, 2, and 10 ZnS monolayers with corresponding two-Gaussian fits. The two constituent Gaussians of each fit are shown (the Cu peak is green and the ZnS peak is blue). The peaks increase in intensity with additional monolayers.

Next, we investigated the effect of adding monolayers of ZnS to higher concentration Cu-doped NCs. The PL emission spectra of ZnS:Cu (1%) with 0–10 monolayers are shown in Figure 4.21a. The zero monolayer NCs PL emission spectrum peaked at 2.62 eV and had a FWHM of $\sim$ 0.5 eV. With addition of ZnS monolayers to cover the surface of the doped NCs, the PL emission was very slightly red-shifted. The 10 monolayer coverage sample peaked at 2.61 eV, displaying a shift of only 0.01 eV. The PL emission intensity increased by 57% compared to that of the no coverage sample. Again two Gaussians (at the same positions and with the same widths) were used to fit each PL emission spectra. The 0, 2, and 10 monolayer fits and constituent Gaussians are shown in Figure 4.21b.

For the undoped NCs, one Gaussian function was used while for each of the

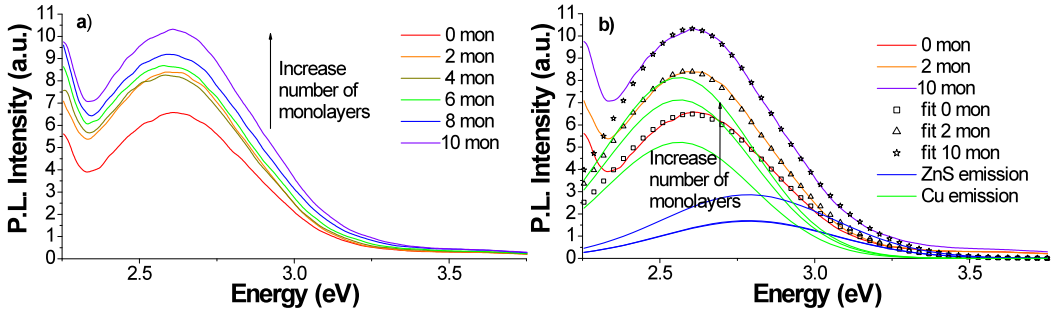

Figure 4.21: (a) PL emission spectra of ZnS:Cu (1%) with 0 (red), 2 (orange), 4 (gold), 6 (green), 8 (blue), and 10 (violet) ZnS monolayers with $\lambda_{ex} = 280$ nm; (b) PL emission of ZnS:Cu (0.2%) with 0, 2, and 10 ZnS monolayers with corresponding two-Gaussian fits. The two constituent Gaussians of each fit are shown (the Cu peak is green and the ZnS peak is blue). Again, the peaks increase in intensity with additional monolayers.

ZnS:Cu NCs two Gaussians were used, one representing the ZnS trap state PL and another representing the Cu-dopant PL. This helps to better understand the dependence of the PL on Cu doping level and on the ZnS shell grown around the core doped NCs. In order to find the peak position of ZnS emission, a single Gaussian fit was used for the ZnS with no Cu, as shown in Figure 4.19. The 0 monolayer sample had a PL band with a FWHM of $\sim$ 0.5 eV and peak position at 2.78 eV. The peak red-shifted with addition of monolayers to 2.72 eV for 8 monolayers of coverage (Figure 4.19). The FWHM remains about the same.

Once the parameters for the Gaussian representing the ZnS PL were determined, the ZnS:Cu (1%) PL spectra were used to determine the Gaussian representing the Cu dopant PL. The 1% sample was chosen since the Cu PL was more dominant and the fitting would generate more accurate numbers for the parameters of the Gaussian representing the Cu PL band. The experimental results and fits with two Gaussians for

the 1% sample are shown in Figure 4.21b. Six data sets (0, 2, 4, 6, 8, 10 monolayers) were fit simultaneously with the location of the ZnS peak allowed to vary slightly between 2.72 eV to 2.78 eV, which was the range found from the undoped ZnS PL emission spectra. For the best fit of the six data sets, the peak for the Cu PL was found to be 2.56 eV (484 nm). The FWHM was found to be $\sim$ 0.4 eV. For clarity, only three of these fits, including the two constituent peaks and the overall fit, are included in Figure 4.21b.

Once the peak positions and FWHM for both the ZnS and Cu PL bands were determined based on the undoped sample and the 1% doped sample, they were used to fit the ZnS:Cu (0.2%) and ZnS:Cu (0.5%) PL emission spectra. The only adjustable parameters allowed to vary were the relative amplitudes of the two Gaussians representing the relative intensities of the two PL bands. Figure 4.20b shows the PL emission spectra with corresponding two Gaussian fits for the ZnS:Cu (0.2%). In the ZnS:Cu (0.2%) fit, shown in Figure 4.20b, the Cu emission peak intensity was observed to more than double while the ZnS emission peak only slightly increased. For the ZnS:Cu (0.5%) (not shown), the Cu emission intensity was again more than doubled, while the ZnS emission was only marginally increased.[Corrado *et al.*, 2010] Likewise, the ZnS:Cu (1%) sample also shows a greater increase in the Cu emission than that of the ZnS emission. The fitting reveals that with addition of a ZnS shell, the Cu emission increased much more than the ZnS trap state emission.

It is interesting to compare quantitatively the intensity of the PL emission in the ZnS NCs doped with various concentrations of Cu and to observe the effect of

adding ZnS layers. We focus on 0 and 10 monolayers as examples. The undoped ZnS NCs showed the least increase in PL emission intensity with ZnS shell coverage when compared to the Cu-doped NCs. A summary of the increases in PL emission intensity and red-shift with 10 monolayer addition is shown in Table 1. The increase in PL intensity with monolayer growth of ZnS is dominated by the increase in Cu-dopant PL, which is a desired outcome for doped semiconductor NCs for electroluminescence and other photonics applications, as discussed later.

	% Increase	λ (0 mono)	λ (10 mono)
0% Cu	10%	445	456
0.2% Cu	37%	449	464
0.5% Cu	67%	456	464
1% Cu	57%	473	475

Table 4.3: Effect of the addition of ZnS shells around a core of ZnS:Cu, both on PL intensity and wavelength.

One key observation is that for each of the core ZnS NCs, the PL intensity increased with the growth of ZnS shells. To understand the origin of this, it is helpful to examine the intensity increase concurrently with the red-shift in PL emission peak position. The undoped sample had a small red-shift of 11 nm with 10 monolayers of ZnS shell coverage, from 445 nm to 456 nm. This PL red-shift is attributed to the increased size of the NCs with shell growth. When the ZnS NCs were doped with Cu, the PL emission was red-shifted compared to the undoped sample before the ZnS shell was grown (Figure 4.18). An even greater red-shift of the PL was apparent in the ZnS:Cu/ZnS NCs when the shell was grown, compared to the undoped NCs. This can be well modeled as an increase in the emission from a Cu center as the thickness of the

ZnS shell increases. In contrast, the UV-Vis absorption spectra of the NCs from 0 to 10 monolayers (Figure 4.17) are identical for doped and undoped samples, and therefore the size evolution of the undoped and doped NCs are determined to be the same.

The reproducible PL spectral shift of ZnS NCs doped with various concentrations of Cu can be well understood by considering the relative contributions of the ZnS trap state emission versus the Cu dopant emission. Since the increase in PL intensity was much higher and the red-shift with increasing ZnS monolayers was more substantial for the doped samples than the undoped samples, the apparent red-shift is attributed mainly to an increase in Cu PL emission with growth of a ZnS shell. The fit results in Figures 4.20 and 4.21 show that the Cu-dopant PL emission increases much more than the ZnS host PL emission and the Cu PL band is redder than the ZnS PL band. The overall observed PL band red-shifts as the contribution from the Cu PL increases. This also explains why the PL for the 1% Cu sample red-shifted only slightly since the overall PL emission was already dominated by Cu, before the ZnS shell was grown. Further growth of the ZnS shell has little effect on the position of the Cu PL. In contrast, samples with low Cu doping in which the ZnS PL and Cu PL are both important, the growth of a ZnS shell resulted in relatively stronger Cu emission and thus the appearance of a red-shift. The stronger Cu PL that results from ZnS shell coverage is likely due to surface Cu sites that were not emissive originally but become emissive upon incorporation into the ZnS lattice with further ZnS shell growth. Successful fitting of the PL emission spectra of the Cu-doped ZnS NCs with two Gaussians representing the emission from Cu and the emission from ZnS seem to support the above explanation (Figures 4.20b

and 4.21).

4.4.4 EXAFS Results

Examples of the k-space EXAFS results, extracted from the absorption data, are shown in Figure 4.22 for the Cu and Zn K-edges. The data for the dilute Cu dopant (obtained in fluorescence mode) are noisier but still have reasonable S/N (signal-to-noise) out to 12 Å^{-1}, while the k-space data for the Zn K-edge have good S/N out to 14 Å^{-1}.

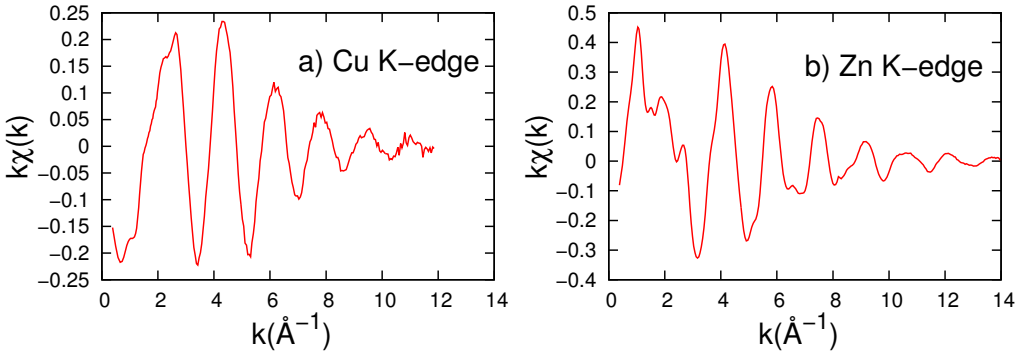

Figure 4.22: k-space data for (a) Cu K-edge and (b) Zn K-edge of ZnS:Cu (0.2%). The energy spectrum is converted into momentum-space (k-space) and then is Fourier transformed to position-space (r-space) to show peaks for different shells of neighbors (see Figure 4.23 and 4.24). Note the different vertical scales; the Cu EXAFS scale is a factor of two smaller than for the Zn EXAFS.

Next the k-space data were Fourier transformed to r-space, which show peaks corresponding to different shells of neighbors about either Zn or Cu. The r-space data at the Zn and Cu K-edges, for NC samples doped with 0.2% and 0.5% Cu, are shown in Figure 4.23 and 4.24, respectively. Each plot is an average of three traces. The data for the initial NCs are plotted with a red line while the data for the NCs, after several

monolayers have been added, are shown in green.

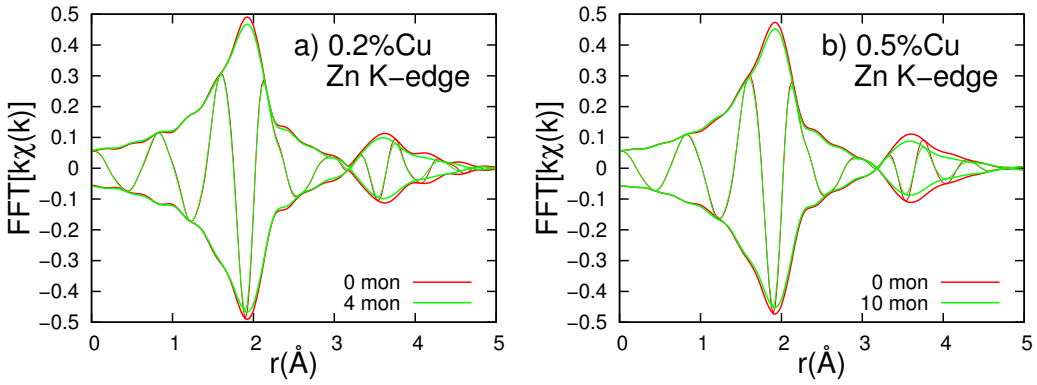

Figure 4.23: Fourier transform of $k\chi(k)$, r-space data, for Zn K-edge. The k-space window is 3.0–14.0 Å^{-1}, with the ends of the window having a Gaussian rounding of 0.3 Å^{-1}. For both Cu concentrations, the additional monolayers cause a slight decrease in both the first and second neighbor peak amplitudes.

The Zn K-edge data (Figure 4.23) show little change in the r-space data as 4 or 10 monolayers are deposited. These r-space plots are nearly identical to Zn K-edge data reported earlier for ZnS nanoparticles.[Corrado *et al.*, 2009] The large amplitude for the Zn-S first peak indicates that the material is reasonably well ordered at the nearest neighbor level, but the small amplitude for the second (Zn-Zn) peak shows that there is considerable disorder at the second neighbor level. For both Cu concentrations, the amplitude is very slightly reduced for both the first (Zn-S) and second (Zn-Zn) peaks, indicating slightly increased disorder of the ZnS host material when monolayers are added. More importantly, the second peak, which corresponds to Zn-Zn pairs, is much smaller than bulk and was expected to grow as the size of the nanoparticles increased, if the nanoparticles had good crystallinity.[Stanley *et al.*, 2010]

The Cu K-edge data (Figure 4.24) also shows little change in the r-space data

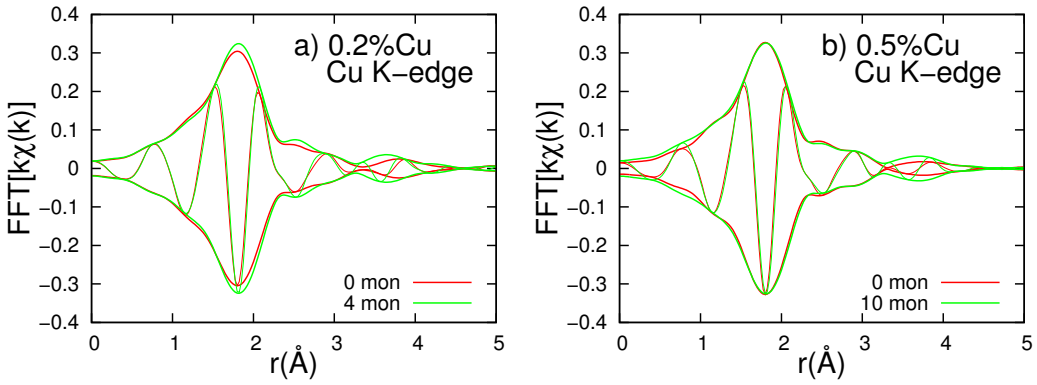

Figure 4.24: Fourier transform of $k\chi(k)$, r-space data, for Cu K-edge. The k-space window is 3.0–10.5 Å^{-1}, with the ends of the window having a Gaussian rounding of 0.3 Å^{-1}. For both Cu concentrations, the additional monolayers cause a very slight increase in the second neighbor peak amplitude.

as 4 or 10 monolayers are deposited. Again the first (Cu-S) peak is large indicating little disorder for the nearest neighbors. However, the second neighbor peak (Cu-Zn) is very small and significantly smaller than the (disordered) Zn-Zn peak in the Zn K-edge data. This low amplitude means there is a high degree of disorder for the Cu-Zn second neighbors, or perhaps a decreased number of Zn neighbors. Unlike the Zn K-edge data, the amplitude of the second (Cu-Zn) peak is marginally increased for all the samples when monolayers are added; *i.e.* the second neighbor distribution becomes slightly more ordered.

4.4.5 Discussion

It is clear from comparing the PL emission spectra and their fits (Figures 4.19–4.21) that there is a greater increase in PL emission intensity with ZnS shell addition for the Cu emission center. The increase in Cu emission may be attributed to the addition

of a ZnS shell covering non-emissive Cu dopant sites that reside on the surface of the initial ZnS:Cu NCs and essentially make them into part of the core of the NCs. These non-emissive sites were proposed based on EXAFS studies of the core doped particles in our previous work[Corrado *et al.*, 2009] in which the large disorder of the second shell around Cu could result from Cu near the surface of the nanoparticle.

We conclude that ZnS:Cu NCs luminescence is predominantly from core dopant sites, similar to the results for ZnSe:Mn NCs.[Norman *et al.*, 2003] In addition, we have demonstrated a simple but effective strategy to increase the dopant PL by using a thin layer of undoped host semiconductor to incorporate the original, non-luminescent surface dopant sites. It was further noted (see Table 4.4.3) that for both the ZnS:Cu (0.2%) and ZnS:Cu (0.5%) NCs, the Cu emission more than doubled upon ZnS shell growth, while the Cu PL peak of the ZnS:Cu (1%) increased by less than expected compared to that of the lower concentration samples, likely due to quenching caused by aggregation of the CuS at too high of dopant concentration, again similar to the Mn-Mn quenching observed for ZnSe:Mn.[Norman *et al.*, 2003]

The EXAFS results show that at the nearest neighbor level, the environments about both Zn (host) and Cu (dopant) are quite well ordered. However for the second neighbors (Zn-Zn or Cu-Zn) there is significant disorder; the Zn-Zn peak is significantly smaller than in bulk ZnS and this reduced amplitude cannot be simply explained by the small size of the NCs (4–6 nm). Furthermore, the disorder is slightly larger when monolayers are deposited (which should normally lead to a larger Zn-Zn peak in good crystalline material). This suggests that the deposited ZnS shell is not of high crys-

tallinity. Thus the NCs are either collections of very tiny nanocrystals ($\sim$ 1 nm) or include significant fractions of amorphous phase, or both.

The disorder about Cu at the second neighbors is even higher, but surprisingly the Cu-Zn is marginally larger when the ZnS monolayers are added. The high disorder at the second neighbor level is not surprising as Cu prefers the layered CuS structure over the cubic ZnS structure—note that the CuS structure does have a similar tetrahedral arrangement of S around one of the Cu sites. The slight increase in amplitude of the Cu-Zn peak is consistent with the result from the photoluminescence experiments, that the copper is becoming more encapsulated by adding ZnS monolayers.

Combined with the PL data, this suggests that the Cu environment is disordered even when far from the surface of the NCs. Given the small particle size and low Cu concentration, we expect only 2–4 Cu atoms per NC, making it very unlikely to form a Cu-S precipitate. Also, the Cu-S bonds are shorter[Warkentin *et al.*, 2007] and might strain the ZnS host crystal locally. Because the ZnS NCs already have significant disorder, and Cu prefers a different local environment to the cubic ZnS structure, the small Cu-Zn peak amplitude likely means that either the Cu dopants may diffuse to more disordered regions of the NCs or the Cu dopant is moving off-center, possibly due to a neighboring S vacancy.

Thus, the result of shell growth was an amplitude increase and a red-shift of the overall PL of the NCs that was significantly more pronounced for the Cu-doped ZnS NCs than the undoped ZnS NCs. When the PL emission from the doped samples was deconvolved into two PL bands representing the ZnS emission and Cu emission, it

became clear that there was a much greater increase in Cu emission than ZnS emission due to ZnS shell growth. This greater increase is attributed to the surface Cu-dopant incorporation into the core ZnS NC lattice aided by the extra ZnS shell. The EXAFS data indicate that, with added monolayers, Cu has marginally more ordered second neighbors, consistent with increased copper encapsulation. However, adding monolayers of ZnS actually appears to decrease the second neighbor (Zn-Zn) peak slightly, indicating that the additional ZnS is more disordered than the core and may have a significant amorphous fraction.

4.5 Dilute Cu Dopants

4.5.1 Background

One major long-standing question about ZnS:Cu phosphors still remains unanswered: what is the local structure of the luminescent emission centers that are associated with the low concentration Cu sites? Several models have been proposed but local structure details are very limited. Because of the low solubility of Cu in ZnS, definitive studies need to be done at very low Cu concentrations where precipitates have not formed. In addition, the evidence for sulfur vacancy (V_S) trap states is also indirect, and there may be isolated V_S as well as complex centers, with V_S associated with some other defect. Here, for the first time, we address the local structure about Cu using EXAFS studies of a number of low concentration NC samples in conjunction with spectroscopic studies. The analysis suggests that a S vacancy exists on one of the

nearest neighbor sites about the Cu dopants.

Early work established, with a few ppm sensitivity, that all the Cu atoms in bulk ZnS:Cu are diamagnetic and hence Cu (including the Cu atoms that form the CuS precipitates) is in the +1 valence state when the material has not been excited—either optically or electrically.[Bowers and Melamed, 1955; Holton *et al.*, 1969] Our NC ZnS:Cu,Cl samples also show no Electron Spin Resonance (ESR) signal at liquid helium temperatures when unexcited, while a signal emerges when excited with UV light as noted earlier for bulk material by Holton.[Holton *et al.*, 1969] For the isolated Cu atoms in the ZnS host (*i.e.* not in CuS precipitates), the +1 valence state requires other nearby defects for charge compensation. Cu^+ has a d^{10} configuration and is not paramagnetic, but when it is excited by trapping a hole, it temporarily has a d^9 configuration and is optically active and paramagnetic.

An important additional property of the center(s) responsible for the blue PL line dominant in our samples is that according to Raman studies of single crystals, at least some of the non-precipitate defects appear to have local C_{3v} symmetry,[Urabe *et al.*, 1968] and hence these Cu atoms are not in a site with the simple tetrahedral symmetry of the zincblende lattice.

A number of charge compensated Cu-complex models have been suggested for these low concentration emission centers. The main models discussed in the literature are: two substitutional Cu^+ atoms on Zn sites, Cu^+_{Zn}, adjacent to a S^{2-} vacancy, substitutional Cu^+_{Zn} plus substitutional Cl^- on a neighboring S^{2-} site, Cl^-_S, and a Cu pair formed of substitutional Cu^+_{Zn} plus a nearby interstitial Cu atom, Cu^+_i.[Shionoya, 1999;

Tanaka *et al.*, 1999; Apple and Prener, 1960; Shionoya *et al.*, 1964; Thornton, 1956; Suzuki and Shionoya, 1971; Blicks *et al.*, 1961; Urabe *et al.*, 1968; Bol *et al.*, 2002] Cu^{+}_{Zn} adjacent to either a S^{2-} vacancy or a Cl^{-}_{S} defect will have C_{3v} symmetry while the most likely Cu_i site (site I_1 with four S nearest neighbors) does not; a second interstitial site (site I_2 with four Zn/Cu nearest neighbors) would have C_{3v} symmetry if one of the four nearest neighbors was Cu. These sites are shown in Figure 16 of the paper by Stanley *et al.* [2010] Additional complexity arises if the S vacancy, Cl^{-}_{S}, or interstitial Cu_i are on more distant sites.

A more important consideration is that the Cu 3d-states split into e_g (lower) and t_{2g} (upper) multiplets in the tetrahedral crystal field of the zincblende lattice. Under C_{3v} reduced symmetry, the t_{2g} multiplet splits further into e'_g and a_{1g}. Consequently, there may be three possible hole trap states for an activated Cu site that could lead to three distinct optical emission lines. Such a variety of possibilities may explain why in ESR experiments, $T \leq 4$ K, as many as seven distinct (meta-stable) ESR signals associated with Cu can be produced by UV activation.[Holton *et al.*, 1969] Because ESR is an extremely sensitive probe and can see defects at the ppm level, some of the centers observed may be extremely dilute. However, because there are only 3 dominant optical emissions in our earlier studies,[Stanley *et al.*, 2010] we focus on these dominant centers.

In this work, we can directly address three questions about the charge compensation from near neighbors: 1) is there a significant fraction of Cu^{+}_{Zn} defects with a charge compensating nearest neighbor S vacancy, leaving only three S neighbors, 2) do

adjacent Cl_S^- defects provide most of the charge compensation, or 3) do a significant fraction of interstitial sites, Cu_i, exist? We have partially addressed the last question in studies of bulk ZnS:Cu particles[Stanley *et al.*, 2010] and some higher concentration Cu-doped ZnS NCs[Corrado *et al.*, 2009]; however because these Cu-doped NCs had concentrations well above the Cu solubility limit, there may have been CuS clusters, limiting our ability to exclude interstitial sites to $\sim 10\%$. To provide a more definitive upper limit on the fraction of Cu in interstitial sites, we use ZnS NCs with very low Cu concentrations, $\sim 0.02\%$ and 0.04% Cu. For these concentrations, and NC diameters below 6 nm, the average number of Cu atoms/particle is < 1; so little or no clustering should be present.

4.5.2 Experimental Details

Five ZnS:Cu,Cl NC samples were synthesized by an aqueous precipitation method, as in the paper by Corrado *et al.* [2009]. Three of the samples have $\sim$0.02% Cu (samples A1, A2, and A3) while the other two contain $\sim$0.04% Cu (samples B1 and B2). Briefly, $Zn(NO_3)_2{\cdot}6H_2O$, $CuCl_2{\cdot}2H_2O$, and mercaptopropionic acid (MPA) were combined in milli-Q water. The pH was adjusted to 11 using NaOH. Next, the solution was degassed after which $Na_2S{\cdot}9H_2O$ was injected quickly. It was stirred for 15 minutes, then exposed to air. The reaction mix was then refluxed 1 hour while excess Zn ($Zn(NO_3)_2{\cdot}6H_2O$) was added. The NCs were precipitated by addition of ethanol, centrifuged, washed several times with ethanol, and finally lyophilized.

The UV-Vis absorption spectra were taken on a HP 8452A diode array spec-

trophotometer at room temperature. The PL spectra were measured on a Perkin-Elmer LS50B luminescence spectrometer at room temperature. The samples that were analyzed with spectrophotometry were prepared by dispersing the NCs in milli-Q water, basified to pH $\sim$ 11 with NaOH, to yield a clear solution.

The EXAFS samples were prepared by dissolving the cleaned NC powder in a few drops of milli-Q water. The concentrated solution was then dropped onto filter paper with the dimensions 3 mm by 13 mm. The filter paper, saturated in NCs, was then sandwiched between two glass slides and warmed on a hotplate to evaporate the water without the edges curling up. Each dried filter paper plus NC sample was then encased in Scotch tape to contain the NCs, several layers of which were stacked together such that the step height at the Zn K-edge absorption was in the range 0.3–1.

EXAFS and XANES data for the ZnS:Cu,Cl NCs (3–6 nm in diameter) were collected at 10 K at the Stanford Synchrotron Radiation Lightsource (SSRL) on beamline 10-2 using a Si [111] double monochromator detuned by 50% to reduce harmonics. A slit height of 0.6 mm provided an energy resolution of $\sim$ 1.5 eV. The Zn K-edge data were collected in transmission mode; the Cu K-edge data were collected in fluorescence mode using a 13 element Ge detector with the samples at 45° to the incident beam. For both types of data sets, a pre-edge subtraction was applied using standard procedures (RSXAP).[Booth, 2012]

Because of the very low Cu concentration, the weak Zn Raman line from ZnS becomes an important background contribution in a Cu scan; this peak is at a fixed energy below the incident X-ray energy[Sánchez *et al.*, 2006] and grows in amplitude

as the incident X-ray energy approaches the Zn K-edge. During a Cu scan, the Zn Raman peak passes through the fluorescence window set up for Cu. In addition, very close to the Zn K-edge at the top of the Cu scan, the tail of the Zn fluorescence peak also produces a background within the Cu fluorescence window. These background contributions were subtracted by conducting a Cu scan on Zn foil, fitting to a 6^{th} order polynomial, and then weighting and subtracting this background function from the low concentration Cu scans.[Medling and Bridges, 2011]

These corrected data were then re-reduced, again using standard procedures (RSXAP)[Booth, 2012], to obtain k-space data, $k\chi(k)$, and then averaged over 5 scans to improve the signal-to-noise for these very dilute samples. Examples of the k-space data are shown in Figure 4.25 for three samples; two with 0.02% Cu (A1 and A2) and one with 0.04% Cu (B2). Scans for the other two samples were similar. Although the scans become noisy at high k, they have nearly identical structure up to $k \sim 11$ Å^{-1} and we use the data up to $k = 10.5$ Å^{-1} to Fast Fourier Transform (FFT) the k-space data to r-space using an FFT window of 3.5–10.5 Å^{-1} with a Gaussian rounding of 0.3 Å^{-1}.

4.5.3 Optical Properties

The PL emission spectra of ZnS:Cu (0.04%) compared to the PL emission of ZnS:Cu (1%) are shown in Figure 4.26, along with the UV-vis spectrum of the 0.04% sample. The UV-Vis absorption spectrum shows an absorption onset around 330 nm and features a small peak around 310 nm and an apparent strong peak around 230 nm.

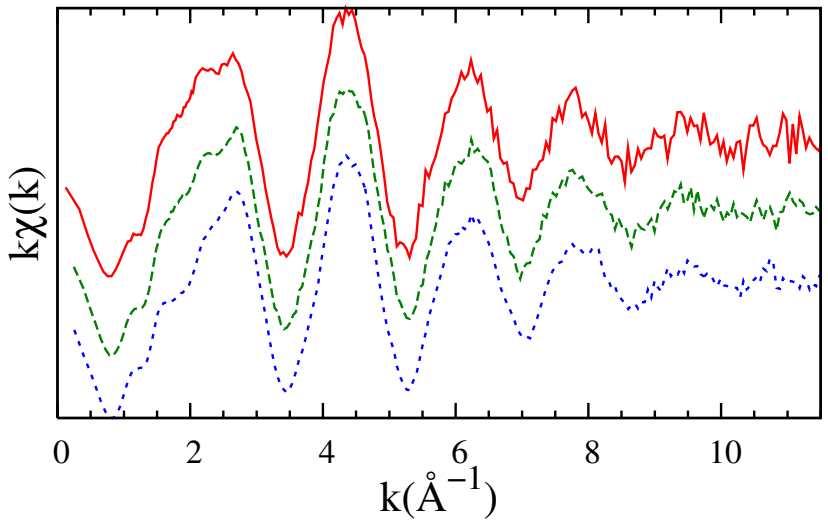

Figure 4.25: Averaged k-space data for three ZnS:Cu samples, top to bottom: A1 – Cu 0.02% (solid red), A2 – Cu 0.02% (dashed green), and B2 – Cu 0.04% (dotted blue).

The peak near 230 nm is likely an artifact due to the unreliable instrument response in that region. The excitonic peak at 310 nm is due to bandgap excitation of the host and is indicative of the small size of the NCs. The UV-Vis spectra of undoped and Cu doped ZnS NCs are indistinguishable, indicating that Cu-doping has no or little effect on the electronic absorption spectrum of ZnS. This is not surprising due to the low doping level.

The PL emission spectrum of the ZnS:Cu (0.04%) shows a broad emission band around 445 nm with a FWHM of 90 nm. The emission from this sample is indistinguishable from that of the undoped ZnS NCs because it contains such a low concentration of Cu. The ZnS:Cu (1%) sample exhibits a red-shifted emission band around 465 nm, which confirms successful Cu doping, as our previous work shows the dependence of the PL emission peak position on the concentration of Cu. [Corrado

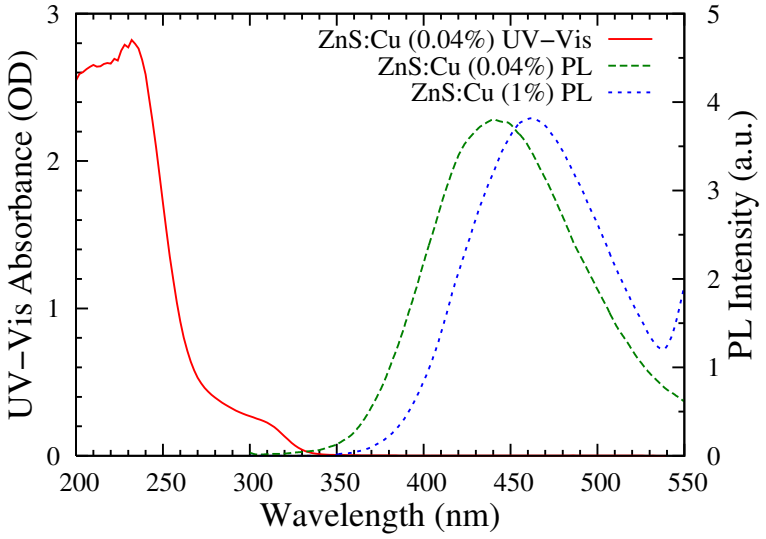

Figure 4.26: UV-Vis and PL spectra of ZnS:Cu (0.04%) (red and green lines) and ZnS:Cu (1%) (blue line).

et al., 2009]

4.5.4 Cu K-edge EXAFS Data

Examples of the averaged r-space Cu K-edge data for two different 0.02% Cu samples (A1 and A2), and a 0.04% Cu sample (B2) [same samples as in Figure 4.25], are shown in Figure 4.27 and compared with the corresponding Zn K-edge data, and a simulation for Zn on the surface, to be discussed later. Note that the EXAFS r-space position is slightly shorter than the actual position; this difference arises from a well known phase shift[Teo, 1986] and is included in the fits. All three Cu traces are nearly identical (as are A3 and B1, not shown), indicating the same local structure in each sample. The first peak near 1.8 Å (actual distance $\sim$ 2.3 Å) corresponds to the nearest neighbor S atoms in cubic ZnS; the next peak for this structure, assuming substitutional

Cu^{+}_{Zn}, corresponds to twelve Zn neighbors and should occur near 3.6 Å (actual distance 3.8 Å). However, there is no obvious peak between 3 and 4 Å for the Cu K-edge data in Figure 4.27a–c. It is very surprising that this peak is so weak since it is present in the Zn K-edge data for the NCs (see Figure 4.27d), and even a Cu site close to the surface would have 4–6 Zn second neighbors and lead to a visible, although reduced, second neighbor peak (see Figure 4.27e).

If there is also some interstitial Cu, there are two possibilities as described above. Site I_1 would again have four S nearest neighbors and the first Cu-S peak in the EXAFS plot would be near 1.8 Å. However, the next peak for this interstitial Cu site would occur near 2.4 Å in the EXAFS plot (actual distance 2.7 Å) and correspond to six Zn neighbors. Since the amplitude near 2.4 Å is very low, there cannot be much interstitial Cu of this type. The second interstitial site, I_2, has four Zn/Cu neighbors at $\sim$ 2.34 Å, the same distance as for Zn-S in ZnS. We address both possibilities below.

4.5.5 Cu K-edge XANES Data

Since XANES is also sensitive to distortion, before doing the EXAFS analysis of the Cu K-edge data (discussed below), we examined the Cu K-edge XANES for these and similar samples at higher Cu concentrations. In Figure 4.28 we plot the edges for several samples and compare them to two reference samples, Cu metal and a Cu_2S bulk powder.

The XANES for the four ZnS:Cu samples are very similar and have little structure—a small amplitude variation at the top of the edge (8990–9010 eV) and tiny

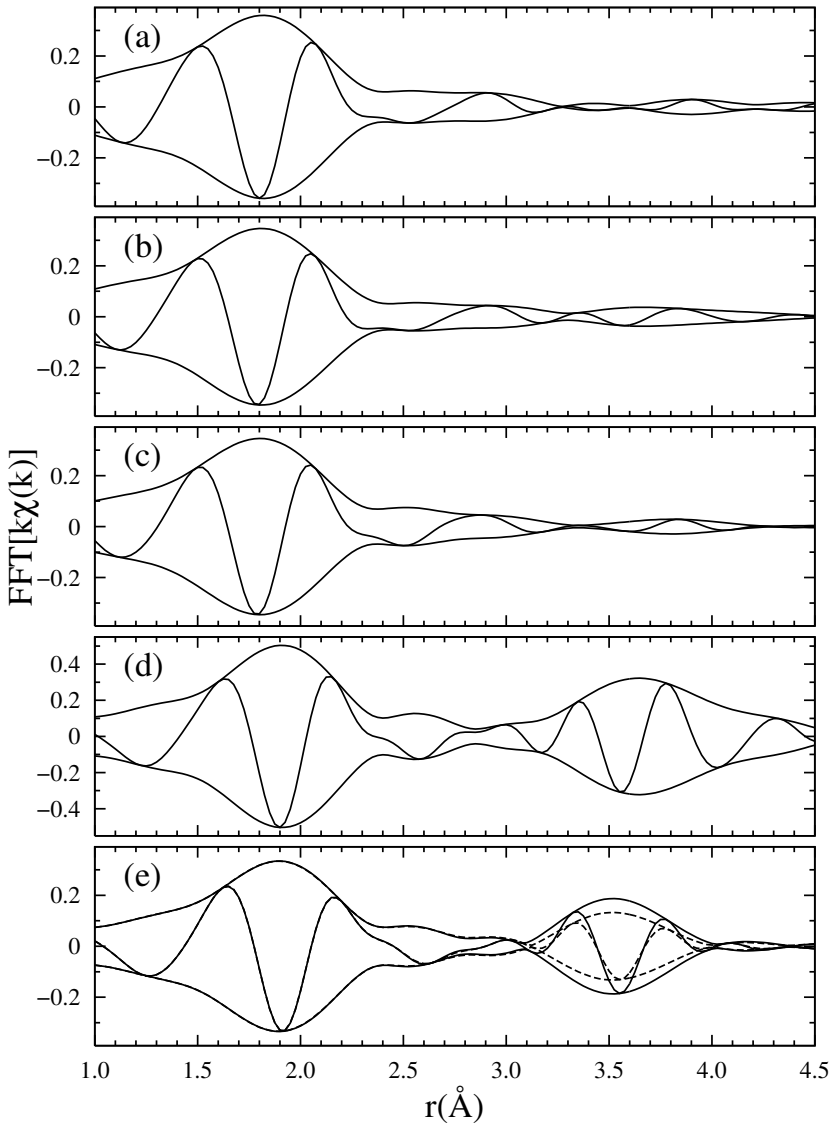

Figure 4.27: r-space data for three ZnS:Cu samples: (a) A1, 0.02% Cu, (b) A2, 0.02% Cu, (c) B2, 0.04% Cu. (d) The corresponding FFT for Zn K-edge data over the same FFT range, and (e) a simulation for Zn on the particle surface, with 3 S neighbors and either 4 (dashed) or 6 (solid) Zn neighbors. A significant global broadening, $\sigma^2 \sim 0.006\text{Å}^2$, was included for (e).

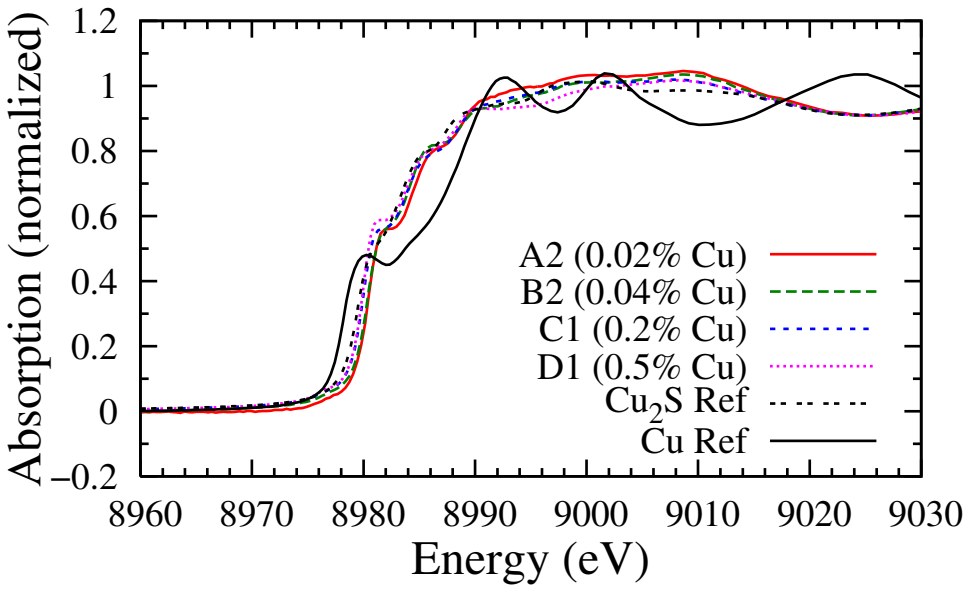

Figure 4.28: Plots of the Cu XANES for ZnS:Cu for concentrations 0.02, 0.04, 0.2, 0.5% and two reference materials Cu_2S and Cu metal. The scans were normalized at higher energies.

variations in weak structure along the edge, such as the feature at the half height point on the edge. In addition, the edge for bulk Cu_2S is very similar to ZnS:Cu, but has even less structure. Note that the environment about Cu in the complex Cu_2S structure is quite different from that for Cu on the Zn site in ZnS and that the average edge passes through the middle of the Cu foil edge.

We also used FEFF8.20[Ankudinov *et al.*, 1998b] to calculate the XANES for Cu on an undistorted Zn site with four S neighbors, for Cu on an undistorted Zn site with three S neighbors and a vacancy, and for Cu next to a vacancy but displaced away from the vacancy. These simulations do not look similar to the measured edges; they show significant structure that changes as the environment varies. We had similar difficulties in simulating the edge for CuS; Rehr[Rehr, 2009] suggested that the potentials

for sulfides, needed to simulate the Cu K-edge XANES, are not yet good enough for a quantitative comparison. Despite this limitation of the XANES modeling to elucidate the local distortions, the experimental XANES data are similar over a wide Cu concentration range and the positions are clearly consistent with a Cu 1+ oxidation state.

4.5.6 EXAFS Data Analysis and Discussion

To quantify whether or not a significant Cu-Zn peak exists near 2.4 Å (for interstitial Cu_i site I_1) requires a careful comparison between two fits: one with an interstitial peak and one without. We initially fit the r-space data using theoretical standard EXAFS functions calculated using FEFF8.20.[Ankudinov *et al.*, 1998b] Here we used the known ZnS structure (F-43m, $a = 5.412$) but replaced the central Zn atom with Cu. The standard for the short Cu-Zn interstitial peak ($\sim$ 2.7 Å; six Zn neighbors) was also calculated using FEFF by placing the central Cu atom at the interstitial positions in ZnS.

Because the possible interstitial Cu-Zn peak at 2.7 Å must be small and would occur on the high side of the Cu-S peak, a further complication exists; for many other systems, we have found a systematic deviation on the high-r side of the first r-space peak between EXAFS functions calculated using FEFF and the corresponding experimental standards.[Li *et al.*, 1995; Kvitky *et al.*, 2001; Bridges *et al.*, 2010a] This small deviation can look like a weak peak. Thus in addition to using the Cu-S function calculated from FEFF for $r = 2.343$ Å, we also generated an experimental Cu-S standard from the Zn-S

peak in Zn K-edge data for ZnS NCs following the procedures described in detail by Li *et al.* [1995]. We compare these two Cu-S functions in Figure 4.29; here, we have fit the experimental standard using the FEFF function by varying r, σ (width of the pair distribution function), the amplitude, and a small E_o shift. For this experimental Cu-S function, the S_o^2 parameter is 0.98; other parameters are given in Figure 4.29. This comparison shows that the difference between the theoretical and experimental functions on the high-r side of the Cu-S peak is quite small (smaller than observed in many other systems).

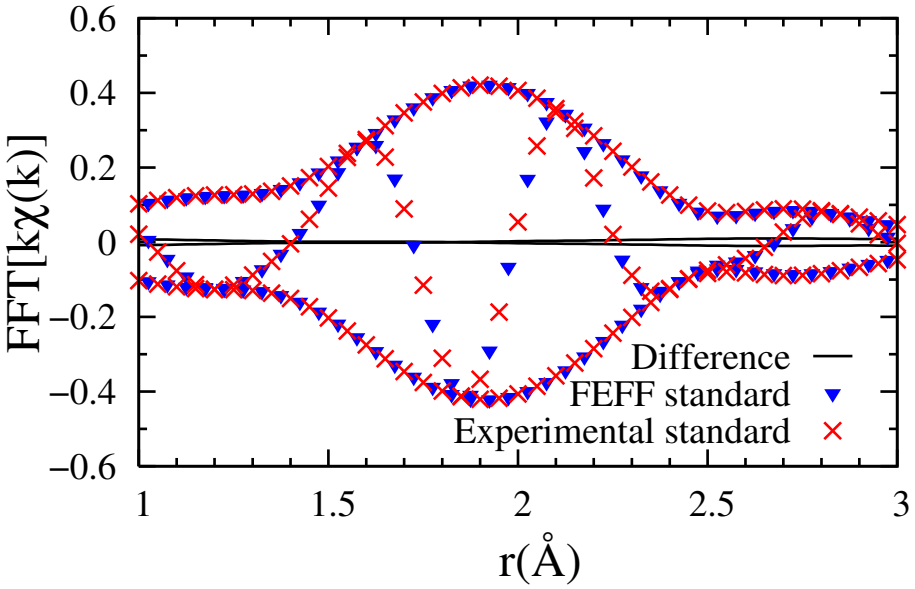

Figure 4.29: Experimental and theoretical Cu-S standards in r-space. Note the nearly identical shapes. We fit the experimental function using the FEFF standard over the r-range 1.2–2.5 Å; the fit parameters are r = 2.345 Å, σ = 0.064 Å, E_o shift = –9.4 eV and S_o^2 = 0.98.

An even more important benefit of using an experimental standard is that it

also provides a more accurate means of estimating the number of S neighbors about Cu, because the standard described above was made from a NC sample (same sample geometry), and has exactly four S neighbors. In particular, when using the experimental standard there is no amplitude correction factor (*i.e.* $S_o^2 = 1$) as is generally needed when using FEFF standards; then the amplitude $= N \cdot S_o^2$ where N is the coordination number, and these two factors cannot be separated.

We first carried out 1-peak fits in r-space using FEFF and experimental Cu-S functions over a short r-space range (1.4–2.2 Å). For all samples, the results for the 1-peak fits are very similar, as was expected from the similar r-space scans in Figure 4.27. The main difference between using FEFF and experimental Cu-S functions is a difference in σ, since the experimental function already includes some thermal motion disorder ($\sigma^2 = 0.0041$ Å^2) while the FEFF standard does not. We have from 4–7 scans for each of the five samples; 25 scans in total. Each scan is fit separately and then the average of the amplitudes and σ^2 (or $\Delta\sigma^2$ for the experimental standard) were determined for each sample. The RMS variation in the number of neighbors is < 0.2, as determined from variations between the 5 scans for each sample.

These 1-peak fits done with an experimental Cu-S function show that the number of S neighbors varies between 3.0 and 3.3 for all samples (see Table 4.4). Thus, a significant fraction of Cu atoms must have a nearest neighbor S vacancy, in some cases perhaps as a result of Cu being near the surface. Since the NCs were synthesized with a very slight deficiency of S and the surface is expected to be rich in Zn atoms over S, this must be considered. However, because the Zn K-edge data show no evidence

# of S neighbors	A1	A2	A3	B1	B2
1-peak fit	3.2	3.0	3.0	3.1	3.0
multipeak fit	3.3	3.1	3.0	3.1	3.1

Table 4.4: Number of S nearest neighbors about Cu. Fit using the experimental Cu-S function with an r-range of 1.4–2.2 Å and FFT range of 3.5–10.5 $Å^{-1}$. RMS variation in the number of neighbors is < 0.2. Decreasing the FFT range to 4–9 $Å^{-1}$ slightly increases the number of neighbors by 0.1–0.2.

for S vacancies about Zn, and since no red emission line (associated with excess S vacancies[Shionoya *et al.*, 1966]) is observed, the overall concentration of S vacancies must be small. The change in the PL data with Cu concentration[Corrado *et al.*, 2009] shows that Cu is incorporated into the ZnS NCs but provides no information about the local environment; however, the EXAFS data are primarily consistent with defect models for which the Cu_{Zn}^{+} defects are compensated by nearest neighbor S vacancies.

Because Cl is a neighbor to S in the periodic table, the S and Cl backscattering functions are too similar to be able to differentiate between S and Cl neighbors and the fact that the Shannon ionic radii are nearly identical means there is no expected significant lattice distortion; thus, a few of the $\sim$ 3–3.3 nearest neighbors might actually be Cl. However, Cl^{-} on a S^{2-} site will charge compensate Cu_{Zn}^{+} defects, so we do not expect both a S vacancy and Cl^{-} as nearest neighbors for a given Cu site. The large number of nearest neighbor S vacancies about Cu, inferred from the decreased coordination number ($\sim$ 3 instead of 4), suggests that the number of nearest neighbor Cl^{-} is likely small.

As to the question of whether the Cu dopants are mostly in the surface layer versus on interior sites, a second result from the 1-peak fits is that the Cu-S distances

are shorter than the Zn-S distance of the host lattice; 2.26–2.27 Å for the 0.02% and 0.04% Cu samples, compared to 2.34 Å for Zn-S. Since, as discussed above, a large fraction of Cu sites have a missing S neighbor, we consider two cases: Cu at an interior site with a neighboring S vacancy, and Cu at the surface. For the interior site, the short Cu-S distance may arise from a [111] displacement of Cu—attracted towards the three remaining S^{2-} and displaced away from the vacancy. In that case, the twelve Zn second neighbors will no longer be at uniform distances; the Cu-Zn peak splits into three: one at a shorter pair distance, one with the pair distance nearly unchanged, and the third at a longer distance, with the number of Zn neighbors for these peaks in the ratio 3:6:3. Using the ZnS structure and assuming little distortion of the host lattice, the contraction of the Cu-S bond for the first peak can be directly related to a Cu off-center displacement, d, and hence the distances for the resulting Cu-Zn peaks. The observed shortening of the Cu-S bond by ~ 0.08 Å corresponds to $d = 0.24$ Å, and the Cu-Zn peaks will split by roughly $\pm$ 0.2 Å. Such a large splitting of the Cu-Zn peaks will dramatically reduce the amplitude of the Cu-Zn peak (the real parts of the FFT are then out of phase) and can easily explain the very small amplitude observed between 3 and 4 Å in the r-space plots.

If instead most of the Cu are in a surface layer of the ZnS NC (to account for the change in PL), then there could also be a reduced number of first neighbor S and second neighbor Zn atoms. We considered this in some detail by simulating the EXAFS assuming there are only three S atom first neighbors (instead of four) and either four or six Zn second neighbors (instead of twelve); we also included a significant broadening

of the distribution functions with $\sigma^2 = 0.006$ Å^2 (*i.e.* corresponding to a bond length variation of order 0.08 Å). These simulations are shown in Figure 4.27e. Even with such a reduced number of neighbors and a significant broadening, the simulated Cu-Zn second neighbor peak in Figure 4.27e is far larger than the Cu K-edge data at 10 K (Figure 4.27a–c). To systematically reduce the Cu-Zn peak to the tiny amplitude observed for every sample would require an additional large broadening $\sigma^2 \sim 0.04$ Å^2.

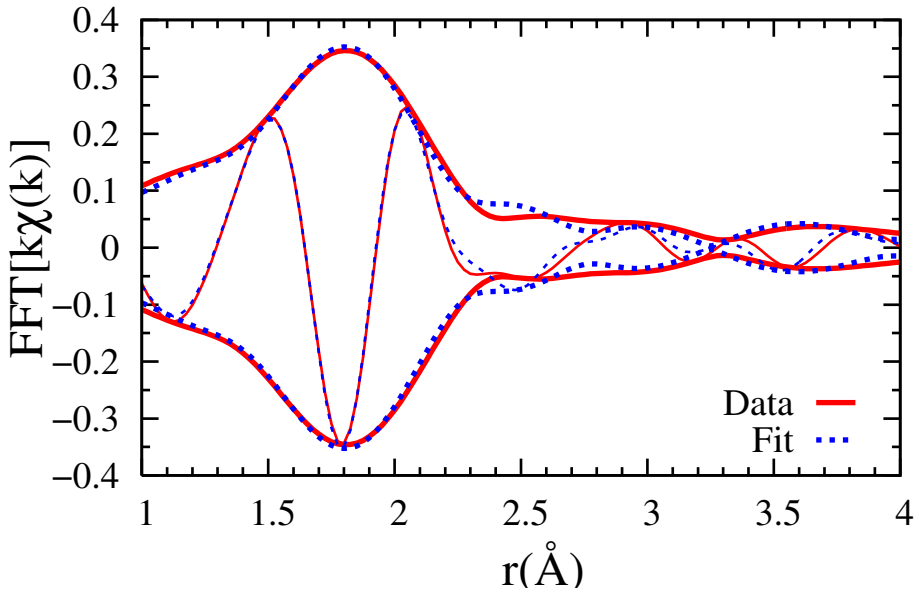

Figure 4.30: A fit of the data for sample A2 from 1.2–3.8 Å to a sum of the experimental Cu-S function and three Cu-Zn FEFF functions; the distances for the Cu-Zn functions are calculated from the Cu-S bond contraction as discussed in the text and tabulated in Table 4.5. Note that only five parameters are varied: δr_1 for the Cu-S peak and σ_i for each peak.

To test the off-center displaced model (shown in Figure 4.31), we carried out a highly constrained fit over the r-range 1.2–3.8 Å, using a sum of the experimental Cu-S function and three Cu-Zn FEFF peaks initially calculated for the Zn-Zn distance (3.8 Å). The Cu-Zn distances in the fit were determined from the contraction of the Cu-S

Sample(% Cu)	δr_1	r_1	$(\Delta\sigma)^2$	r_2	r_3	r_4
A1 (0.02)	-0.076	2.267	0.0026	3.615	3.835	4.044
A2 (0.02)	-0.086	2.257	0.0025	3.587	3.837	4.073
A3 (0.02)	-0.085	2.258	0.0025	3.591	3.837	4.069
B1 (0.04)	-0.073	2.272	0.0023	3.623	3.835	4.036
B2 (0.04)	-0.086	2.257	0.0024	3.587	3.837	4.073

Table 4.5: Fit results; distances in Å for Cu-S (δr_1 and r_1) and the three Cu-Zn peaks (r_i; i = 2–4) for the off-center Cu model. These are average fits; the relative errors for r_1 are less than 0.01 Å. The third column is the excess broadening (in Å^2) of the Cu-S peak relative to the experimental standard.

bondlength; if δr_1 is the change in the Cu-S bond length, then the changes of the Cu-Zn distances are $2.78\delta r_1$, $-0.114\delta r_1$, and $-2.875\delta r_1$. The Cu-S amplitude was held at the value obtained in the short fits (1.4–2.2 Å) discussed above and the number of neighbors for the three Cu-Zn peaks in the ratio 3:6:3. Only five parameters were varied: the Cu-S bond length and σ for each peak. An example of such a fit is given in Figure 4.30, and the resulting distances are tabulated in Table 4.5; the variation in the Cu-S bond length between samples is very small, $\sim$ 0.01 Å. Note that in such fits, it is the oscillating real and imaginary parts of the FFT that are fit, not the amplitude envelope. Figure 4.30 illustrates how well the phase for the real part of the FFT is modeled over most of the r-space fit range. Although better fits can be obtained by letting the three Cu-Zn distances vary independently, the amplitude of the data is very small and the fractional variation from trace to trace in the 3–4 Å range does not support a more extensive fit.

We noted that if one assumes that the shortened Cu-S distances arise from a [111] displacement of Cu away from the vacancy and towards the three S^{2-}, then the Cu-Zn peak would have a large splitting. A fit based on this model describes the data

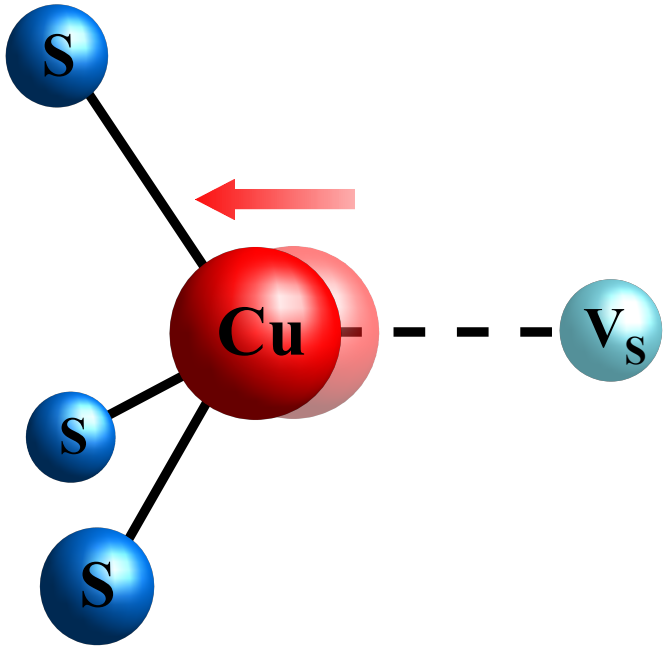

Figure 4.31: The local environment about CuS in ZnS showing the Cu (red) displaced away from a S vacancy (light blue) and towards the three remaining S neighbors (blue).

very well and suggests that the Cu is in a distorted site with Cu^{+}_{Zn} displaced roughly 0.24 Å away from a neighboring S vacancy. Such a distorted Cu site would have C_{3v} symmetry—the symmetry observed in early work by Urabe *et al.* [1968]. This reduced symmetry will further split the Cu 3d states; the t_2 states will split into e′ and a_1. Thus, there are three energy levels for Cu on which excited holes may be found: a_1, e′, and e. This might explain the fact that there are three main EL emission lines that decrease in intensity in exactly the same way, as an AC EL device degrades.[Stanley *et al.*, 2010]

It is not clear whether the low concentration S vacancies we find adjacent to Cu^{+}_{Zn} have the same properties as isolated V_S, particularly whether the donor level

for V_S in the Cu^+_{Zn}-V_S complex is responsible for the trap states 0.6–0.8 eV below the conduction band. Differentiating between these two distinct types of V_S is difficult.

In addition, we note that the excess broadening of the Cu-S peak in fits using the experimental standard (see Table 4.5) is small, only 0.0023–0.0026 Å^2 relative to the experimental standard. Thus although the number of S neighbors is reduced, the disorder of the remaining Cu-S bonds is low.

Finally, we address the possibility of any interstitial Cu, starting with site I_1. In this case, Cu_i provides the charge compensation for a nearby Cu^+_{Zn} defect so no S vacancies should be present and a large off-center displacement of Cu_i is not expected for this small fraction of Cu. For each of the samples we carried out another fit, adding a fourth Cu-Zn peak near 2.7 Å, to represent the interstitial Cu-Zn distance in cubic ZnS. Three additional parameters are required for this peak: an amplitude, shift in r (δr_5), and σ_5. In this fit, we started with 0.5 Zn neighbors (*i.e.* $\sim$ 8% Cu_i sites) and constrained the shift of the Cu-Zn distance to ± 0.04 Å about the nominal distance. In all such fits, the amplitude for the interstitial peak goes to zero; there is no significant peak close to 2.7 Å. When we allowed the distance to vary up to ±0.3 Å about the nominal distance, a range of slightly improved fits occur both for significantly longer and shorter distances for r_5. The results varied widely (different amplitudes and σ's); the negative shifts were typically –0.2 Å while positive shifts ranged from 0.2–0.3 Å. Since we are fitting to both the real (R) and imaginary (I) parts of the FFT instead of just the amplitude, the inability to get a fit when we constrain the Cu-Zn distances to ± 0.04 Å indicates that the shape of R and I for the data FFT is quite different than

that for the theoretical Cu-Zn function.

The improvement in these fits for large δr_5 was small, considering that three additional parameters are needed to describe the interstitial peak. To quantify the discussion, we used the Hamilton F-test[Downward *et al.*, 2006] to determine whether adding the extra peak was significant, and applied it to fits for each scan of every sample (25 fits total). Overall, this test indicated that the interstitial peak was not significant, with confidence levels for most fits being below 67% and well below the necessary 95% confidence level. Fits for a few scans gave confidence levels near 90%, but this is to be statistically expected with 25 fits and the large variation in parameters (amplitudes and σ_5) between fits suggest that the results are dominated by noise.

For the other possible interstitial site, I_2, the closest neighbors are Zn/Cu atoms at approximately 2.34 Å. This interstitial void is large enough to accommodate the large S^{2-} ion, whereas the Cu^{+1} ion is much smaller; however the interaction between Cu_i and the neighboring Zn^{2+} is repulsive. It is thus not clear if the neighboring Zn atoms are displaced. We start assuming the ZnS host lattice is not significantly distorted and generated a Cu-Zn FEFF standard for this pair. Then we fit the first peak in the Cu K-edge data (see Figure 4.27) to the sum of the Cu-S experimental peak and the interstitial Cu-Zn peak, starting with various fractions of interstitial site occupations. If we restrict the interstitial Cu-Zn distance to not vary by more than ±0.05 Å, the amplitude of this peak goes to zero and the peak broadens such that the Cu-Zn EXAFS peak has negligible amplitude. Next we let the Cu-Zn distance vary up to ± 0.2 Å. For a large contraction of –0.2 Å, the phase of the real part of the Cu-Zn peak is 180 degrees

out of phase with the Cu-S peak and the amplitude is low, corresponding to $\sim 2\%$ of the sites. Another fit with a low amplitude is obtained if the distance expands by 0.15 Å to 2.5 Å. We consider these large distortions to be unreasonable for the ZnS lattice. Thus within our uncertainty, the fraction of Cu interstitial sites is very small, no more than 2% and possibly much smaller.

4.5.7 Discussion

We have investigated, for the first time, the local environment about dilute Cu (0.02% and 0.04% Cu) in a number of ZnS:Cu,Cl nanocrystals. From the XANES, we verify that the Cu is in a 1+ oxidation state and using the EXAFS technique, we find that for all samples, the number of S neighbors is significantly below 4 ($\sim$3.2), indicating that most Cu atoms have a nearest neighbor S vacancy. In addition, the second neighbor Cu-Zn peak is surprisingly weak, which requires a huge distortion of the Cu-Zn pair distribution function; the amplitude is much smaller than expected for an atom in the surface layer. Furthermore, the Cu-S distance is significantly shorter ($\sim$0.07–0.08 Å) than the Zn-S distance in the host.

We noted that if one assumes that the shortened Cu-S distances arise from a [111] displacement of Cu away from the vacancy and towards the three S^{2-}, then the Cu-Zn peak would have a large splitting. A fit using this model, with the shift of the Cu-Zn distances determined from the Cu-S bond contraction, describes the data well. Thus, the EXAFS data suggest that the Cu is in a distorted site with Cu^{+}_{Zn} displaced roughly 0.24 Å away from a neighboring S vacancy, resulting in the Cu site having C_{3v}

symmetry which would further split the Cu 3d states, leaving three energy levels on which excited holes may be found.

Finally, we considered the possibility of some interstitial Cu_i sites which would charge compensate Cu^+_{Zn} defects but should have no nearby vacancies. Site I_1 has a distinctive signature—a Cu-Zn peak at a rather short distance of 2.7 Å. Adding a peak at this distance did not significantly improve the fits, and if the distance was constrained to be close to the expected distance, the amplitude of the peak went to zero. The second site I_2 has four nearest neighbor Zn/Cu atoms at the normal Cu-S distance (2.34 Å). Including a very short Cu-Zn/Cu peak (near 2.34 Å) in the fit did not improve the fit significantly and if the distance was constrained within ± 0.05 Å, the amplitude went to zero. Thus, we conclude that if there are Cu_i sites, the fraction of Cu_i sites must be very small, $< 2\%$ of the total Cu sites. These results provide a better fundamental understanding of the local structure of the Cu dopant in ZnS nanocrystals, which is significant for understanding the PL emission centers and for applications including electroluminescence.

Chapter 5

Thermoelectric Clathrates

5.1 General Introduction

5.1.1 Motivation and Applications

Thermoelectric materials function directly as solid-state heat pumps or heat engines, requiring no conventional moving parts. When a thermoelectric device is placed between a heat source and a heat sink, a voltage is generated between the two, functioning as a heat engine. Similarly, when a voltage is applied, it operates as a heat pump and transfers thermal energy from one side of the device to the other.

Unlike traditional heat pumps and heat engines, thermoelectrics are easily scalable to small sizes and can be made in flexible shapes, making it possible to put them in places which would otherwise be impractical. Thus, despite their low efficiencies, they have the potential to be used to recover heat which would otherwise be wasted or to use targeted cooling, cooling a smaller volume, and thereby increase overall efficiency.

While thermoelectric materials have long been used in thermocouples, Peltier coolers, and radioisotope thermoelectric generators, their efficiency is still quite low. Many different materials are now being studied in order to increase the efficiency of thermoelectric devices.

5.1.2 Thermoelectricity

From a basic viewpoint, thermoelectric devices work by using materials with a low thermal conductivity of the device, forcing the majority of the heat transfer to occur via the charge carries. For a thermoelectric material connected to a heat source and a heat sink, charge carriers from the hot side of the device move toward the cold side of the device, generating a voltage and, by connecting a load, a current. On the other hand, a thermoelectric device with a voltage applied across it will preferentially move the warmer charge carriers across the device, resulting in one side warming and the other cooling which can either be forced to go in one direction (as in a heat pump) or the electrical potential generated by their motion can be used to generate electricity.

Thermoelectric materials are typically characterized by their thermoelectric figure of merit, ZT.

$$ZT = S^2 T \frac{\sigma}{\kappa} \tag{5.1}$$

where S is the Seebeck coefficient, σ is the electrical conductivity, and κ is the thermal conductivity.

Currently, the best materials have figures of merit approaching 2.5, though

there is no theoretical upper limit. So in order to increase the figure of merit, it is desirable to increase the electrical conductivity, σ, and decrease the thermal conductivity, κ.

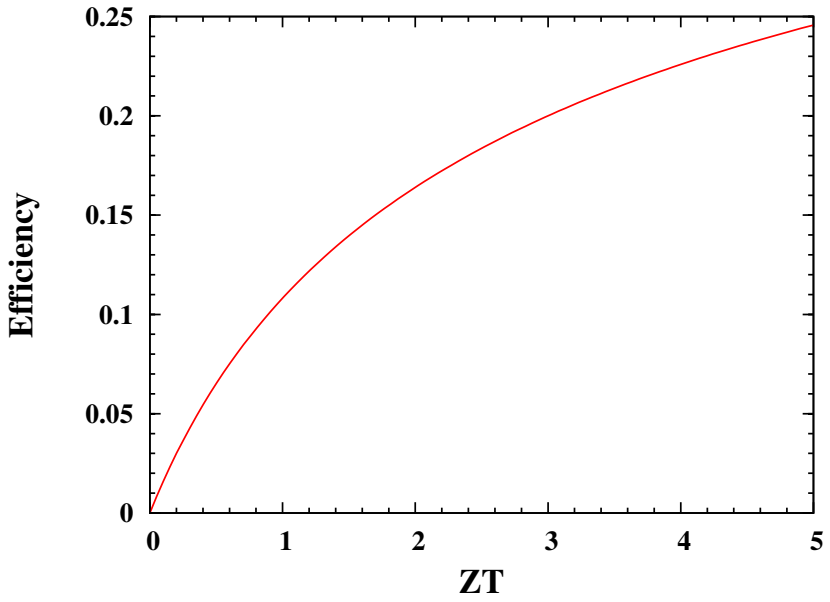

Figure 5.1: Efficiency as a function of ZT for a device operating at $T_H = 2T_C$, so the Carnot limit is 0.5.

The maximum efficiency of a thermoelectric heat engine is shown in Figure 5.1, and given by the equation:

$$\eta_{max} = \frac{T_H - T_C}{T_H} \frac{\sqrt{1+ZT}-1}{\sqrt{1+ZT}+T_C/T_H} \tag{5.2}$$

where T is the average temperature.[Snyder and Ursell, 2003] Due to the diminishing returns, it is estimated that a device made of materials with a ZT of ~ 4 would make thermoelectric devices economically feasible in most applications.

5.1.3 Materials

Finding promising materials for thermoelectric applications is difficult because, typically, electrical and thermal conductivities go hand in hand, and looking at Equation 5.1, it is necessary to isolate the two in order to maximize ZT. Despite this difficulty, there are a variety of novel materials which exhibit high figures of merit. Common materials are Bi_2Te_3 ($ZT = 0.8$–1.0)[Chung *et al.*, 1997], PbTe:Tl ($ZT = 1.5$)[Heremans *et al.*, 2008], and when materials are nanostructured ZT for Bi_2Te_3 increases to $\sim$ 2.4[Venkatasubramanian *et al.*, 2001] and even silicon nanowires (bulk $ZT \approx 0.01$) have a ZT of $\sim$ 1.0.[Boukai *et al.*, 2008]

Clathrates are a class of materials which have cages with guest atoms inside, which can rattle around and scatter phonons, decreasing thermal conductivity, without significantly decreasing electrical conductivity (see Figure 5.2). In fact, many clathrates have a glass-like thermal conductivity while being adjustable large-bandgap semiconductors, making them suitable as high temperature thermoelectrics.[Nolas *et al.*, 1998]

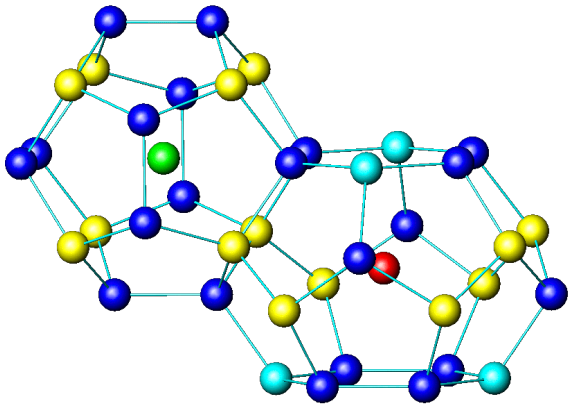

Red & Green	Rattler Atoms
Yellow	M1 Site
Dark Blue	M2 Site
Light Blue	M3 Site

Figure 5.2: Cages within the structure of a type I clathrate. Legend/key at right indicates colors of the crystallographic sites.

There are many different types of clathrates, with different crystal structures, but only three are known to exhibit good thermoelectric properties: types I, II, and VIII. The unit cell of type I clathrates consists of 6 24-atom cages and 2 20-atom cages, along with 8 rattler atoms, with the rattler atom inside the larger cage sitting slightly off-center.[Baumbach *et al.*, 2005] Type II clathrates have a much larger unit cell consisting of 8 24-atom cages, 16 20-atom cages, and 24 rattlers.[Mano *et al.*, 2011] Type VIII clathrates have the same chemical formula as the type I clathrates, but the unit cell is made up of 8 identical 20-atom cages and 8 rattler atoms.[Kono *et al.*, 2010] Thus far, type I clathrates (as shown in Figure 5.2) have been the focus of most research.

Much research is currently being directed toward trying out new combinations of elements in clathrate structures and measuring their transport parameters and thermoelectric figure of merit. However, to guide future syntheses, it is beneficial to develop a more complete understanding of the origin of these transport properties from the local structure.

5.2 Smaller or Larger Cage Atoms

5.2.1 Background

Each of the crystallographic sites (M1, M2, and M3; visible in Figure 5.2) are occupied by a mixture of Ga and X (X = Ge,Sn,Si). Due to this non-uniform arrangement of elements among the crystallographic sites, diffraction cannot determine the disorder for each element, instead giving an average over each of the crystallographic

sites. Therefore, we use EXAFS to probe the individual elements and determine the precise bond lengths (*i.e.* for BaGaSn: Ga-Sn, Ga-Ga, Sn-Sn) and the relative fractions of these bonds by comparing our experimental results with theoretical calculations.

After promising studies of BaGaGe, samples of the similar compounds BaGaSn and BaGaSi have been made and studied in order to better understand the physical basis for thermoelectrics with high figures of merit. Based on simple size differences between the atoms, it was expected that BaGaSn would be slightly larger, and BaGaSi would be slightly smaller, when compared to BaGaGe. Further, it is plausible that both would be more disordered than BaGaGe due to the difference in size compared to the other lattice element, Ga.

Previous work on BaGaSn[Suekuni *et al.*, 2009] shows the lowest thermal conductivity of all the type I clathrates and our previous studies[Kozina *et al.*, 2009] verified the low occurrence of Ga-Ga bonds. On the other hand, BaGaSi is not strictly promising for practical thermoelectric applications, but it is not well understood why due to the lack of agreement between theoretical and experimental results.[Blake *et al.*, 2001]

5.2.2 Sample and EXAFS Details

Single crystals were prepared by Takabatake using methods similar to those described in the articles by Avila *et al.* [2008] and Suekuni *et al.* [2008]. The samples were then powdered with a mortar and pestles and shaken through a 25 μm sieve. Next a thin layer was brushed onto two pieces of Scotch tape, which preferentially adheres to the smaller particles, and subsequently taped together, forming an encapsulated

double layer of $\sim$ 5 μm particles. The double tape layer was then cut into 2 mm by 16 mm strips which were stacked in order to obtain a thickness of 0.3–0.9 absorption lengths, and mounted in a liquid helium cryostat. We collected EXAFS data at several temperatures between 6 K and 300 K.

All data were collected on beamline 10-2 at the Stanford Synchrotron Radiation Laboratory (SSRL) in transmission mode. Ba K-edge data were collected using a Si(220) double monochromator, detuned to 80% to reduce harmonics; with a slit height of 0.3 mm, the resulting incident X-ray energy resolution was 7 eV for the Ba K-edge. A Si(111) double monochromator, detuned to 50% to reduce harmonics, was used to collect the Ga K-edge data. Using a slit height of 0.5 mm, the resulting X-ray energy resolution was 2 eV. Sn K-edge data were also collected using a Si(220) double monochromator, detuned to 50% to reduce harmonics. Using a slit height of 0.3 mm resulted in an X-ray energy resolution of 4 eV at the Sn K-edge. Due to the low energy of the Si K-edge (1.8 keV), we were unable to collect data for Si, and are limited to using the Ga K-edge to study the Ga-Si lattice in $Ba_8Ga_{16}Si_{30}$.

After collecting the data, we used the RSXAP data reduction package to reduce the data.[Booth, 2012] The REDUCE software removes a pre-edge background, consistent with the Victoreen formula, subtracts a spline-fit from the spectrum above the edge, converts into k-space, and fast Fourier transforms using a Gaussian-rounded window to get the results in r-space. The RSFIT program fits the real and imaginary parts of the r-space experimental data to theoretical EXAFS functions generated by FEFF8 in order to determine the amplitude, position r, and width, σ, of the pair dis-

tribution functions for each atom pair.[Ankudinov *et al.*, 1998a] While the width σ at a given temperature is dependent primarily on the degree of correlation in the atomic vibrations of various atom pairs, it is useful to note that normally, σ grows as the pair-distance increases.

Typically, we determine the parameter ΔE_0 (the difference between the the experimental edge energy, defined as the half-height edge energy, and the energy for which $k = 0$ for the theoretical standards) at low temperature (< 100 K), and fix it at that value for the higher temperature fits.

5.2.3 Comparison of the Rattler EXAFS

The Ba K-edge EXAFS provides a useful summary/overview of what we find when analyzing the cage elements, and is easy to compare each of the compounds and understand what is going on from a single figure. Figure 5.3 shows two main differences as the cage atom sizes are changed: a decrease in amplitude and shift toward lower r. In particular, the BaGaSn also shows a potential split peak due to the interference dip visible at ~ 2.8 Å.

This amplitude decrease indicates that the neighborhood around Ba becomes more disordered in the progression from BaGaGe to BaGaSi to BaGaSn. This increased disorder is consistent with the decreasing thermal conductivity, as can be seen in Figure 7 of Suekuni *et al.* [2008]. The shift to shorter r means that there are some significantly shorter Ba-X distances. When considering the bond distances, it is also important to note that EXAFS preferentially picks out the shortest distances, due in part to a $1/r^2$

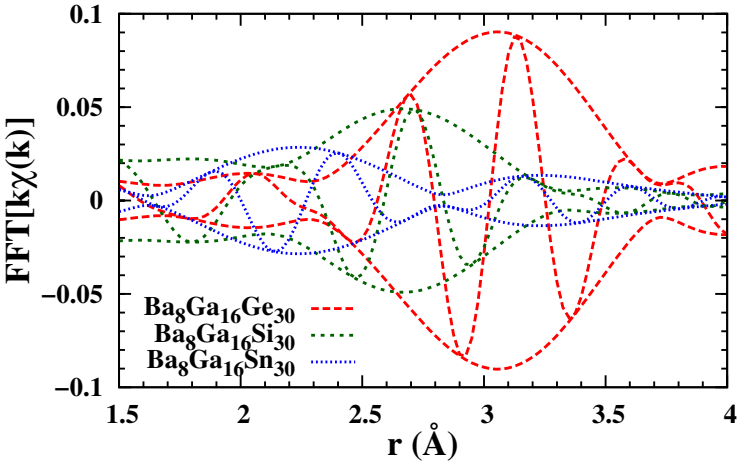

Figure 5.3: Ba K-edge EXAFS data for the three clathrate compounds. The shift and decrease in amplitude suggests that the Ba "rattler" environment becomes more distorted in the Si and Sn compounds. For these data we used an FFT window of 3.5–10 Å^{-1} , Gaussian broadened by $\sigma = 0.3$ Å^{-1}.

sensitivity of EXAFS, plus the general result that the closest neighbors usually have stronger bonds which leads to a smaller broadening, σ of the PDF. Thus, the peak in r-space generally corresponds with the shortest bond, but does not mean there are not a broad distribution of longer bonds.

All of these signs point to the conclusion that the cages are buckling in BaGaSi and BaGaSn, resulting in some of the neighbors being closer to the Ba rattler and others being farther.

5.2.4 $Ba_8Ga_{16}Sn_{30}$

For BaGaSn, EXAFS data were collected at both the Ga and Sn K-edges. For each edge, we fit the data using two Gaussians (either Sn-Sn and Sn-Ga for the Sn K-edge, as shown in Figure 5.4, or Ga-Ga and Ga-Sn for the Ga K-edge, not shown).

This allows us to determine each of the three elemental bond lengths present in the cage structure.

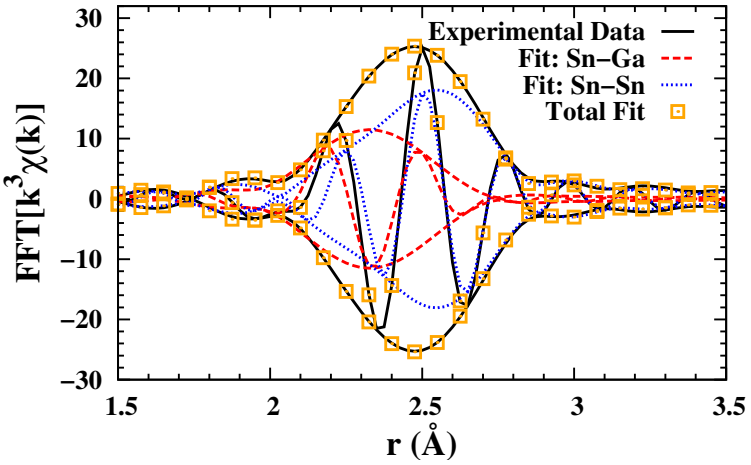

Figure 5.4: r-space plot of experimental data at Sn K-edge for $Ba_8Ga_{16}Sn_{30}$, along with 2-peak fit (Sn-Sn and Sn-Ga). For these data we used an FFT windows of 3.5–15 Å^{-1}, Gaussian broadened by $\sigma = 0.3$ Å^{-1} and fitted over the range 2.0–2.8 Å.

These distances are each plotted (as a function of temperature, though there is little change) along with the results from X-ray diffraction in Figure 5.5. Here, we can see that the Sn-Sn and the Ga-Ga bond distances both fall outside the range reported by diffraction, due to the differences between the local structure and the average structure. It is also useful to keep in mind that there are very few Ga-Ga bonds[Kozina *et al.*, 2009], and that the Sn-Sn and Sn-Ga bonds dominate.

5.2.5 $Ba_8Ga_{16}Si_{30}$

We can see from the fits in Figure 5.6 that the actual elemental bond lengths are 2.46 Å for Ga-Si and 2.52 Å for Ga-Ga, though, in agreement with Kozina *et al.*

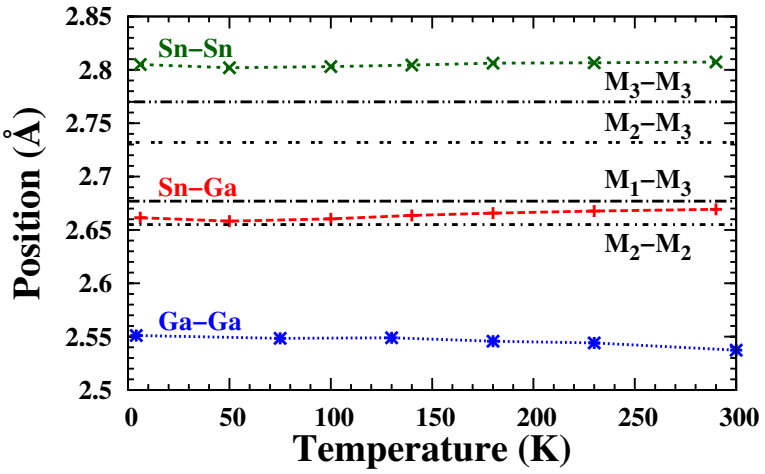

Figure 5.5: Comparison of the elemental bond lengths (as a function of temperature) with the crystallographic bond lengths, from diffraction, for $Ba_8Ga_{16}Sn_{30}$.

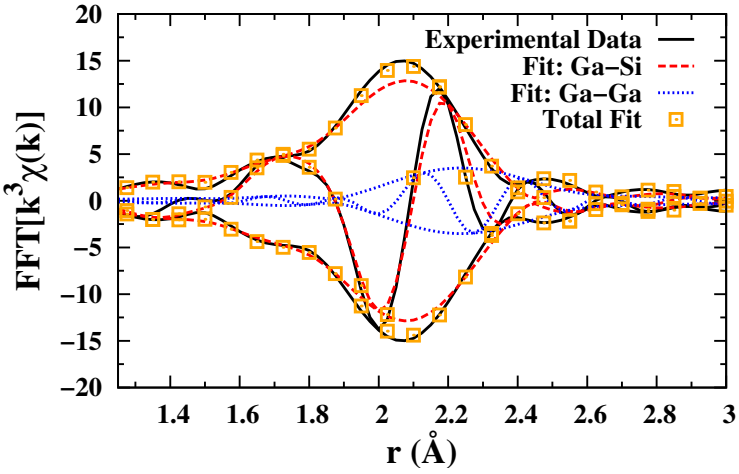

Figure 5.6: r-space plot of experimental data at Ga K-edge for $Ba_8Ga_{16}Si_{30}$, along with 2-peak fit (Ga-Si and Ga-Ga). For these data we used an FFT windows of 3–14.5 $Å^{-1}$, Gaussian broadened by $\sigma = 0.3$ $Å^{-1}$ and fitted over the range 1.7–2.4 Å.

[2009], the Ga-Ga bond is generally avoided, occurring with only $< 10\%$ the amplitude of the Ga-Si bond. Though were were unable to collect Si EXAFS data, we assume that because Si is smaller than Ga, it is most likely that the Si-Si bond distance is significantly smaller than the Ga-Si bond.

5.2.6 Discussion

Thus, it is apparent that the change to non-uniform cage atom sizes causes increased disorder within the cages and likely causes cage buckling since the lattice parameter is not changing significantly. The fact that, compared to BaGaGe, BaGaSi and especially BaGaSn have significantly increased disorder, explains the lower thermal conductivity and suggests that electrical conductivity is also greatly decreased. Further, we expect that the electrical conductivity will be decreased even more than the thermal conductivity, which is already low as a result of the rattler-induced scattering of phonons. This, in turn, explains why the thermoelectric figure of merit is not improving for these materials, but is actually getting worse.

Chapter 6

Magnetism in Complex Oxides

6.1 Introduction

Doping in complex oxides is a fundamental route for control of the many degrees of freedom. However, depending on the nature of the underlying ground-state, the impact on the local electronic structure depends strongly on the balance between on-site energies and the bonding to oxygen[Imada *et al.*, 1998; Goodenough, 2004]. For example, doping in the Mott regime directly changes the valence state of the transition metal ion (*e.g.* manganites) while doping in the extreme of the charge transfer regime (*e.g.* cuprates) results in formation of holes on the oxygen lattice. The case of cobaltites lies in the cross-over region between these two extremes and and a better understanding of the regime may finally answer the decade-old question of why magnetism in $La_{1-x}Sr_xCoO_3$ (LSCO) is unusual.

The parent compound, $LaCoO_3$, is a non-magnetic, small band-gap semicon-

ductor at low temperatures, but develops a weak susceptibility that peaks near 100 K, known as the Spin State Transition (SST). While it is well established that the low-temperature phase is a low-spin (LS) state (S=0)[Yamaguchi *et al.*, 1996], there has been intense debate over the nature of the higher temperature net-spin phase, which could be a mixture of low-spin and either high-spin (S=2), and/or a Jahn-Teller (JT) active intermediate-spin (IS, S=1)[Knížek *et al.*, 2005]. However, our EXAFS experiments[Sundaram *et al.*, 2009; Jiang *et al.*, 2009b] show no JT distortion and are inconsistent with a localized IS state. As x increases, the formal valence of some Co^{+3} changes to Co^{+4}, and the system becomes magnetic. Initially, there is a formation of small magnetic polarons that grow into magnetic clusters leading to the formation of the spin glass phase ($5\% \leq x \leq 18\%$) as ferromagntic (FM) droplets, and then a full FM phase develops above 18% with a concomitant metal to insulator transition (MIT)[Itoh *et al.*, 1994; Anil Kumar *et al.*, 1998; Sikolenko *et al.*, 2004; Aarbogh *et al.*, 2006; He *et al.*, 2007] (see Figure 5 of Ref. [He *et al.*, 2007] for a phase diagram). With increasing x, the rhombohedral structural distortion gradually decreases and the crystal approaches the cubic perovskite structure[Kriener *et al.*, 2009].

The change in the magnetic properties depending on the Sr doping is usually discussed in terms of Co^{+3}/Co^{+4}; removing an electron from the Co^{+3} LS state will make it magnetic (S=1/2) and from the high-spin state even more magnetic (S=5/2). Since the moment in the FM state is close to 1.8 μ_B[Wu and Leighton, 2003], a change of only the LS state to a S=1/2 state is insufficient to explain the observed moment. Local probes of the element-resolved electronic and magnetic structure can gain insight

into this problem.

Most of the recent studies of the $La_{1-x}Sr_xCoO_3$ systems have used localized models with the dominant interactions being the crystal field splitting (CFS) and the exchange interactions E_ex, which split the Co 3d energy levels into t_{2g} and e_g multiplets and also split up the spin up and spin down states. However, this localized picture is likely not appropriate since the e_g states are spread over a large energy range from low energy bonding states to high energy anti-bonding states.

In our Co K-edge X-ray absorption near edge spectroscopy (XANES) study of cobaltites[Sundaram *et al.*, 2009; Jiang *et al.*, 2009b] the Co K-edge shifts ≤ 0.15 eV as x increases to 0.3, in stark contrast to other Co systems and many manganites, for which the edge shift is roughly 3 eV per valence unit[Sikora *et al.*, 2006; Han *et al.*, 2008; Bridges *et al.*, 2001]. Further, both diffraction studies[Caciuffo *et al.*, 1999; Mineshige *et al.*, 1999] and our EXAFS results[Jiang *et al.*, 2009b] show that the Co-O bond length is nearly independent of x for LSCO; consequently through the bond-valence sum model, the lack of a contraction of this bond with x also indicates no change in Co valence—*i.e.* the 3d electron configuration remains close to d^6. This raises the question: where do the Sr-induced holes go? We argued that a large fraction of the holes are on the O atoms[Jiang *et al.*, 2009b], which can be directly probed at the oxygen K edge. Previous XAS studies at the O K-edge show an evolution with hole doping[Saitoh *et al.*, 1997; Toulemonde *et al.*, 2001]. Existing XMCD studies[Okamoto *et al.*, 2000; Merz *et al.*, 2010] are limited, however. The former normalized the O K-edge data at the first pre-edge peak, resulting in no visible change observed with changing Sr

concentration; the latter only examined one Sr-doped sample. Thus, to date there has been no systematic study of the low hole doping regime to follow the connection with the change in electronic and magnetic states of the cobaltites.

Here, we present a detailed doping-dependent study of the oxygen hole states in $La_{1-x}Sr_xCoO_3$ single crystals. By tracking the first oxygen pre-edge peak, due to Co-O ligand hole states, with polarization-dependent XAS, it is clear that a strong magnetic oxygen state forms with doping and the increase in absorption is tied to a large fraction of the doped holes residing on the oxygen site. The strong XMCD shows directly that there is a non-zero orbital moment on oxygen due to the net magnetic moment on the oxygen site. Detailed analysis shows the moment on oxygen is parallel to the Co moment and increases in magnitude with doping. To understand these results and determine the magnetic structure of O, complementary theoretical work has been carried out by Bruce Harmon and Yongbin Lee. They show that the density of states (DOS) for the 3d electrons are spread over a large energy range with significant e_g character for bonding state below E_F. They also show that the (empty) O density of states (DOS) just above the Fermi level increases with x, and that the O atoms develop a moment, with both a spin and orbital component. Most importantly, the O atoms are no longer equivalent; their properties depend on the number of nearest Sr neighbors.

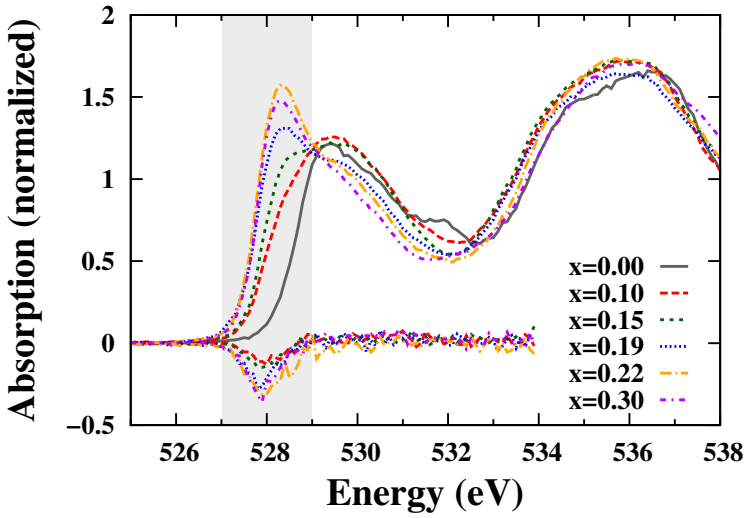

Figure 6.1: XAS (top) and XMCD (bottom, ×5) at the O K-edge. The XAS data were normalized at 550 eV and a self-absorption correction was applied. The corrected XAS data agree well, except at the beginning of the edge (from 527–529 eV) where the number of empty states increases with x and a large increase in the XAS is observed. A significant XMCD signal is only observed over this same small energy range. For x = 0.22 and 0.3, T = 75 K, B = ±1 T; x = 0.19, T = 20 K, B = ±3 T; x = 0.1–0.15, T = 20 K, B = ±5 T.

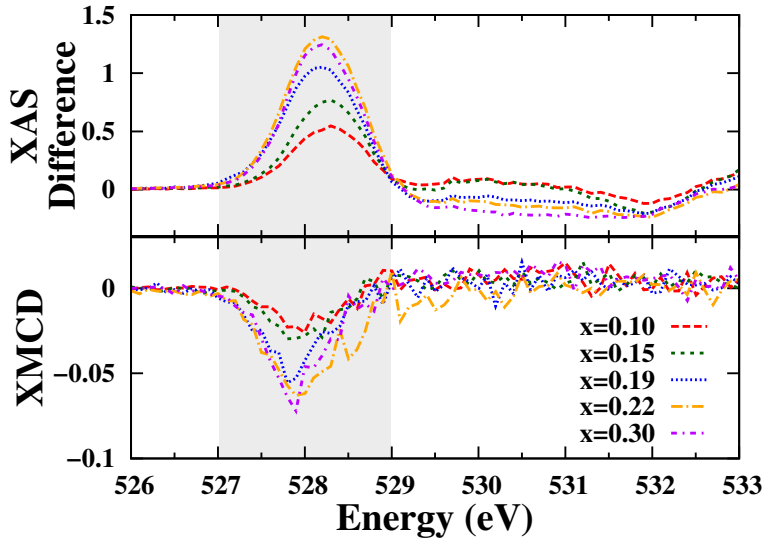

Figure 6.2: Comparison of the change in the O pre-edge XAS (XAS(x)–XAS(0)) with the O XMCD. The XMCD occurs over the same 2 eV range where XAS(x)–XAS(0) is positive. Above 529 eV the differences become slightly negative.

6.2 Experimental Results

XMCD and XAS data for the O K-edge and Co $L_{3,2}$-edges were measured at the Advanced Photon Source beamline 4-ID-C, to probe the magnetization on both sites. A superconducting magnet provided magnetic fields up to $\pm$5T. The energy resolution was $\sim$ 0.15 eV at the O K-edge and 0.3 eV for the Co $L_{3,2}$-edges. Small (randomly oriented) single crystals were mounted on an electrode using Ag paste to collect the current for total electron yield. The X-ray beam was oriented at 45° to the sample surface and the fluorescence detector was at 90° to the beam. Each sample was scraped with a diamond file to remove surface contamination just before mounting. Here we focus on the bulk sensitive O K-edge fluorescence results as the Co $L_{3,2}$-edge data, both XAS and XMCD, are similar to previous work.[Okamoto *et al.*, 2000; Merz *et al.*, 2010]

The XAS fluorescence data at the O K-edge (I_F/I_o, where I_F is the fluorescence signal and I_o the incident flux), and the corresponding XMCD data ($\mu^+ - \mu^-$), where μ^+ and μ^- are the absorption coefficients for +/- circularly polarized X-rays, are shown in Figure 6.1 for x = 0, 0.1, 0.15, 0.19, 0.22, and 0.30. For the XAS plots, a small background was first subtracted and then the data were normalized to 1 at energy 550 eV. Finally, the data were corrected for self absorption following the method in FLUO[Haskel, 1999]. The correction factor is significant (< 1.5 for the first peak), and important to obtain good fluorescence data and to correct the XMCD data. The main results for the XAS data as x increases are a shift of the leading part of the O K-edge to lower energy and an increase in absorption. As has been noted previously[Sarma *et al.*, 1996] and in our theory results below, the weak core-hole interaction at the oxygen K-edge means that the XAS closely follows the shape of the O-projected density of states (DOS). This allows us to make a direct connection with the evolution of electronic structure.

The magnetic state on oxygen is probed by the XMCD, as shown in the lower part of Figure 6.1. A significant signal is only observed over a short energy range ($\sim$ 2 eV) at the beginning of the O K-edge. The XMCD signal increases in magnitude as x increases and is surprisingly large above $x = 0.19$ in correlation with the formation of the FM metallic state. However, the fact that only a small part of the O XAS shows a magnetic signal indicates that not all the O states are magnetic. These data were collected in a high enough B-field that the magnetization is close to saturation. This significant XMCD signal indicates a non-zero orbital moment on the O site[Igarashi and

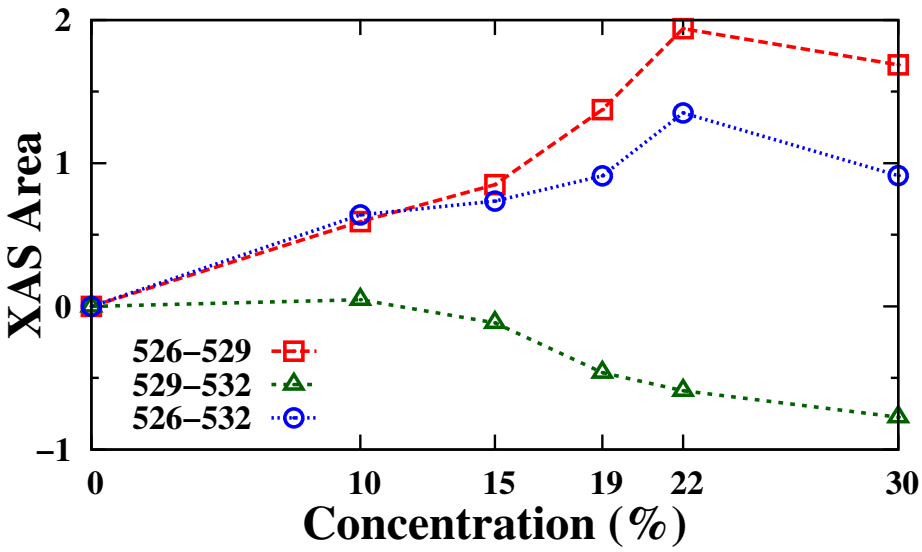

Figure 6.3: Integrals of the difference in O XAS (Figure 6.2) from 526–529 eV (magnetic holes) and from 529–532.5 eV (non-magnetic holes) as a function of x, showing that the change is not linear. For $x \leq 0.15$, the new magnetic holes are associated with FM clusters; over the range 0.15–0.22 where the material becomes fully FM, higher energy holes with no orbital momentum are converted to lower energy magnetic states.

Hirai, 1994].

To visualize how the electronic structure evolves with doping, the Sr-induced change in the XAS defined as XAS(x) – XAS(x = 0) is shown in Figure 6.2. The top panel shows that Sr induces a strong increase in the absorption at lower energy due to the formation of additional unoccupied oxygen ligand hole states. For low Sr concentrations, this new XAS peak shifts to lower energies and increases in amplitude as x increases, with no other changes in the XAS up to $\sim$ 533 eV. Above $\sim$ 15% Sr there is no further shift, but the amplitude continues to increase with x and the XAS difference becomes negative above 529 eV (*i.e.* the O-DOS decreases from 529–532 eV above the MIT). The lower panel shows the XMCD and illustrates that the energy range

for which the XMCD is observed corresponds to the same energy range over which the additional peak in the XAS develops.

6.3 Theoretical Calculations

This increase in empty O-DOS is consistent with adding holes to the O bands as a result of Sr doping, but there is also an induced shift of higher energy O states with quenched angular momentum to lower energy states with net angular momentum. The integrated induced O magnetic holes (DOS integral from 526–529 eV) and non-magnetic holes (from 529–532 eV) are shown in in Figure 6.3; the latter only develops above x = 0.15. There is a clear change in these integrals near $x = 0.18$ where the MIT occurs and the system changes from a spin glass to a FM state. To better understand this evolution, we utilize doping dependent electronic structure calculations.

Recent theoretical studies suggest that a first principles density functional approach from an itinerant electron viewpoint can provide insights about the physical behavior of LSCO.[Takahashi *et al.*, 1998; Ravindran *et al.*, 1999, 2002] This is a homogeneous approach, which is typically applicable for rather itinerant or free-electron systems. In this work we use the electronic states obtained from first principles band structure calculations to calculate theoretical XAS and XMCD spectra for the oxygen K-edge. For the electronic structure we have used a full-potential linearized augmented plane-wave (FPLAPW) method[Blaha *et al.*, 2001] with a local density functional.[Perdew and Wang, 1992] We used $R_{MT}K_{max} = 8.0$ and $R_{MT} = 2.2$, 2.2, 1.9 and

1.6 a.u. for La, Sr, Co and O respectively.

For investigating changes in the electronic structure with Sr doping, a convenient theoretical approach is the virtual crystal approximation (VCA), where the nuclear charge on the La site is reduced by a fraction corresponding to the amount of doping, and the calculated bands are filled with fewer electrons to achieve electrical neutrality. However, recent experiment work including the unusual data described above indicate the need for a deeper theoretical analysis. Also, the VCA is likely not appropriate for oxide materials with strong local bonds and a spatial variation in Sr concentration. Consequently, we have used a 2×2×2 supercell formed of eight pseudo-cubic unit cells, with Sr concentrations 0, 0.125, 0.25 and 0.375 as shown in Figure 6.5. We have kept the cubic structure, even for these lower concentrations since preliminary calculations indicated that the spectral features were more sensitive to the local atomic arrangement compared to the overall cell geometry and the higher symmetry speeds up the calculations. For the supercells 40 k-points were used for the iterations to self-consistency.

The strong interactions between oxygen 2p and cobalt 3d (especially the e_g orbitals) form bonding and anti-bonding states, well separated in the solid as shown in the orbital decomposed DOS in Figure 6.4. The GGA and LDA density functionals yield essentially the same results. Our electronic structure calculations for undoped $LaCaO_3$ are essentially in agreement with those of Takahashi *et al.* [1998] and Ravindran *et al.* [1999]. However, note that the GGA is more sensitive to the electronic correlations and yields a non-magnetic ground state with the experimental rhombohedral distortion. The transition from the non-magnetic to magnetic ground state (with $\sim \mu_B$ moments on Co)

is not unlike the traditional local transition state picture, in the sense that about one Co d electron is promoted from spin down to spin up with very little cost in energy, and is very sensitive to the rhombohedral distortion.

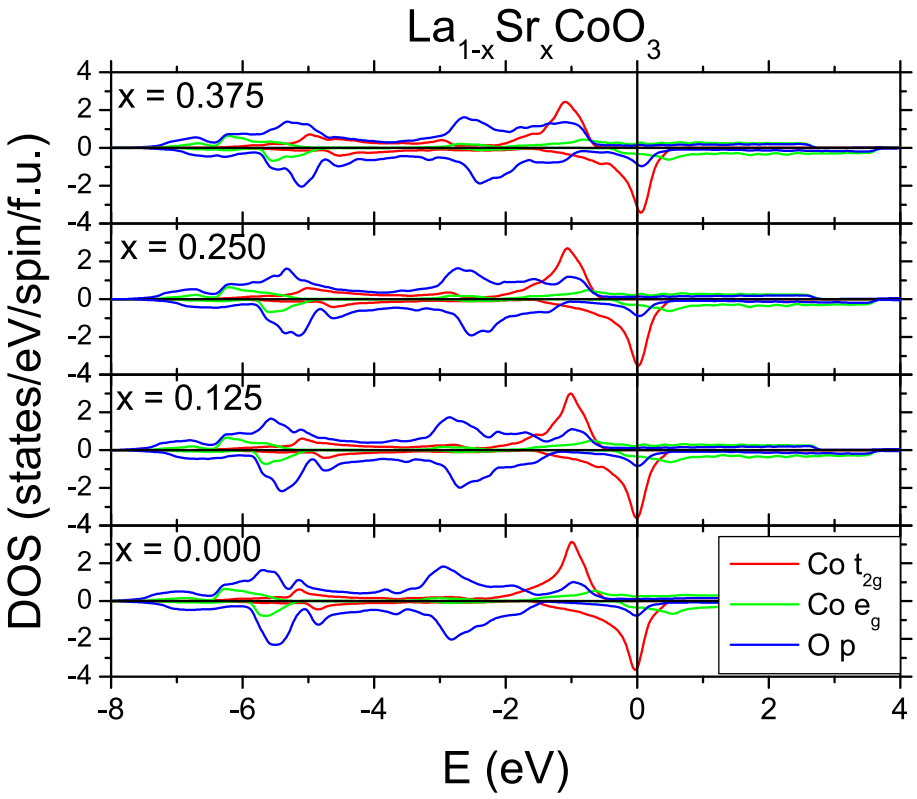

Figure 6.4: The orbitally decomposed DOS for Co 3d and O 2p states for each of the calculated supercells.

From these calculations, we extracted the theoretical O K-edge (mainly a measure of the oxygen partial DOS (PDOS)), as shown as a function of x in Figure 6.6. There is a significant increase in the O K-edge XAS with increasing x, just above E_F, very similar to the increase in the experimental O pre-edge peak in Figure 6.2. In the

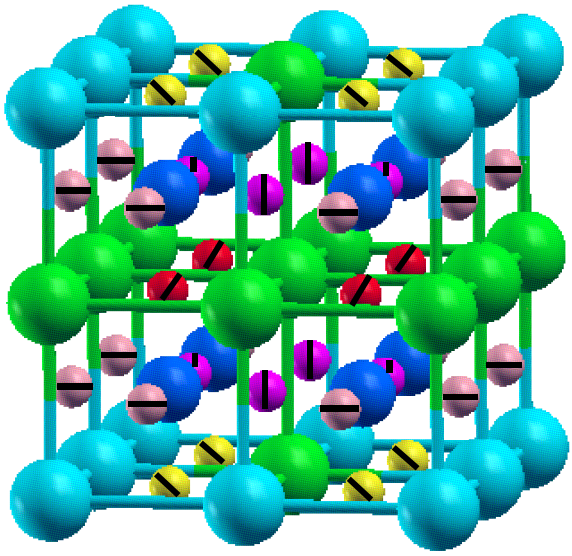

Figure 6.5: The 2×2×2 supercell for a Sr doping of 3/8. Large atoms: Sr, light blue; La, green; medium atoms (blue) Co. There are four types of (small) O atoms: right slant line (red), no Sr neighbors (O1); vertical line (purple), one Sr neighbor (O2); horizontal line (gray), two Sr neighbors (O3); left slant line (yellow), three Sr neighbors (O4).

calculations, the energies are with respect to E_F, so the XAS does not shift to lower energy as observed experimentally. We also calculated the O XMCD signal as a function of Sr concentration as shown in Figure 6.6. Again, the theoretical results agree quite well with the experimental results shown in Figure 6.1; specifically, there is only an O XMCD signal over the same energies for which the O XAS has a large increase. The lack of an amplitude change with x is likely from the use of a pseudo-cubic cell.

Further important details are obtained by calculating the hole fraction on Co and O atoms, induced via Sr doping, using similar energy ranges as for Figure 6.3. In Figure 6.7, we plot the induced hole density as a function of x; the calculated O hole density is comparable to but slightly larger than that on the Co atoms. Thus, the induced holes are nearly equally distributed over the Co and O atoms.

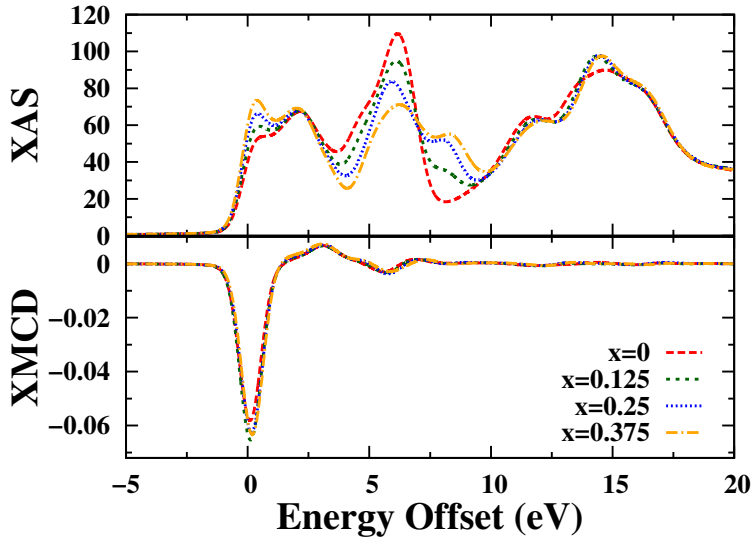

Figure 6.6: The theoretical O K-edge, showing a significant increase at the beginning of the edge, and the calculated O K-edge XMCD signal, both for $0 < x < 0.375$.

The calculations of the individual O magnetic moments are even more unusual. These results, tabulated in Table 6.1, show that the O atoms in the supercell are not all equivalent. Their properties depend on the number of neighboring Sr atoms, which can vary from 0 to 3: the larger the number of Sr neighbors, the larger the calculated magnetic moment. Thus, these calculations show the limitations of the VCA; the system is not homogeneous at the local level. For Co, it is likely that a similar situation occurs. However, the cubic supercell is not large enough to discriminate as within the 2×2×2 supercell all Co are equivalent. Another calculation using a trigonal distortion of the basic unit cell does indeed find different Co moments on different sites.

Another interesting feature from the calculated O-PDOS 6.4 is that it provides a simple explanation as to why there are magnetic and non-magnetic holes; just above E_F the spin up and spin down O-PDOS are not equal so those energy states will have

Label	# Sr Neighbors	Moment (μ_B)	Relative Weight
O1	0	0.067	4
O2	1	0.078	8
O3	2	0.095	8
O4	3	0.121	4

Table 6.1: O magnetic moments for the four types of O sites at x = 0.375. The average weighted moment is 0.089 μ_B.

a net moment. At higher energies the spin up and spin down O-PDOS are about equal and will have no net moment.

6.4 Discussion

The O K-edge XAS and XMCD data for LSCO presented above show that a surprisingly large fraction of the Sr-induced holes, go onto the O sites and increase the empty O PDOS just above the Fermi energy. More importantly, these new O states are magnetic in contrast to most of the O states. The increases in the O XAS and XMCD are not linear with x and appear to be correlated with the overall magnetism in the system which changes from a glass-like behavior below 18% (described as FM clusters) to metallic FM above 18%. Calculations qualitatively agree quite well with both the XAS and XMCD at the O K-edge, and indeed find a significant spin magnetic moment on O atoms. Further, the theoretical results show that the properties of the O atoms are not all equivalent, and have different moments; this indicates that the virtual crystal approximation is not adequate for describing systems such as LSCO, for which the electron density and oxygen moments are sensitive to nearby Sr positions. The variation in the small fraction of O states that carry angular momentum may be

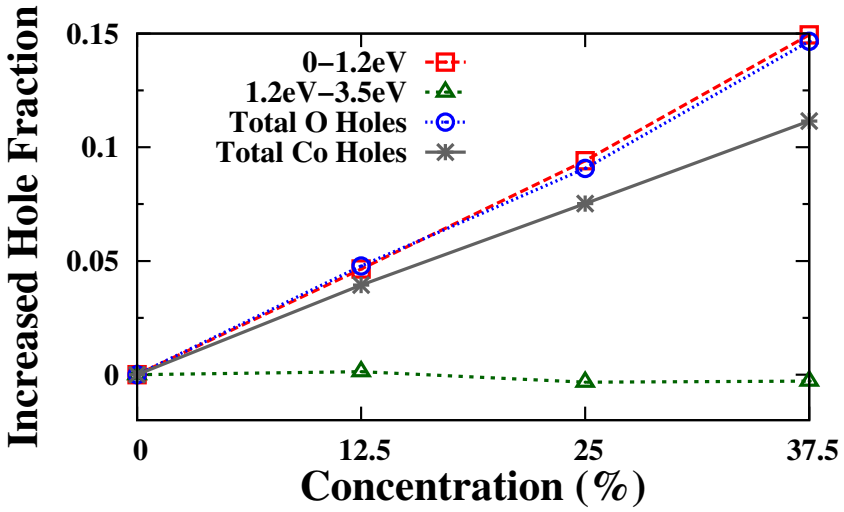

Figure 6.7: Calculated hole fractions: magnetic O-hole fraction (red square), non-magnetic O-hole fraction (green triangle), total O-holes (blue circle), total Co-holes (grey star).

part of the explanation for the unusual magnetic behavior in these systems and must be considered in future models for cobaltites.

Bibliography

H. M. Aarbogh, J. Wu, L. Wang, H. Zheng, J. F. Mitchell, and C. Leighton. Magnetic and electronic properties of $La_{1-x}Sr_xCoO_3$ single crystals across the percolation metal-insulator transition. *Phys. Rev. B* **74**, 134408 (2006).

P. S. Anil Kumar, P. A. Joy, and S. K. Date. Origin of the cluster-glass-like magnetic properties of the ferromagnetic system $La_{0.5}Sr_{0.5}CoO_3$. *J. Phys.: Condens. Matter* **10**, L487 (1998).

A. L. Ankudinov, B. Ravel, J. J. Rehr, and S. D. Conradson. Real-space multiple-scattering calculation and interpretation of x-ray-absorption near-edge structure. *Phys. Rev. B* **58**, 7565 (1998a).

A. L. Ankudinov, B. Ravel, J. J. Rehr, and S. D. Conradson. Real space multiple scattering calculation of XANES. *Phys. Rev. B* **58**, 7565 (1998b).

E. F. Apple and J. S. Prener. On the infrared emission in ZnS:Cu–effect of sulfur pressure and aluminum. *J. Phys. Chem. Solids* **13**, 81 (1960).

M. Aven and J. A. Parodi. Study of the crystalline transformations in ZnS:Cu, ZnS:Ag and ZnS:Cu,Al. *J. Phys. Chem. Solids* **13**, 56 (1960).

M. A. Avila, K. Suekuni, K. Umeo, H. Fukuoka, S. Yamanaka, and T. Takabatake. $Ba_8Ga_{16}Sn_{30}$ with type-I clathrate structure: Drastic suppression of heat conduction. *Appl. Phys. Lett.* **92**, 041901 (2008).

R. Baumbach, F. Bridges, L. Downward, D. Cao, P. Chesler, and B. Sales. Off-center phonon scattering sites in $Eu_8Ga_{16}Ge_{30}$ and $Sr_8Ga_{16}Ge_{30}$. *Phys. Rev. B.* **71**, 024202 (2005).

R. N. Bhargava, D. Gallagher, X. Hong, and A. Nurmikko. Optical properties of manganese-doped nanocrystals of ZnS. *Phys. Rev. Lett.* **72**, 416 (1994).

P. Blaha, K. Schwarz, G. K. H. Madsen, D. Kvasnick, and J. Luitz. In A. K. Schwarz, TU Wien, ed., *WIEN2k, An augmented Plane wave + Local Orbitals Program for Calculation Crystal Properties* (2001).

N. P. Blake, D. Bryan, S. Latturner, L. Mollnitz, G. D. Stucky, and H. Metiu. Structure and stability of the clathrates $Ba_8Ga_{16}Ge_{30}$, $Sr_8Ga_{16}Ge_{30}$, $Ba_8Ga_{16}Si_{30}$, and $Ba_8In_{16}Sn_{30}$. *J. Chem. Phys.* **114**, 10063 (2001).

H. Blicks, N. Riehl, and R. Sizmann. Reversible leuchtzentren-umwandlungen in ZnS-phosphoren. *Z. Phys.* **163**, 594 (1961).

A. A. Bol, J. Ferwerda, J. A. Bergwerff, and A. Meijerink. Luminescence of nanocrystalline ZnS:Cu^{2+}. *J. Lumin.* **99**, 325 (2002).

C. H. Booth. R-Space X-ray Absorption Package (2012). http://lise.lbl.gov/RSXAP/.

C. H. Booth and F. Bridges. Improved self absorption correction for fluorescence measurements of extended X-ray absorption fine structure. *Physica Scripta* **T115**, 202 (2005).

A. I. Boukai, Y. Bunimovich, J. Tahir-Kheli, J.-K. Yu, W. A. Goddard, and J. R. Heath. Silicon nanowires as efficient thermoelectric materials. *Nature* **451**, 168 (2008).

R. Bowers and N. T. Melamed. Luminescent centers in ZnS:Cu,Cl phosphors. *Phys. Rev.* **99**, 1781 (1955).

F. Bridges, C. H. Booth, M. Anderson, G. H. Kwei, J. J. Neumeier, J. Snyder, J. Mitchell, J. S. Gardner, and E. Brosha. Mn K-edge studies of $La_{1-x}A_xMnO_3$ systems (A = Ca, Ba, Pb). *Phys. Rev. B* **63**, 214405/1 (2001).

F. Bridges, L. Downward, J. J. Neumeier, and T. A. Tyson. Detailed relationship between local structure, polarons, and magnetization for $La_{1-x}Ca_xMnO_3$ ($0.21 \leq x \leq 0.45$). *Phys. Rev. B* **81**, 184401 (2010a).

F. Bridges, S. Medling, B. Balaban, and S. A. Carter. Degradation and local distortion in electroluminescent ZnS:Cu,Cl phosphors. *IOP Conf. Ser.: Mater. Sci. Eng.* **15**, 012028 (2010b).

R. Caciuffo, D. Rinaldi, G. Barucca, J. Mira, J. Rivas, M. A. Senaris-Rodriguez, P. G. Radaelli, D. Fiorani, and J. B. Goodenough. Structural details and magnetic order of $La_{1-x}Sr_xCoO_3$ ($x \leq 0.3$). *Phys. Rev. B* **59**, 1068 (1999).

L. Cao, J. Zhang, S. Ren, and S. Huang. Luminescence enhancement of core-shell ZnS:Mn/ZnS nanoparticles. *Appl. Phys. Lett.* **80**, 4300 (2002).

B. Car, S. Medling, C. Corrado, F. Bridges, and J. Z. Zhang. Probing the local structure of dilute Cu dopants in fluorescent ZnS nanocrystals using EXAFS. *Nanoscale* **3**, 4182 (2011).

M. A. Chamarro, V. Voliotis, R. Grousson, P. Lavallard, T. Gacoin, G. Counio, J. P. Boilot, and R. Cases. Optical properties of Mn-doped CdS nanocrystals. *J. Cryst. Growth* **159**, 853 (1996).

W. C. W. Chan and S. Nie. Quantum dot bioconjugates for ultrasensitive nonisotopic detection. *Science* **281**, 2016 (1998).

W. Chen, J. O. Malm, V. Zwiller, Y. Huang, S. Liu, R. Wallenberg, J. O. Bovin, and L. Samuelson. Energy structure and fluorescence of Eu^{2+} in ZnS:Eu nanoparticles. *Phys. Rev. B* **61**, 11021 (2000).

W. Chen, J. Z. Zhang, and A. G. Joly. Optical properties and potential applications of doped semiconductor nanoparticles. *J. Nanosci. Nanotech.* **4**, 919 (2004).

D. Y. Chung, T. Hogan, J. Schindler, L. Iordarridis, P. Brazis, C. Kannewurf, B. Chen, C. Uher, and M. Kanatzidis. Complex bismuth chalcogenides as thermoelectrics. In *Thermoelectrics, 1997. Proceedings ICT '97. XVI International Conference on* (1997), pp. 459 –462.

C. Corrado, M. Hawker, G. Livingston, S. Medling, F. Bridges, and J. Z. Zhang. Enhanced cu emission in ZnS : Cu,Cl/ZnS core-shell nanocrystals. *Nanoscale* **2**, 1213 (2010).

C. Corrado, Y. Jiang, F. Oba, M. Kozina, F. Bridges, and J. Z. Zhang. Synthesis, structural, and optical properties of stable ZnS:Cu,Cl nanocrystals. *J. Phys. Chem. A* **113**, 3830 (2009).

G. Destriau. Experimental studies on the action of an electric field on phosphorescent sulfides. *J. Chem. Physics.* **33**, 620 (1936).

L. Downward, C. H. Booth, W. W. Lukens, and F. Bridges. A variation of the f-test for determining statistical relevance of particular parameters in EXAFS fits. In *X-ray Absorption Fine Structure - XAFS13: 13th International Conference*. American Institute of Physics, New York (2006).

S. C. Erwin, L. Zu, M. I. Haftel, A. L. Efros, T. A. Kennedy, and D. J. Norris. Doping semiconductor nanocrystals. *Nature* **436**, 91 (2005).

S. Faria. Electroluminescent characteristics of small particle size phosphors. *J. Electrochem. Soc.* **110**, 2627 (1988).

A. G. Fischer. Electroluminescent lines in ZnS powder particles. *J. Electrochem. Soc.* **109**, 1043 (1962).

A. G. Fischer. Electroluminescent lines in ZnS powder particles: II. models and comparison with experience. *J. Electrochem. Soc.* **110**, 733 (1963).

B. Gilbert, F. Huang, H. Zhang, G. Waychunas, and J. Banfield. Nanoparticles: Strained and stiff. *Science* **305**, 651 (2004).

J. Goodenough. Electronic and ionic transport properties and other physical aspects of perovskites. *Rep Prog Phys* **67**, 1915 (2004).

A. R. Han, S. Hwang, Y. Zhao, and Y. Kwon. X-ray absorption spectroscopic and magnetic characterization of cobalt-doped zinc oxide nanocrystals prepared by the molten-salt method. *J. Magn. Mater.* **320**, 1591 (2008).

D. Haskel (1999). http://www.aps.anl.gov/~haskel/FLUO/fluo.ps.

C. He, M. A. Torija, J. Wu, J. W. Lynn, H. Zheng, J. F. Mitchell, and C. Leighton. Non-griffiths-like clustered phase above the Curie temperature of the doped perovskite cobaltite $La_{1-x}Sr_xCoO_3$. *Phys. Rev. B* **76**, 014401/1 (2007).

J. P. Heremans, V. Jovovic, E. Toberer, A. Saramat, K. Kurosaki, A. Charoenphakdee, S. Yamanaka, and G. J. Snyder. Enhancement of thermoelectric efficiency in PbTe by distortion of the electronic density of states. *Science* **321**, 554 (2008).

W. C. Holton, M. de Wit, R. K. Watts, T. L. Estle, and J. Schneider. Paramagnetic copper centers in ZnS. *J. Phys. Chem. Solids* **30**, 963 (1969).

J.-I. Igarashi and K. Hirai. Magnetic circular dichroism at the K edge of nickel and iron. *Phys. Rev. B* **50**, 17820 (1994).

M. Imada, A. Fujimori, and Y. Tokura. Metal-insulator transitions. *Rev. Mod. Phys.* **70**, 1039 (1998).

M. Itoh, I. Natori, S. Kubota, and K. Motoya. Spin-glass behavior and magnetic phase diagram of $La_{1-x}Sr_xCoO_3$ ($0 \leq x \leq 0.5$) studied by magnetization measurements. *J. Phys. Soc. Japan* **63**, 1486 (1994).

J. Stöhr. Exploring the microscopic origin of magnetic anisotropies with X-ray magnetic circular dichroism (XMCD) spectroscopy. *Journal of Magnetism and Magnetic Materials* **200**, 470 (1999).

D. Jiang, L. Cao, W. Liu, G. Su, H. Qu, Y. Sun, and B. Dong. Synthesis and luminescence properties of core/shell ZnS:Mn/ZnO nanoparticles. *Nanoscale Res. Lett.* **4**, 78 (2009a).

Y. Jiang, F. Bridges, N. Sundaram, D. P. B. I. E. Anderson, J. F. Mitchell, and H. Zheng. Study of the local distortions of the perovskite system $La_{1-x}Sr_xCoO_3$ ($0 \leq x \leq 0.35$) using the extended X-ray absorption fine structure technique. *Phys. Rev. B* **80**, 144423 (2009b).

A. A. Khosravi, M. Kundu, L. Jatwa, S. K. Deshpande, U. A. Bhagwat, M. Sastry, and S. K. Kulkarni. Green luminescence from copper doped zinc sulphide quantum particles. *Applied Physics Letters* **67**, 2702 (1995).

S. Kishimoto, T. Hasegawa, H. Kinto, O. Matsumoto, and S. Iida. Effect and comparison of co-doping of Ag, Ag plus In, and Ag+Cl in ZnS: N/GaAs layers prepared by vapor-phase epitaxy. *J. Cryst. Growth* **214-215**, 556 (2000).

V. I. Klimov, S. A. Ivanov, J. Nanda, M. Achermann, I. Bezel, J. A. McGuire, and A. Piryatinski. Single-exciton optical gain in semiconductor nanocrystals. *Nature* **447**, 441 (2007).

K. Knížek, P. Novák, and Z. Jirák. Spin state of LaCoO3: Dependence on CoO6 octahedra geometry. *Phys. Rev. B* **71**, 054420 (2005).

D. Koningsberger and R. Prins, eds. *X-Ray Absorption Principles, Applications, Techniques of EXAFS, SEXAFS, and XANES.* Wiley, New York (1988).

Y. Kono, N. Ohya, T. Taguchi, K. Suekuni, T. Takabatake, S. Yamamoto, and K. Akai. First-principles study of type-i and type-viii $ba_8ga_{16}sn_{30}$ clathrates. *J. Appl. Phys.* **107**, 123720 (2010).

M. Kozina, F. Bridges, Y. Jiang, M. A. Avila, K. Suekuni, and T. Takabatake. Direct verification of Ga-Ga bond avoidance in the type-I clathrate $Ba_8Ga_{16}Ge_{30}$ from its x-ray absorption fine structure. *Phys. Rev. B* **80**, 212101 (2009).

M. Kriener, M. Braden, H. Kierspel, D. Senff, O. Zabara, C. Zobel, and T. Lorenz. Magnetic and structural transitions in La(1-x)A(x)CoO(3) (A=Ca, Sr, and Ba). *Phys. Rev. B* **79**, 224104 (2009).

Z. Kvitky, F. Bridges, and G. van Dorssen. Systematic deviations between theoretical and experimental EXAFS functions: Possible evidence of interstitial scattering outside the muffin-tin radius. *Phys. Rev. B* **64**, 214108 (2001).

P. A. Lee and J. B. Pendry. Theory of the extended x-ray absorption fine structure. *Phys. Rev. B* **11**, 2795 (1975).

W. Lehmann. Voltage dependence and particle size distribution of electroluminescent phosphors. *J. Electrochem. Soc.* **107**, 20 (1960).

W. Lehmann. Hyper-maintenance of electroluminescence. *J. Electrochem. Soc.* **113**, 40 (1966).

G. G. Li, F. Bridges, and C. H. Booth. XAFS standards: a comparison of experiments and theory. *Phys. Rev. B* **52**, 6332 (1995).

J. Manam, V. Chatterjee, S. Das, A. Choubey, and S. K. Sharma. Preparation, characterization and study of optical properties of ZnS nanophosphor. *Journal of Luminescence* **130**, 292 (2010).

S. Mano, T. Onimaru, S. Yamanaka, and T. Takabatake. Off-center rattling and thermoelectric properties of type-II clathrate $(K, Ba)_{24}(Ga, Sn, \square)_{136}$ single crystals. *Phys. Rev. B* **84**, 214101 (2011).

S. Medling and F. Bridges. Background subtraction for fluorescence EXAFS data of a very dilute dopant Z in Z+1 host. *J. Synch. Rad.* **18**, 679 (2011).

S. Medling, C. France, B. Balaban, M. Kozina, Y. Jiang, F. Bridges, and S. A. Carter. Understanding and improving electroluminescence in mill-ground ZnS:Cu,Cl phosphors. *J. Phys. D: Appl. Phys.* **44**, 205402 (2011).

M. Merz, P. Nagel, C. Pinta, A. Samartsev, H. v. Löhneysen, M. Wissinger, S. Uebe, A. Assmann, D. Fuchs, and S. Schuppler. X-ray absorption and magnetic circular dichroism of $LaCoO_3$, $La_{0.7}Ce_{0.3}CoO_3$, and $La_{0.7}Sr_{0.3}CoO_3$ films: Evidence for cobalt-valence-dependent magnetism. *Phys. Rev. B* **82**, 174416 (2010).

A. Mineshige, M. Kobune, S. Fujii, Z. Ogumi, M. Inaba, T. Yao, and K. Kikuchi. Metal-insulator transistion and crystal strucuture of $La_{1-x}Sr_xCoO_3$ as functions of Sr-content, temperature, and oxygen partial pressure. *J. Solid State Chem.* **142**, 374 (1999).

N. K. Morozova, V. G. Galstyan, and V. I. Muratova. Nature of the inhomogeneities and luminescence centers in low-Ohmic single ZnS crystals doped with Al. *Izv. Akad. Nauk SSSR Neorg. Mater.* **21**, 1097 (1985).

J. Nickerson, P. Goldberg, and D. H. Baird. The influence of copper on structural transformations in ZnS:Cu,Cl. *J. Electrochem. Soc.* **110**, 1228 (1963).

Y.-T. Nien and I.-G. Chen. Raman scattering and electroluminescence of ZnS:Cu,Cl phosphor powder. *Appl. Phys. Lett.* **89**, 261906 (2006).

M. Nirmal, B. O. Dabbousi, M. G. Bawendi, J. J. Macklin, J. K. Trautman, T. D. Harris, and L. E. Brus. Fluorescence intermittency in single cadmium selenide nanocrystals. *Nature* **383**, 802 (1996).

G. S. Nolas, J. L. Cohn, G. A. Slack, and S. B. Schujman. Semiconducting Ge clathrates: Promising candidates for thermoelectric applications. *Appl. Phys. Lett.* **73**, 178 (1998).

T. J. Norman, D. Magana, T. Wilson, C. Burns, J. Z. Zhang, D. Cao, and F. Bridges. Optical and surface structural properties of Mn^{2+}-doped ZnSe nanoparticles. *J. Phys. Chem. B* **107**, 6309 (2003).

J. Okamoto, H. Miyauchi, T. Sekine, T. Shidara, T. Koide, K. Amemiya, A. Fujimori, T. Saitoh, A. Tanaka, Y. Takeda, and M. Takano. Magnetic circular X-ray dichroism study of $La_{1-x}Sr_xCoO_3$. *Phys. Rev. B* **62**, 4455 (2000).

X. Peng. Mechanisms for the shape-control and shape-evolution of colloidal semiconductor nanocrystals. *Adv. Mater.* **15**, 459 (2003).

J. P. Perdew and Y. Wang. Accurate and simple analytic representation of the electron-gas correlation energy. *Phys. Rev. B* **45**, 13244 (1992).

N. Pradhan and D. M. Battaglia. Efficient, stable, small, and water-soluble doped ZnSe nanocrystal emitters as non-cadmium biomedical labels. *Nano Lett.* **7**, 312 (2007).

Z. Quan, Z. Wang, P. Yang, J. Lin, and J. Fang. Synthesis and characterization of high-quality ZnS, ZnS:Mn^{2+}, and ZnS:Mn^{2+}/ ZnS(core-shell) luminescent nanocrystals,. *Inorg. Chem.* **46**, 1354 (2007).

P. Ravindran, H. Fjellvag, A. Kjekshus, P. Blaha, K. Schwarz, and J. Luitz. Itinerant metamagnetism and possible spin transition in $LaCoO_3$ by temperature/hole doping. *J. Appl. Phys.* **91**, 291 (2002).

P. Ravindran, P. A. Korzhavyi, H. Fjellvag, and A. Kjekshus. Electronic structure, phase stability, and magnetic properties of $La_{1-x}Sr_xCoO_3$ from first-principles full-potential calculations. *Phys. Rev. B.* **60**, 16423 (1999).

J. J. Rehr (2009). Private communication.

S. Roberts. Aging characteristics of electroluminescent phosphors. *J. Appl. Phys.* **28**, 262 (1957).

T. Saitoh, T. Mizokawa, A. Fujimori, M. Abbate, Y. Takeda, and M. Takano. Electronic structure and magnetic states in $La_{1-x}Sr_xCoO_3$ studied by photoemission and x-ray-absorption spectroscopy. *Phys. Rev. B* **56**, 1290 (1997).

H. J. Sánchez, M. C. Valentinuzzi, and C. Pérez. X-ray resonant raman scattering cross sections of Mn, Fe, Cu and Zn. *J. Phys. B: At. Mol. Opt. Phys.* **39**, 4317 (2006).

D. Sarma, N. Shanthi, and P. Mahadevan. Electronic excitation spectra from ab initio band-structure results for LaMO3 (M=Cr,Mn,Fe,Co,Ni). *Phys. Rev. B* **54**, 1622 (1996).

G. Schütz, W. Wagner, W. Wilhelm, P. Kienle, R. Zeller, R. Frahm, and G. Materlik. Absorption of circularly polarized x rays in iron. *Phys. Rev. Lett.* **58**, 737 (1987).

S. Shionoya. Principal phosphor materials and their optical properties. In S. Shionoya and W. M. Yen, eds., *Phosphor Handbook*, CRC Press, New York, chap. 3, pp. 231–258 (1999).

S. Shionoya, T. Koda, K. Era, and H. Fujiwara. Nature of luminescence transitions in ZnS crystals. *J. Phys. Soc. Jpn.* **19**, 1157 (1964).

S. Shionoya, K. Urabe, K. Era, and H. Fujiwara. Nature of the red-copper luminescence centre in ZnS crystals as elucidated by polarization measurements. *J. Phys. Chem. Solids* **27**, 865 (1966).

V. V. Sikolenko, A. P. Sazonov, I. O. Troyanchuk, D. Tobbens, U. Zimmermann, E. V. Pomjakushina, and H. Szymczak. Magnetic properties of $La_{1-x}Sr_xCoO_3$ (x = 0.15 and 0.3). *J. Phys.:Condens. Matter* **16**, 7313 (2004).

M. Sikora, C. Kapusta, K. Knizek, Z. Jirak, C. Autret, M. Borowiec, C. J. Oates, V. Prochazka, D. Rybicki, and D. Zajac. X-ray absorption near-edge specroscopy study of mn and co valence states in $LaMn_{1-x}Co_xO_3$ (x=0-1). *Phys. Rev. B* **73**, 094426 (2006).

B. A. Smith, J. Z. Zhang, A. Joly, and J. Liu. Luminescence decay kinetics of Mn^{2+}-doped ZnS nanoclusters grown in reverse micelles. *Phys. Rev. B.* **62**, 2021 (2000).

G. J. Snyder and T. S. Ursell. Thermoelectric efficiency and compatibility. *Phys. Rev. Lett.* **91**, 148301 (2003).

Y. L. Soo, Z. H. Ming, S. W. Huang, Y. H. Kao, R. N. Bhargava, and D. Gallagher. Local structures around Mn luminescent centers in Mn-doped nanocrystals of ZnS. *Phys. Rev. B.* **50**, 7602 (1994).

J. Stanley, Y. Jiang, F. Bridges, S. A. Carter, and L. Ruhlen. Degradation and rejuvenation studies of AC electroluminescent ZnS:Cu,Cl phosphors. *J. Phys.: Condens. Matter* **22**, 055301(15) (2010).

E. Stern. Theory of the extended x-ray-absorption fine structure. *Phys. Rev B* **10**, 3027 (1974).

K. Suekuni, M. A. Avila, K. Umeo, H. Fukuoka, S. Yamanaka, T. Nakagawa, and T. Takabatake. Simultaneous structure and carrier tuning of dimorphic clathrate $Ba_8Ga_{16}Sn_{30}$. *Phys. Rev. B* **77**, 235119 (2008).

K. Suekuni, T. Tanaka, S. Yamamoto, M. A. Avila, K. Umeo, Y. Takasu, T. Hasegawa, N. Ogita, M. Udagawa, and T. Takabatake. Off-center guest vibrations and their effect on lattice thermal conductivity in n- and p-type β-$Ba_8Ga_{16}Sn_{30}$. *J. Electronic Mater.* **38**, 1516 (2009).

N. Sundaram, Y. Jiang, I. E. Anderson, D. P. Belanger, C. H. Booth, F. Bridges, J. F. Mitchell, T. Proffen, and H. Zheng. Local structure of $La_{1-x}Sr_xCoO_3$ determined from EXAFS and neutron pair distribution function studies. *Phys. Rev. Lett.* **102**, 026401 (2009).

A. Suzuki and S. Shionoya. Mechanism of the green-copper luminescence in ZnS crystals. I. direct evidence for the pair emission mechanism. *J. Phys. Soc. Jpn.* **31**, 1455 (1971).

H. Takahashi, F. Munakata, and M. Yamanaka. Ab initio study of the electronic structures in LaCoO3-SrCoO3 systems. *Phys. Rev. B* **57**, 15211 (1998).

S. Tanaka, H. Kobayashi, and H. Sasakura. Electroluminescence materials. In S. Shionoya and W. Yen, eds., *Phosphor Handbook*, CRC Press, New York, chap. 9, pp. 601–612 (1999).

B. K. Teo. *EXAFS: Basic Principles and Data Analysis.* Springer-Verlang, New York (1986).

W. A. Thornton. Electroluminescence in zinc sulphide. *Phys. Rev.* **102**, 38 (1956).

W. A. Thornton. Electroluminescence maintenance. *J. Electrochem. Soc.* **107**, 895 (1960).

O. Toulemonde, N. N'Guyen, and F. S. A. Traverse. Spin state transition in $LaCoO_3$ with temperature or strontium doping as seen by XAFS. *J. Solid State Chem.* **158**, 208 (2001).

K. Urabe, S. Shionoya, and A. Suzuki. Polarization of the blue-copper luminescence in ZnS crystals. *J. Phys. Soc. Jpn.* **25**, 1611 (1968).

R. Venkatasubramanian, E. Siivola, T. Colpitts, and B. O'Quinn. Thin-film thermoelectric devices with high room-temperature figures of merit. *Nature* **413**, 597 (2001).

M. Warkentin, F. Bridges, S. A. Carter, and M. Anderson. Electroluminescence materials ZnS:Cu,Cl and ZnS:Cu,Mn,Cl studied by EXAFS spectroscopy. *Phys. Rev. B* **75**, 075301/1 (2007).

R. Withnall, J. Silver, T. G. Ireland, G. R. Fern, and P. J. Marsh. Structure and morphology of ACEL ZnS:Cu,Cl phosphor powder etched by hydrochloric acid. *J. Electrochem. Soc.* **156**, J326 (2009).

V. Wood, J. E. Halpert, M. J. Panzer, M. G. Bawendi, and V. Bulovic. Alternating current driven electroluminescence from ZnSe/ZnS:Mn/ZnS nanocrystals. *Nano Letters* **9**, 2367 (2009).

J. Wu and C. Leighton. Glassy ferromagnetism and magnetic phase separation in $La_{1-x}Sr_xCoO_3$. *Phys. Rev. B.* **67**, 174408 (2003).

S. Yamaguchi, Y. Okimoto, H. Taniguchi, and Y. Tokura. Spin-state transition and high-spin polarons in $LaCoO_3$. *Phys. Rev. B* **53**, R2926 (1996).

H. Yang, P. H. Holloway, and B. B. Ratna. Photoluminescent and electroluminescent properties of Mn-doped ZnS nanocrystals. *J. Appl. Phys.* **93**, 586 (2003).

P. Yang, M. Lü, D. Xü, D. Yuan, and G. Zhou. Photoluminescence properties of zns nanoparticles co-doped with Pb^{2+} and Cu^{2+}. *Chem. Phys. Lett.* **336**, 76 (2001).

J. Z. Zhang. Interfacial charge carrier dynamics of colloidal semiconductor nanoparticles. *J. Phys. Chem. B* **104**, 7239 (2000).

J. Zheng, X. Yuan, M. Ikezawa, P. Jing, X. Liu, Z. Zheng, X. Kong, J. Zhao, and Y. Masumoto. Efficient photoluminescence of Mn^{2+} ions in MnS/ZnS core-shell quantum dots. *J. Phys. Chem. C* **113**, 16969 (2009).